AFRL-AFOSR-VA-TR-2023-0368

Biomimetic Design of Morphing Micro Air Vehicles

Perkinson, Harry
TEXAS RESEARCH INSTITUTE, AUSTIN, INC.
9063 BEE CAVES RD
AUSTIN, TX, 78733
USA

06/14/2023
Final Technical Report

Air Force Research Laboratory
Air Force Office of Scientific Research
Arlington, Virginia 22203
Air Force Materiel Command

REPORT DOCUMENTATION PAGE

PLEASE DO NOT RETURN YOUR FORM TO THE ABOVE ORGANIZATION.

1. REPORT DATE	2. REPORT TYPE	3. DATES COVERED	
20230614	Final	START DATE 20171201	END DATE 20201130

4. TITLE AND SUBTITLE
Biomimetic Design of Morphing Micro Air Vehicles

5a. CONTRACT NUMBER	5b. GRANT NUMBER	5c. PROGRAM ELEMENT NUMBER
FA9550-18-C-0001		61102F
5d. PROJECT NUMBER	**5e. TASK NUMBER**	**5f. WORK UNIT NUMBER**

6. AUTHOR(S)
Harry Perkinson

7. PERFORMING ORGANIZATION NAME(S) AND ADDRESS(ES)
TEXAS RESEARCH INSTITUTE, AUSTIN, INC.
9063 BEE CAVES RD
AUSTIN, TX 78733
USA

8. PERFORMING ORGANIZATION REPORT NUMBER

9. SPONSORING/MONITORING AGENCY NAME(S) AND ADDRESS(ES)
Air Force Office of Scientific Research
875 N. Randolph St. Room 3112
Arlington, VA 22203

10. SPONSOR/MONITOR'S ACRONYM(S)
AFRL/AFOSR RTB2

11. SPONSOR/MONITOR'S REPORT NUMBER(S)
AFRL-AFOSR-VA-TR-2023-0368

12. DISTRIBUTION/AVAILABILITY STATEMENT
A Distribution Unlimited: PB Public Release

13. SUPPLEMENTARY NOTES

14. ABSTRACT
The attached report is a Final Technical Report for Contract No. FA9550-18-C-0001. This report covers the program period of performance from 1 December 2017 to 31 December 2020, for the effort entitled “Biomimetic Design of Morphing Micro Air Vehicles,” STTR Topic No AF15-AT01. A micro air vehicle (MAV)approximately the size of a bird of prey (hawk) was designed, built, tested, optimized, and demonstrated by the University of Florida Micro Air Vehicle Laboratory. The MAV design uses bimorphs to control flight surfaces and a servo motor to sweep the outboard wing. The flight control surfaces can be controlled by the autopilot in response to changing flight conditions and mission requirements or by the ground based pilot.

15. SUBJECT TERMS

16. SECURITY CLASSIFICATION OF:			17. LIMITATION OF ABSTRACT	18. NUMBER OF PAGES
a. REPORT U	b. ABSTRACT U	c. THIS PAGE U	UU	65

19a. NAME OF RESPONSIBLE PERSON	19b. PHONE NUMBER *(Include area code)*
BYUNG LEE	426-8483

Standard Form 298 (Rev.5/2020)
Prescribed by ANSI Std. Z39.18

REPORT DOCUMENTATION PAGE

Form Approved
OMB No. 0704-0188

1. REPORT DATE *(DD-MM-YYYY)*	**2. REPORT TYPE**	**3. DATES COVERED** *(From - To)DD-MM-YY*
31/12/2020	Final Technical Report	01/12/2017 – 31/12/2020

4. TITLE AND SUBTITLE

Biomimetic Design of Morphing Micro Air Vehicles
FINAL REPORT, Item 0001AH

5a. CONTRACT NUMBER
FA9550-18-C-0001

5b. GRANT NUMBER

5c. PROGRAM ELEMENT NUMBER

6. AUTHOR(S)
Harry Perkinson, Dr. Peter Ifju

5d. PROJECT NUMBER

5e. TASK NUMBER

5f. WORK UNIT NUMBER

7. PERFORMING ORGANIZATION NAME(S) AND ADDRESS(ES)
Texas Research Institute Austin, 415 Crystal Creek Drive, Austin, Texas 78733-6201

University of Florida,

8. PERFORMING ORGANIZATION REPORT NUMBER

F-30111:HEP:Final

9. SPONSORING / MONITORING AGENCY NAME(S) AND ADDRESS(ES)
AF Office of Scientific Research
875 North Randolph Street, Room 3112
Arlington, Virginia 22203-1954

10. SPONSOR/MONITOR'S ACRONYM(S)
AFOSR

11. SPONSOR/MONITOR'S REPORT NUMBER(S)

12. DISTRIBUTION / AVAILABILITY STATEMENT
Distribution Statement B: Distribution authorized to U.S. Government agencies only; (DFARS - SBIR Data Rights); December 1, 2017. Other requests for this document shall be referred to AF Office of Scientific Research, 875 North Randolph Street, Room 3112, Arlington, VA 22203-1954, Attn. Dr. Byung Lee. byung.lee@us.af.mil

13. SUPPLEMENTARY NOTES

14. ABSTRACT
The attached report is a Final Technical Report for Contract No. FA9550-18-C-0001. This report covers the program period of performance from 1 December 2017 to 31 December 2020, for the effort entitled "Biomimetic Design of Morphing Micro Air Vehicles," STTR Topic No AF15-AT01. A micro air vehicle (MAV)approximately the size of a bird of prey (hawk) was designed, built, tested, optimized, and demonstrated by the University of Florida Micro Air Vehicle Laboratory. The MAV design uses bimorphs to control flight surfaces and a servo motor to sweep the outboard wing. The flight control surfaces can be controlled by the autopilot in response to changing flight conditions and mission requirements or by the ground based pilot.

15. SUBJECT TERMS
Morphing, Micro Air Vehicles (MAVs), STTR Report

16. SECURITY CLASSIFICATION OF:			**17. LIMITATION OF ABSTRACT**	**18. NUMBER OF PAGES**	**19a. NAME OF RESPONSIBLE PERSON**
					Dr. Byung Lee
a. REPORT	**b. ABSTRACT**	**c. THIS PAGE**			**19b. TELEPHONE NUMBER** *(include area code)*
UNCLASSIFIED	UNCLASSIFIED	UNCLASSIFIED	SAR	64	(703)696-8483

Standard Form 298 (Rev. 8-98)
Prescribed by ANSI Std. Z39.18

Topic Title: Biomimetic Design of Morphing Micro Air Vehicles

Topic #: AF15-AT01

Texas Research Institute Austin, Inc.
415 Crystal Creek Drive
Austin, Texas 78746
512-263-2101

Contract Information:

Phase:	II
SYSCOM:	Air Force Office of Scientific Research
TPOC:	Dr. Byung (Les) Lee (byung.lee@us.af.mil)
Contract #:	FA9550-18-C-0001
PoP:	1 December 2017 to 31 December 2020

Corporate Official:
Matthew Berry, Contracts Administrator, 512-615-4482, mberry@tri-austin.com

Principal Investigator (PI):
Harry Perkinson, 512-426-5335, hperkinson@tri-austin.com

Prepared By:
Harry Perkinson, 512-426-5335, hperkinson@tri-austin.com

Table of Contents

Executive Summary 3
Project Objective 4
Project Approach 4
Analysis 4
Results 29
Conclusions 31
Recommendations 31
Appendix A: Key Terms 32
Appendix B: Supplemental Data 33

EXECUTIVE SUMMARY

Texas Research Institute Austin, Inc. (TRI Austin), in conjunction with the Micro Air Vehicles Laboratory at the University of Florida, has investigated the development of a micro air vehicle (MAV) design that can autonomously change wing length, planform, and control surfaces though the use of micro fiber composite bimorph actuation and autopilot programming.

The overall objective of the program was to design and develop a biomimetic morphing MAV that utilizes multifunctional materials to autonomously change configurations to adapt to varying flight regimes. A typical mission for a MAV will require a vehicle optimized for take-offs/landings, loitering, aggressive maneuvers, and fast-dash while diving. A single fixed MAV configuration is not optimized for all portions of a typical mission. The ability to reconfigure the MAV during the mission will increase the likelihood of mission success because the vehicle will be more fuel efficient, be able to hide in plain sight by looking and flying like a raptor (*Falco peregrinus*), and be capable of changing flight configurations to fly into environments for which one configuration would not be sufficient.

The morphing MAV program used an iterative design and test program to build and fly progressively more capable flight models. Starting with fixed winged craft, with the wings configured for flight in the take-off/landing, dive, loiter, and aggressive maneuver regimes, the evaluation process moved up to models that could be configured by hand and servo motors prior to and during flight. Finally, the model evaluation process used flight vehicles that incorporated micro fiber composite (MFC) bimorph piezoelectric actuation to modify control surfaces and servo motors to rotate the outboard wings.

Numerous test flights were conducted, all of which had flight test plans cleared and approved by the Air Force Office of Flight Testing and the Flight Worthiness Authority. Iterative finite element analyses (FEA), using information developed from test flights and laboratory testing, such as digital image corelation (DIC), were performed to optimize the vehicle's performance. Computational fluid dynamic (CFD) analyses were used to optimize the design of the flight control structures and lifting elements. Wind tunnel models were built and tested to verify vehicle FEA and CFD results.

The control system developed and evaluated consisted of a high bandwidth inner loop control and a lower bandwidth outer loop control, The inner loop control used MFC bimorph actuation of ailerons to control roll and MFC bimorphs actuation of elevators to control pitch. The outer loop control used mechanical servo motors to change wing area and static margin by rotating the outboard wing toward the fuselage. Both control loops were integrated into the autopilot control system.

The autonomous flight of an MFC bimorph-controlled MAV aircraft configuration was attempted at the University of Florida test flight field in December 2020. While the MFC bimorph passed the check off testing in the laboratory prior to flight testing, the MFC bimorphs shorted out and failed during initial power-up for the flight, resulting in the final design not being able to fly. The University of Florida has ordered new lots of MFC bimorphs, is building new flight surfaces, and will test fly the final design funded by a grant awarded to the University. University of Florida will continue the morphing MAV development after the AFOSR/TRI Austin contract closes and will report the results to AFOSR. The Biomimetic Design of Morphing Micro Air Vehicles Program is supporting the thesis research for two PhD candidates at the University of Florida.

PROJECT OBJECTIVE

The primary technical objective of the Phase II effort of the Biomimetic Design of Morphing Micro Air Vehicles Program is to demonstrate a flight vehicle capable of morphing wing shape, length, and planform shape autonomously in response to flight conditions encountered during the vehicle's autopilot-controlled mission. The constitutive objectives of the Phase II effort include:

a) Demonstrating that shape morphing can be accomplished to a large extent through the use of piezoelectric actuators;

b) Demonstrating the wing length can be modified by rotating the wing outboard portion under the inboard portion of the wing using a servo motor and system that will withstand the rigors of landing, and;

c) Integrating the capability of morphing the shapes of the MAV with the autopilot function in such a manner that the MAV will change shape in response to flight conditions in order to meet the requirements of a preprogrammed route.

An autonomously morphing micro air vehicle has military and commercial applications. Military applications include being able to place sensors or weapons on target in remote locations for which a convoluted flight path is required, or for which the flight path is through areas where the flying conditions change rapidly. Commercial applications include being able to fly a sensor platform in environments in which the flight environment is constantly in flux. Increased aircraft endurance can be realized through the capability of the vehicle to automatically morph to the configuration that will utilize the least amount of energy for any given flight environment.

PROJECT APPROACH

An iterative design approach was used in the development of the Biomimetic-based micro air vehicle. This design approach looked at different components of the vehicle, evaluating designs for these components, then building the component designs, and integrating these components into a test flight vehicle. Components or areas of technical analysis and focus included the outboard wing design, tail design, wing sweep mechanism, material studies and characterization, MFC bimorph hysteresis studies, fluid structure interaction studies, and control system studies.

ANALYSIS

Outboard Wing Design

Base Design

The major goal in the design of the control surfaces of the vehicle was to incorporate smart materials, i.e. piezoelectric actuators, as the control actuators for this vehicle. In addition, biomimicry was also an important aspect of the development of the control surfaces. The design of the control surfaces for the vehicle was approached in a local-global manner. The mechanical response of piezoelectric actuators was modeled analytically using finite element software. Experimental models were then created to validate the deflection observed in the analytical model. These results were used to study the aerodynamic response of the control surfaces during typical flight missions.

Macro fiber composites (MFCs) were chosen as the piezoelectric actuators to be used for this vehicle. MFCs were selected due to their high bandwidth of active control and relatively easy integration into the composite wing layup process compared to other smart materials. However, MFCs produce very small strain. MFCs can be attached to a substrate material to produce deflection through a unimorph or bimorph configuration. The unimorph configuration only uses one MFC, while a bimorph configuration uses two MFCs attached on opposite sides of the substrate. Bimorph configuration allows for equal deflections when actuated through the positive and negative range. The optimal selection of the substrate material, as well as where to place the MFCs, is crucial to obtaining the necessary deflection for the robust control of the vehicle.

The modeling of the outboard section of the wing requires an accurate model of MFCs when attached to a composite substrate. Carbon fiber plate samples with unimorph configurations were fabricated in the lab for experimental validation. The samples were coated with white paint and then speckled with black paint in preparation for digital image correlation (DIC). DIC is a non-contact measurement technique that uses a random speckle pattern on an object to track deformation over time using cameras. Two cameras were required to measure the out-of-plane deflection when MFCs are actuated as shown in Figure 1.

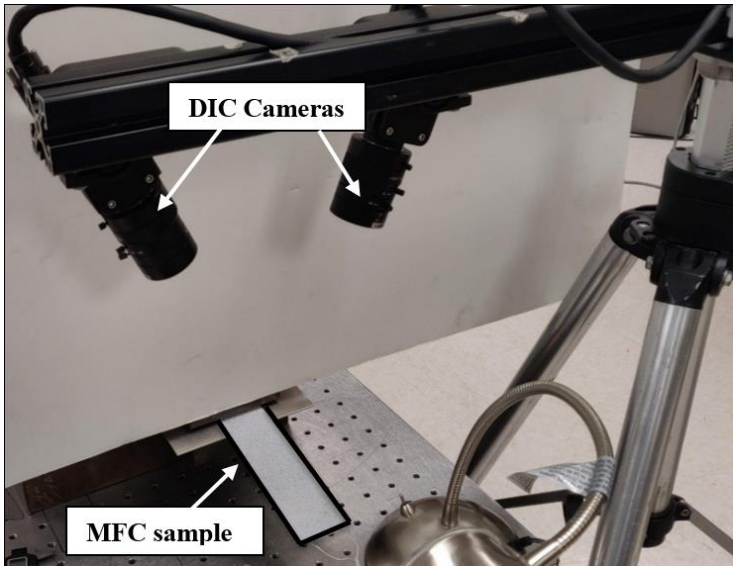

Figure 1: Experimental setup of cantilevered MFC with two cameras for 3D DIC

The data obtained from DIC was used to model the wing in ABAQUS, a finite element solver software. The properties of the carbon fiber to be used for manufacturing, as well as the mechanical properties of MFC, were inputted in the software. An initial study was done on the relationship between various orientations of MFCs and the amount of deflection achieved on the outboard section. MFC angles were evaluated from 0^o, with the longer side of the MFC oriented parallel with the leading edge, to 90^o, with the MFC perpendicular to the leading edge. A separate material coordinate system was used for the MFC to simplify steps in the iteration process. The orientation of the bidirectional carbon fiber was aligned to the MFC placement in the wing section. The boundary condition used for this study was fixed boundary at the root of the leading edge. An extra layer of bidirectional carbon fiber was assigned to the leading edge based on the physical design of the wing. The MFC at 45^o orientation has been presented in Figure 2. It was determined that the maximum deflection occurs at 61^o orientation of the MFC for this layup of the outboard section.

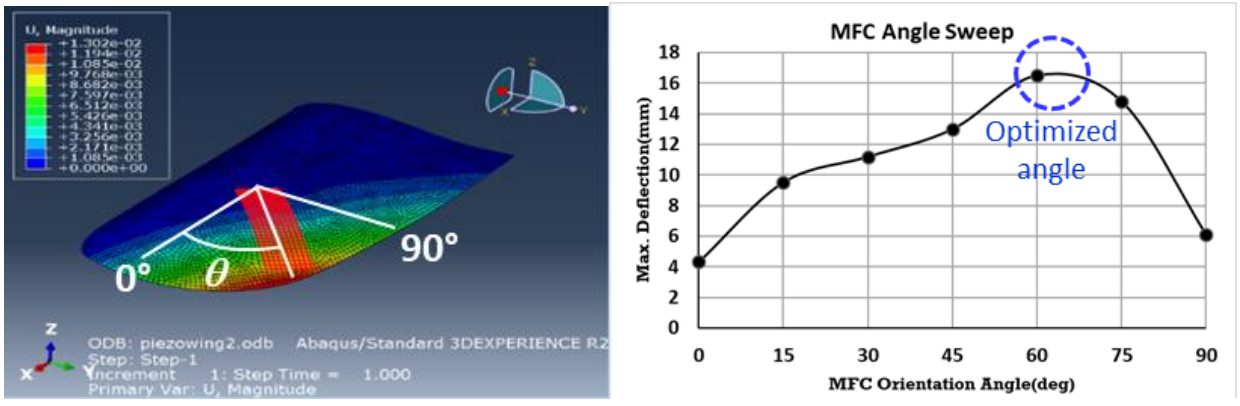

Figure 2: (left) FEA model of wing with MFC angle θ, (right) Deflection results based on MFC sweep

Outboard Wing with Overlap Regions

A full-scale version of an outboard wing was built with the MFC angles placed based on the initial optimization scheme. The initial configuration was continuous wing, the wing surface was uninterrupted. The next design iteration for the outboard wing included slits in the wing. Showing the MFC placement on the wing, the camera setup of a wing with slits is shown in the following Figure 3. The wing was

clamped at the root of the leading edge, which is the location for connecting with the inboard portion of the wing. There were three major regions to be studied. The first region is the most outboard part of the wing towards the tip before the first slit as seen in Figure 3. The second region, which is referred to as the MFC region, is the area between the two slits (dashed line in the Figure). The third region is the inner most region to the right of the second slit. In order to better understand the effect of the MFC region on all three regions, deflection data was extracted along the trailing edge of the wing. The solid line in the area of interest represents this location. The deflection results are shown in Figure 3. The graph shows that most of the deflection occurs in the MFC region which was expected for a wing with slits.

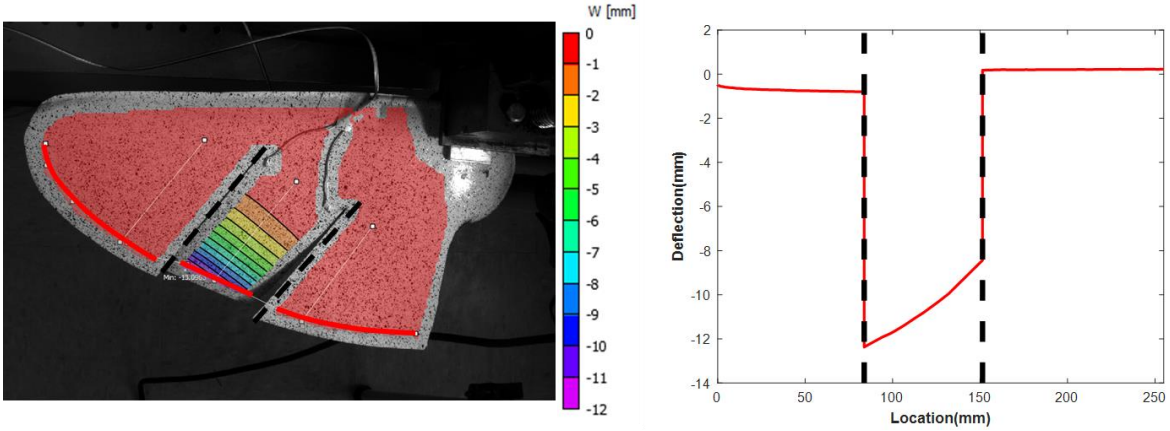

Figure 3: (a) DIC deflection results for fully slit wing, (b) Deflection results along the trailing edge of slit wing

There were six total configurations that were tested. The first configuration was the wing with no slit. The second configuration was a fully slit wing. The third configuration had the MFC region overlap the other two regions from the bottom. The fourth configuration had the MFC region overlap the two regions from the top. The fifth configuration had the overlap cascading from the left region being on the bottom, followed by the MFC region on top, and then right region on top. The sixth configuration was cascading in the reverse order. Figure 4 shows the six configurations as seen from the trailing edge for better visualization.

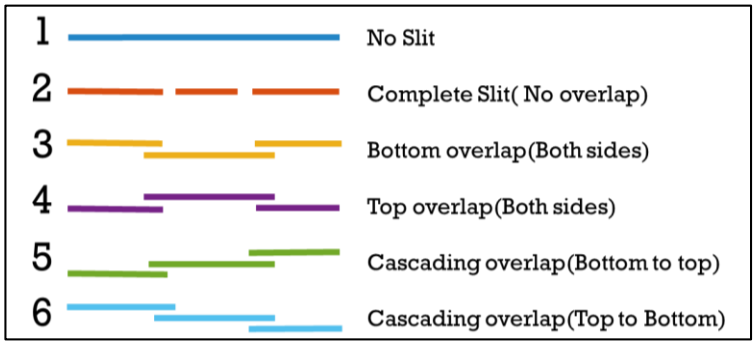

Figure 4: Tested configurations of the outboard wing

The results for both upward and downward deflection of the six configurations are shown in the Figure 5. In all cases, the most deflection is concentrated in the MFC region, which was expected. The effectiveness of MFC configuration will therefore be determined by how much deflection is produced in the other regions. One key observation in configuration 1 is the disparity in deflection between the upward direction and downward direction. The main reason for such a large difference was attributed to the complex curvature of the wing model, which stiffens the wing in the downward direction. Another important observation was the deflection in the inboard region for configuration 6 in the upward direction, even though there was no overlap. This was also due to the way the wing rests when in neutral position, which tends to curve the inboard region upwards when MFC is actuated in that direction.

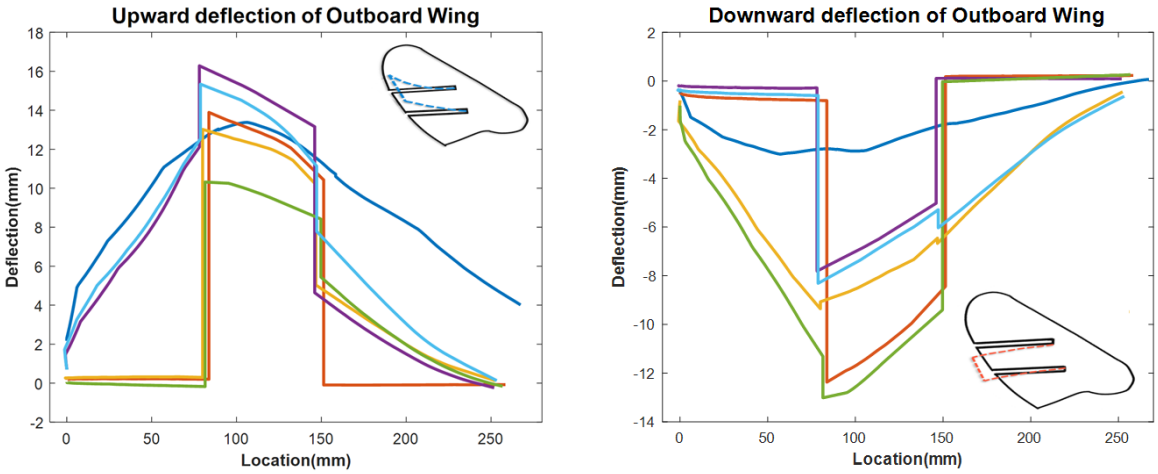

Figure 5: Deflection results for all six configurations of outboard wing

The amount of deflection created from the actuation of the MFC can be measured by looking at the total volume change under the wing. This is calculated by taking the area under the trailing edge deflection with respect to a unit chord for simplicity. The results for various configurations and both the upward and downward deflection are presented in Figure 6. The main observation was the huge disparity in deflection, for instance in configuration 1, which could lead to perverse yaw effect in the micro aerial vehicle. Configurations 2 and 3 show matching deflection results in both the upward and downward direction.

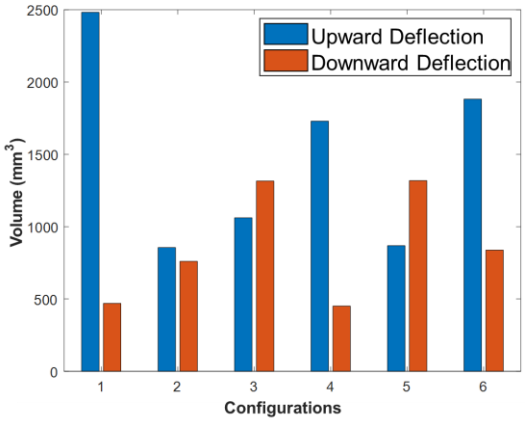

Figure 6: Volume under MFC actuated wings for various configurations

The FEA model for the full wing design with the optimized placement of the MFC angle at 60 degrees shown in Figure 7 was compared to the experimental results of the wing model shown in Figure 8. The MFC was placed in a similar location on the numerical model as in the experiment. The deflection contours for both the experiment and the FEA model are presented in the figure below. The FEA model well represented the deflections obtained from the experimental result. There was a slight variation in the magnitude of deflection obtained from the FEA model. This variation was expected as the boundary condition of the experiment was slightly different than the numerical model. There are also some discrepancies when manufacturing complex curvatures, such as the wing below, that can also account for the margin of error.

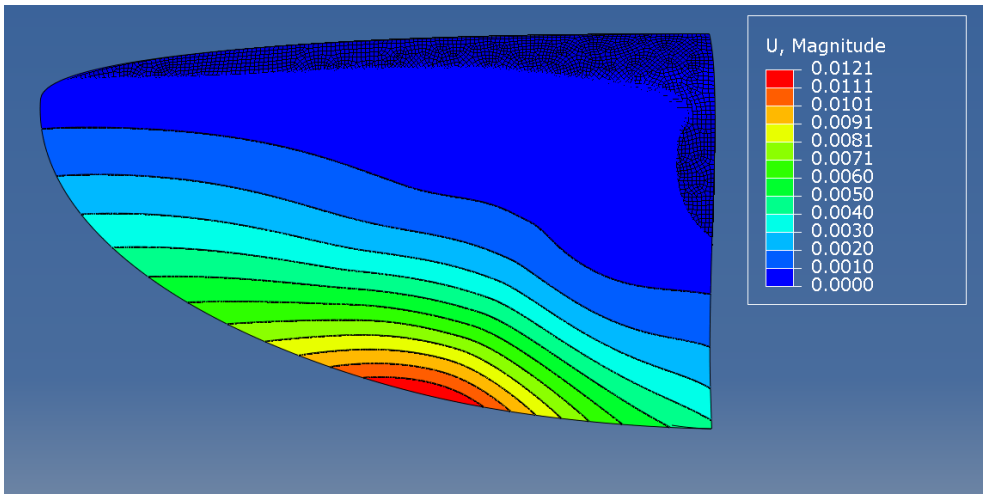

Figure 7: Deflection results from FEA of outboard wing with MFC

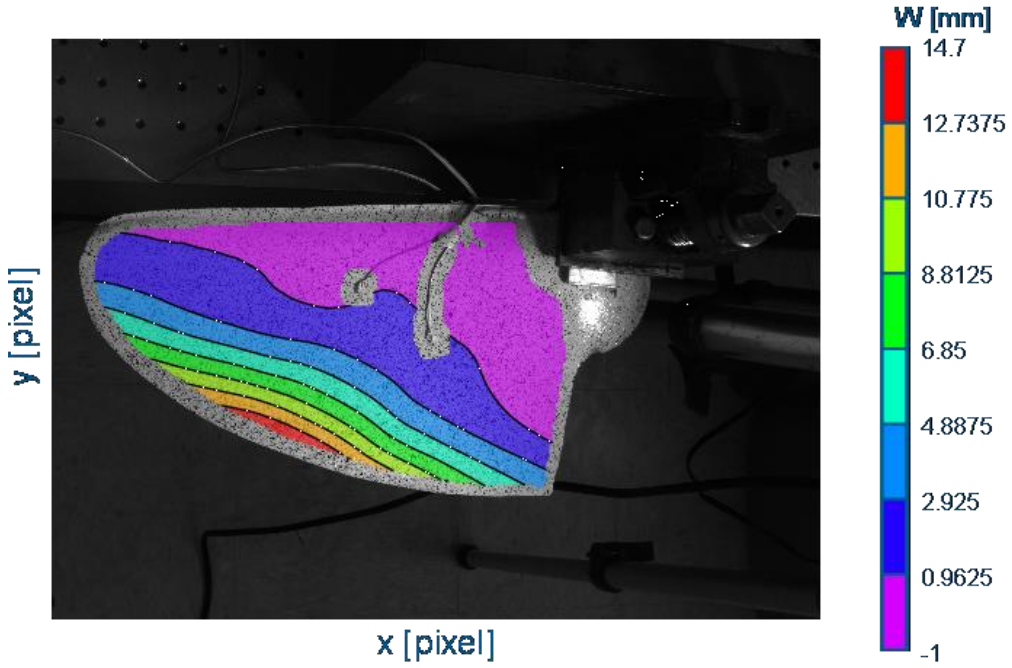

Figure 8: Deflection results from experiment of outboard wing with MFC

Modeling of Fluid Structure Interaction for Aileron Configuration

Based on previous characterization of several aileron configurations, aerodynamic models were developed to understand the effectiveness of each aileron design. Athena Vortex Lattice (AVL) is a modeling tool based on a vortex lattice method used for creating simplifAthenied models and calculating aerodynamic properties, such as the lift distribution over the span and induced drag. The various aileron configurations were inputted into the model. The ailerons for this configuration were based on the deformation of the wing using MFCs. Based on the placement angle of the MFCs, non-linear deflection along the trailing edge were achieved. It was necessary to interpolate the deflection values obtained from the DIC data to match the span sections of the AVL model. In addition, the maximum deflection of each aileron spanwise section was determined by normalizing the deflection of each section to the maximum overall deflection. An exaggerated deflection to observe the implementation of the aileron deflection can be observed in Figure 9.

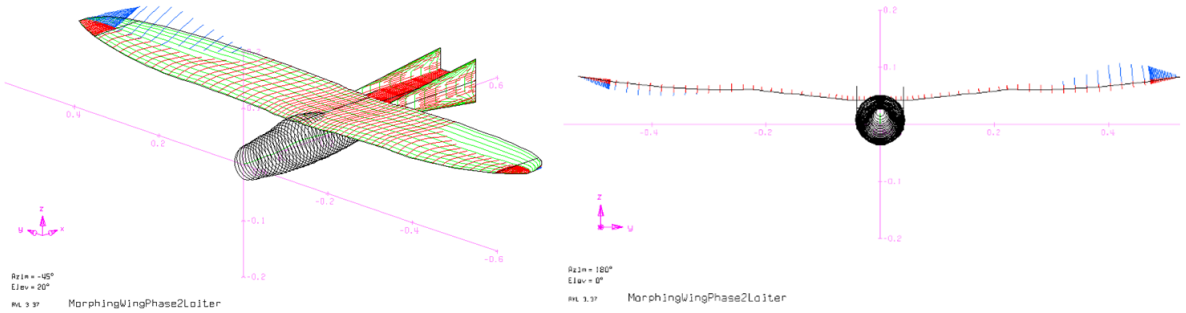

Figure 9: The AVL model of the vehicle highlighting aileron deflection (left) and Front view of the deflection for both sides of the wing (right)

The six configurations previously reported were modeled. These configurations varied based on different overlaps in the outboard section of the wing. After modeling the various configurations in the AVL model, the aileron deflections were set to 10 degree and the vehicle speed was set to 18 m/s. The resulting roll moment coefficients were compared between different configurations. The result is presented in Figure 10. The result showed that the fifth configuration had the highest roll moment coefficient. The main factors for determining effectiveness of the ailerons are the actuated area and distance from the center of gravity from the vehicle. Further investigation is required to understand the effectiveness of the ailerons with a change in the wing sweep of the outboard section.

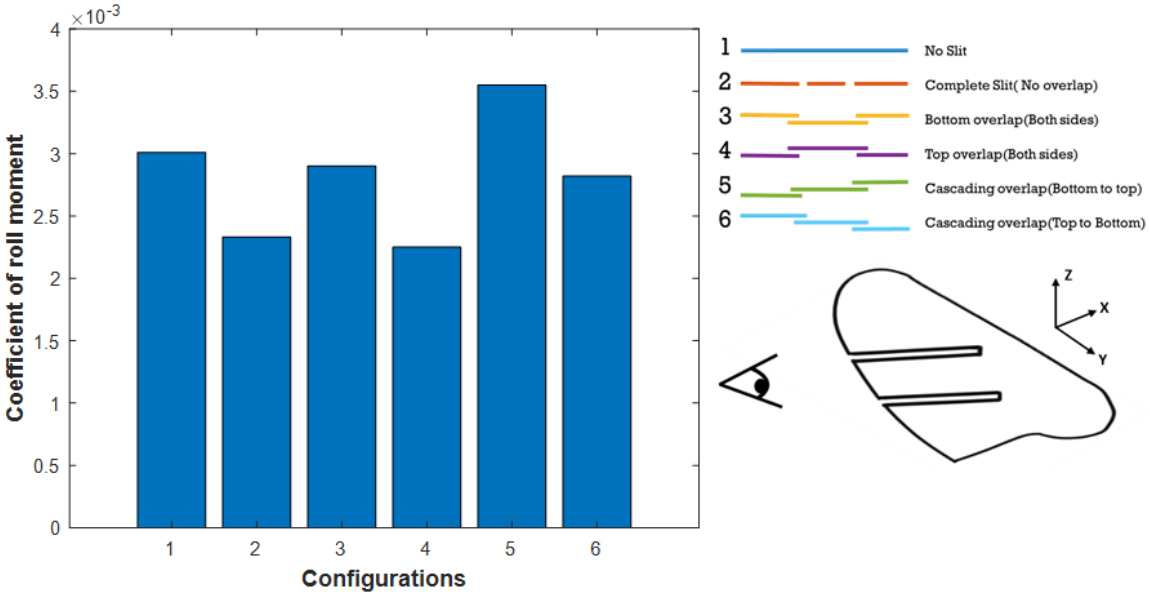

Figure 10: Coefficient of roll moment for each configuration based on the AVL model

Aerodynamics Characteristics of Variable Sweep Wing

To further understand the performance of the vehicle when the outboard wing is swept incrementally, it was necessary to develop the wing planforms for each sweep angle. As such, MATLAB was used to automatically generate the wing design based on the desired sweep angle. Some examples are presented in the Figure 11. For this study, it was necessary to use a single airfoil for the entire wing. The change in the airfoil shape due to the sweep angle was not considered, since similar results were observed for a thin uncambered airfoil shape.

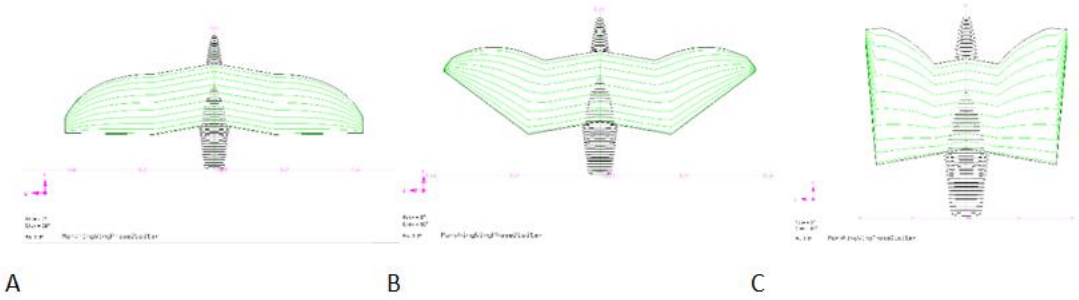

Figure 11. Aerodynamic model of the wing section at A) 0º sweep B) 45º sweep C) 90º sweep

Analysis shows that as the wing sweeps backwards, the aerodynamic center of the wing shifts backwards as well. The shift in aerodynamic center results in a higher static margin, requiring significant deflection from the tail in order to trim the vehicle. The sweep angle of the inboard fixed section was explored to find a sweep angle that can mitigate the effects of the outboard wing sweep. Four different angles of the inboard sweep were explored, starting from zero degrees (no sweep) with a forward sweep increment of 10 degrees each. At each inboard sweep angle, the neutral point of the wing was measured for the total sweeping angle of the outboard section. The results can be seen in Figure 12. As seen in the figure, there was significant drop in the neutral point position past the 60 degree sweep of the outboard wing. Continued investigation is underway to understand the non-linear change of the static margin due to inboard sweep.

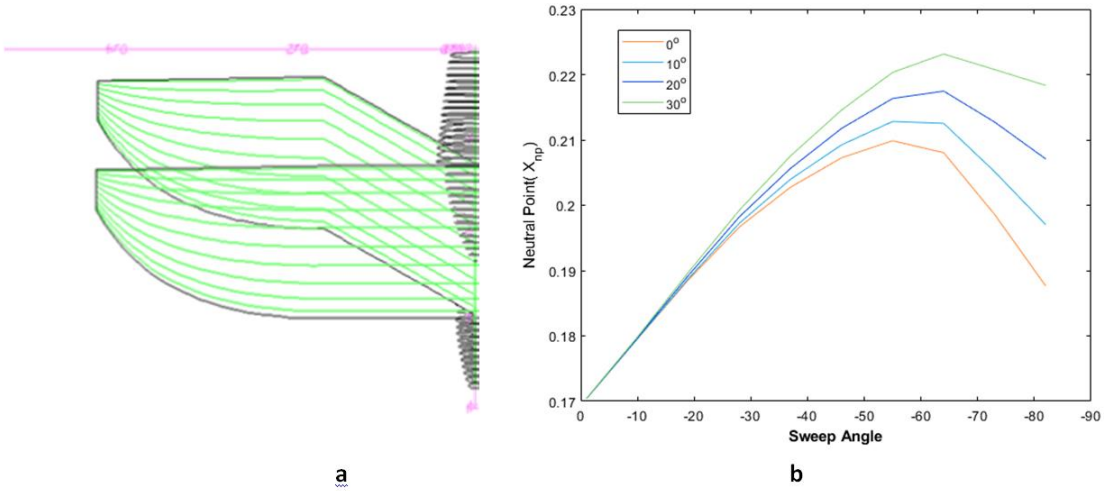

Figure 12: a) Comparison of inboard sweep angle b) Neutral point vs outboard sweep graph for various inboard sweep angle

Wind Tunnel Testing

A test vehicle, previously used for flight tests, was used as a test asset for wind tunnel testing. The wind tunnel test was mainly for quantifying the characteristics of the vehicle at different air speeds and to determine the effectiveness of MFCs as ailerons. The wind tunnel that was used, determined by the size of the vehicle, was located at the University of Florida Research & Engineering Facility (REEF) which is located adjacent to Eglin Air Force Base. The wingspan of the vehicle when fully extended is 42 inches, which could not be studied under the wind tunnel available at the main campus. Preliminary analysis was conducted to understand the operation of the wind tunnel, as well as prepare for more detailed experimentation.

The deflections of the control surfaces and the response to the various wind speeds were measured using DIC. This method uses stereo cameras and a unique random pattern on the object to measure deformations and deflections. Two cameras were used to capture the out-of-plane deflections of the ailerons. The most effective method of creating this pattern on the test vehicle was using spray paint. The wing of the vehicle was spray painted with an even coat of white paint followed by a speckle pattern using black paint. Cameras were mounted on the base of the test stand, which served as a rigid mount for capturing images. The vehicle was mounted on a fixture that was available at the wind tunnel facility. The vehicle was mounted upside down on the fixture, since the cameras were mounted on the base. This setup was viable because the effect of gravity on the light-weight wings could be neglected. The area of interest of the camera view was adjusted to look at one side of the wing. The wind tunnel set up is shown in Figure 13.

Figure 13. Wind tunnel setup with vehicle on mount (right) and Speckled pattern on wing of the test vehicle (left)

The main objective for this study was to determine how much deflection can be achieved at various wind speeds. LabVIEW was the main tool for operating the various aspects of the wind tunnel. The lift and drag characterizations were reserved for another time due to limitations at the facility. There was full control over air speed in the tunnel. A separate system for recording and capturing DIC images was brought in with the test vehicle. Using this full setup, the vehicle ailerons were deflected in the positive direction to identify the baseline deflection value. While maintaining this deflection, the air speed was increased to 5 m/s and 10 m/s. This process was repeated for the downward deflection as well. The result for three locations along the trailing edge of the outboard wing are presented in the Figure 14.
Based on the above results, there was significant change in deflection when the air speed was increased. At 10 m/s, there was about 6 mm of change in the maximum deflection. There is need for further analysis using fluid-structural interaction models to better optimize the placement of the MFCs as well as understand the aerodynamic properties of the vehicle. Similar characteristics were observed in both the upward and downward deflection of the ailerons. Even though there seems to be a decrease in the overall deflection as air speed increases, the flight tests have shown sufficient roll control during maximum flight speeds.

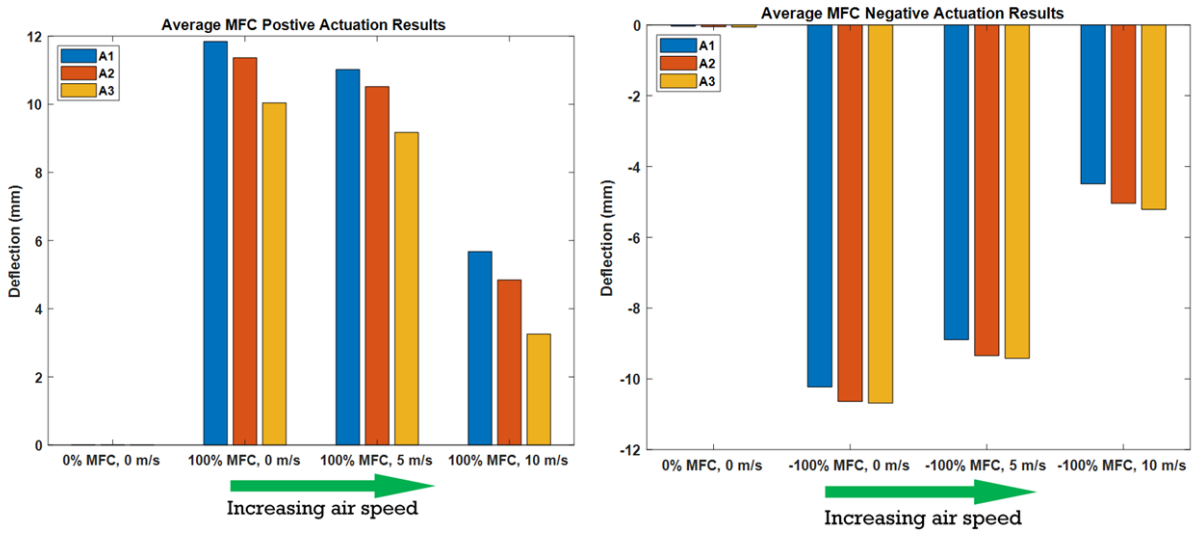

Figure 14. (left) MFC deflection for positive actuation, and (right) Average MFC deflection for negative deflection

Tail Design

Iterations of Tail Design

FEA models for each section were developed to study the implementation of MFCs on the control surfaces and their effectiveness. The main challenge was understanding the behavior of MFC actuators while the MFCs are experiencing aerodynamic loads. For these FEA model simulations, the aerodynamic loads were modeled by introducing a distributed load into the model. The various sections of the elevator had different layup configurations. The root and base sections of the elevator were layered with quasi-isotropic layup of the composite to ensure maximum stiffness. Unidirectional carbon fibers were used as a substrate for the middle section of the elevator where the MFC were placed. This substrate was chosen because unidirectional fibers yield the maximum deflection compared to other layup of composite. The section surrounding this MFC region was layered with ± 45 degree layers to ensure maximum compliance when the MFCs are being actuated. There were three locations of the MFC that were explored. MFC was placed closest to the root of the elevator, in the middle, and closest to the tip of the elevator. These locations were modeled with a distributed load, as well as without one. The results can be seen in Figure 15.

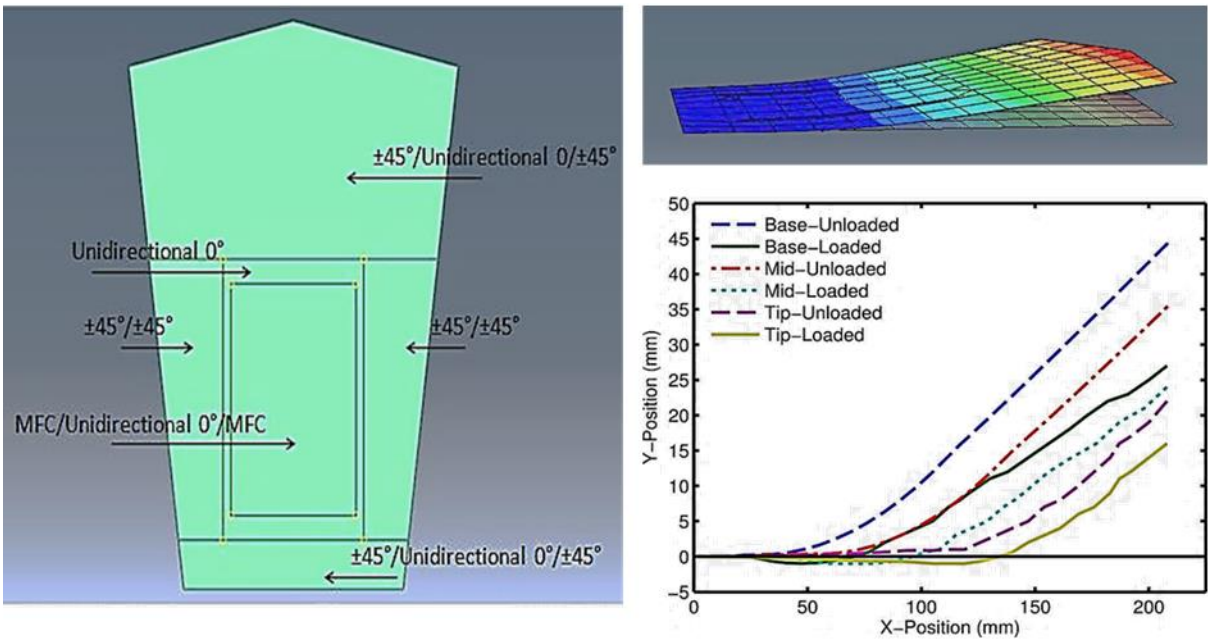

Figure 15. Initial design study of elevator section with MFC actuator

There are several design configurations that will be considered for this vehicle to achieve sufficient control as well as resemblance to a real-life bird. The first design is the V tail configuration. This configuration would incorporate two MFC actuated section on each side of the V shape with a compliant middle section made of silicone rubber sheet, so as to remove any restrictions from the stiffness of the material to the motion of the MFCs. The second configuration is the X tail configuration. This configuration has the advantage of silhouetting well when looking at the bird from any given direction. Two actuated sections will also be used for this configuration occupying the top two sides of the X shape. The other design is the H shape configuration. This is a configuration with an elevator that is end-plated on each side. This configuration has a middle section, which is the only actuated section in this configuration. This configuration provided a significant cost reduction because of the reduced number of MFC actuators needed. The actuation schematics for these different configurations can be seen in Figure 16.

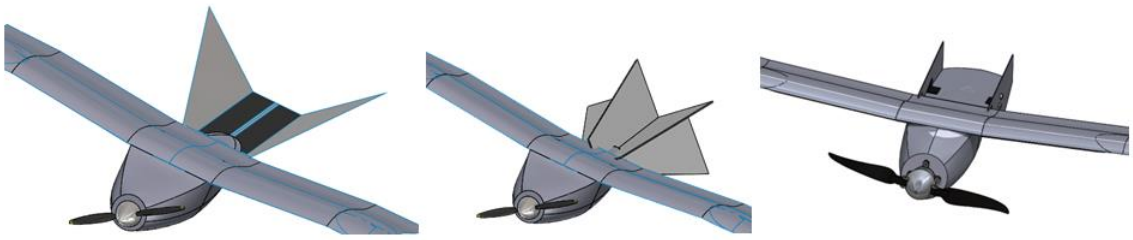

a b c

Figure 16. a) V tail configuration b) X tail configuration and c) H tail configuration models of the tail section

The overall aerodynamic performance of the different configurations needed to be studied to understand the efficiencies of each design. Qualitative measures were defined in order to determine which design visually resembles more closely to a bird. Several low-fidelity models using AVL were created to determine the performance of the vehicle under aerodynamic loads. MFC actuators have a limited range in the amount of deflection they can generate. Finding the design that maximizes the use of MFCs and achieves sufficient control of the aircraft was the design study objective. Some of the different tail configurations studied are shown in Figure 17.

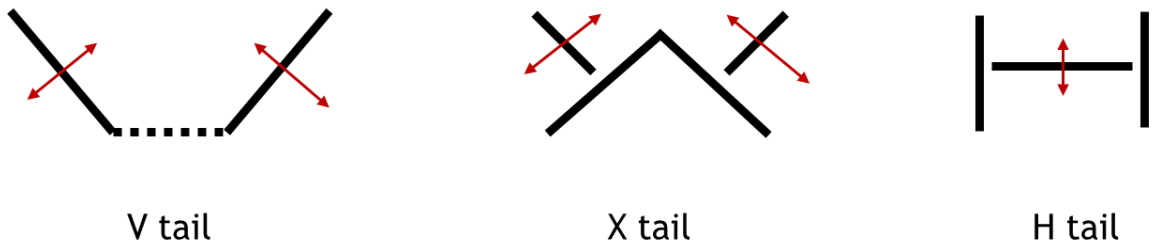

Figure 17. Different configurations of the tail with actuated sections

The tail configurations were modeled in AVL alongside the wing from the previous section, as shown in Figure 18. The MFC deflections obtained from the cantilever setup were used to determine the maximum deflection that can be produced in the tail section. The hinge location and maximum angle was determined for each model. The compliant section for the V tail configuration was assigned a fraction of the deflection as a response to the actuated section. The quantitative measure for the effectiveness of the tail configuration was based on the change in pitch moment per actuation angle of the MFCs. The study revealed that the H tail configuration yields the best results. The H tail configuration was further analyzed to understand the effectiveness of the end plates compared to a conventional elevator. The result showed an 18% decrease in the required deflection using end plates to maintain trim flight. This decrease in the required deflection is mainly due to the restriction of air movement from the top layer towards the bottom, thereby reducing induced drag and flow separation that occur at the edges. The H tail design was selected as the configuration to be used on the demonstration flight test vehicle.

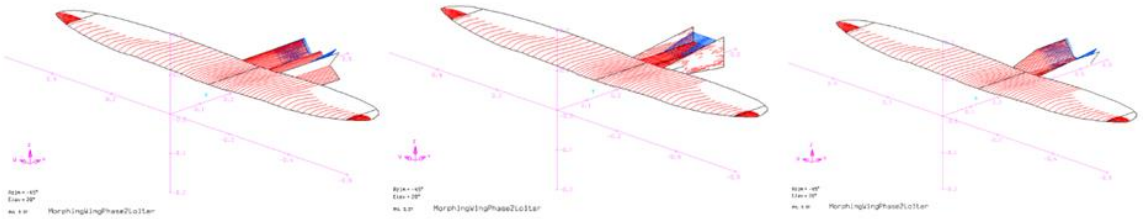

Figure 18: AVL model of tail configurations coupled with wing section

The end plates were fabricated in the lab using 3 layer carbon fiber prepreg. The middle section with the MFC were also laid up based on the elevator study highlighted in the beginning of this section. A larger size of the MFC section was made during the composite curing process. The size and shape was trimmed down to fit the vehicle after the cure cycle was complete. L brackets were used to secure the end plates onto the actuated section of the tail configuration. These brackets were placed with sufficient gaps to ensure smooth deflection of the MFC section. Figure 19 shows the layout of the H tail configuration on board the vehicle. During the flight test, observers noted that the tail configuration silhouettes really well at various angles.

Figure 19: H tail design as seen on the vehicle

Wing Sweep Mechanism

Sweep Profile

In order to keep a streamline surface at the overlap between the inboard and outboard portions of the wing, a unique geometry must be developed to minimize surface discretization. The design of the sweep profile aims to reduce surface separation while minimizing surface traction at the root of the outboard wings. Part of the outboard airfoil, from the location of max camber to the trailing edge, at the intersection of the inboard leading edge and the outboard leading edge, is first rotated about the spanwise axis of the wing [Equation 1]. This rotation gives an inherent washout to the outboard wing, mitigating failure due to tip stall, while having a geometry mimicking a natural avian wing. The estimate is that for every one degree of rotation about the span, there is 3.16 degree of washout between the root of the outboard and the tip; the recommended is that a span rotation of less than 1.5 degrees be used. Another rotation is created about the axis of rotation 90 degrees out from the intersection to create the base design of the outboard wing [Equation 2]. Note that the rotations are taken with respect to the dihedral angle of the wing and not the global coordinate system [Figure 20].

$$\{\boldsymbol{X_{washout}}'\} = [\boldsymbol{R_{span}}]\{\boldsymbol{X}'\}\ for\ \boldsymbol{X}' \in [\max camber, trailing\ edge] \quad \text{(Eq. 1)}$$

$$\{\boldsymbol{X_f}'\} = [\boldsymbol{R_{rotate}}]\{\boldsymbol{X_{washout}}'\} \quad \text{(Eq. 2)}$$

Where:

$\boldsymbol{X}'$ are the coordinate points with respect to the dihedral angle in the local coordinate system;

$\boldsymbol{R_{span}}$ and $\boldsymbol{R_{rotate}}$ are rotations about the spanwise axis and axis of rotation, respectively.

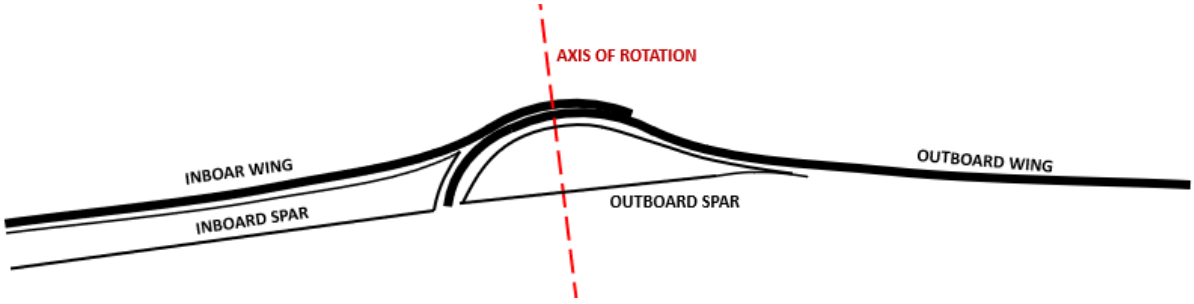

Figure 20. Front view schematic at the intersection of the sweep profile. The natural curvature generated between the outboard and inboard sections of the wing mimic the design of most avian predators. The axis of rotation is tilted to with respect to the dihedral angle of the wing.

The sweep profile was originally implemented for both inboard and outboard sections of the wing; however, the result led to an inconsistent lifting surface with questionable reliability. Additionally, a natural wash-in was generated, which is unfavorable for aircraft stability. The spar designs for the inboard and outboard wing modules were fabricated in a manner that did not interfere with sweep motion, as shown in Figure 21.

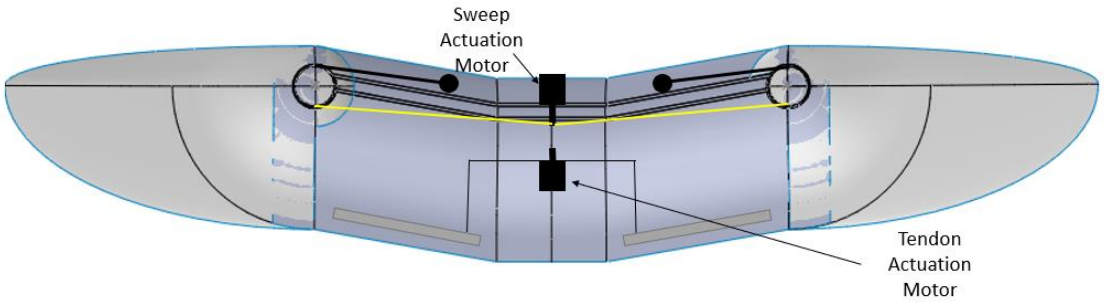

Figure 21. Spar and elbow joint hybrid mechanism integrated into the morphing wing. An integrated rotary cuff design is introduced at the intersection between the inboard and outboard wing sections. The yellow line represents the tendon actuator pulling the wing via motor propulsion. Springs are attached to the opposite ends of the joint to retract the wing forward.

Iterations in Sweep Actuation Design

Development of the initial sweep actuator did not come without issues. For instance, the design of the spring constant needed was required to not only resist friction between the two wing sections, but to also remain static under aerodynamic loading until the tendon actuator was activated. This required spring constant parameter, in addition to spatial restrictions, made the tendon actuator a rigorous and difficult design to implement. Other methods were introduced to improve upon prior iterations. Table 1 contains a summary of each attempted design concept, their advantages, and disadvantages.

Table 1. Summary of Sweep Actuation Designs

Design	Advantages	Disadvantages
Tendon actuator with elastic recovery	• Minimal vertical space required • Moderate in plane space required • Simplistic mechanics, design around one load bearing component	Linear elastic spring must be designed around external forces (friction forces Motor performance restricted to the torsional resistance of elastic spring plus external forces Highly coupled system – requires minimal margin of error – external forces are detrimental
Coupled tendon actuators	• Minimal vertical space required • Simplistic mechanics, design around one load bearing component • Motor designed around external forces alone	• Requires high volume of in-plane space to work (wiring tangles otherwise) • Sensitive to out-of-plane motion (must be in-plane or system fails) • Very small margin of error
Rigid-body mechanism	• Simplistic mechanics, design around one load bearing component • Rigid body motion provides predictable path (easy to design around) • Motor designed around external forces alone	• Questionable amount of in-plane and out-of-plane space required • More susceptible to complete failure upon impact than other systems

Finalized Prototype Sweep Actuation Mechanism

The final design of the sweep mechanism propagated on the initial humerus spar and elbow joint concept. The spar in the finalized design was fabricated to be more streamlined, where the inboard section would appear to have a thick profile transitioning to a thinner profile past the spar's trailing edge. The spars shown in Figure 22 were manufactured to reduce module interaction between the inboard and outboard wing sections. The elbow joint was adapted from a rotary collet design to a pinned joint using thrust bearings. Actuation of the sweep mechanism would utilize a hollow aluminum rod attached to the leading

end of the elbow joint. A servo motor is activated in the fuselage of the vehicle and rotates the outboard wing using the rod about the pinned joint, akin to rigid body motion. This design was able to achieve a wing sweep of about 80 degrees when fully actuated. Note that the outboard wing is pocketed underneath the inboard spar when fully swept; lubrication was required to reduce friction.

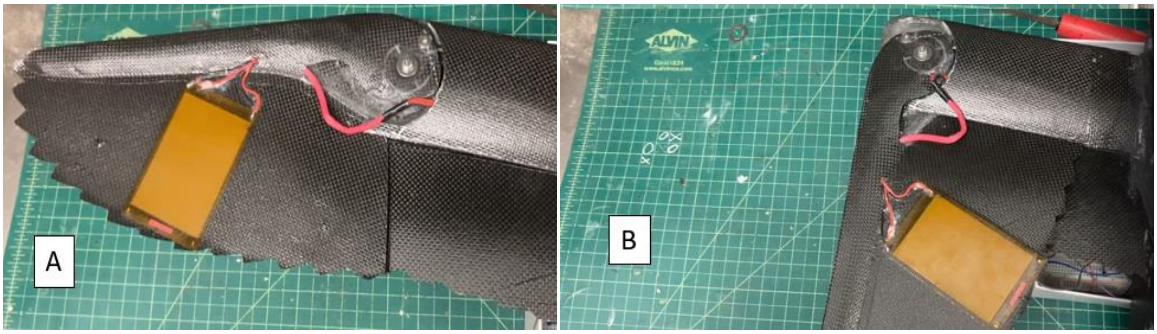

Figure 22: (A) Outboard wing fully swept forward. A thrust bearing is integrated into the foam-carbon fiber laminate at the joint section. Washers, a bolt, and nut were used to pin the two joints. (B) The outboard section is swept by actuating a servo linked to an aluminum rod through the inboard spar. The servo pushes the rod spanwise and creates a clockwise (counter-clockwise in the figure) motion about the pinned joint. Portions of the outboard wing are tucked underneath the inboard spar. Lubrication was applied to reduce friction between the modules.

Material Studies and Characterization

The biomimetic morphing wing prototypes are primarily fabricated using AS4 plain weave carbon fiber-epoxy composite prepregs. This material was implemented based on its marketed high longitudinal modulus and minimal ply thickness, making it apt for aerospace structures requiring high specific strength. However, as a substrate in a MFC bimorph configuration, AS4 plain weave was not suitable due to its orthotropic equivalency in longitudinal and transverse properties; AS4 unidirectional is substituted instead.

In order to characterize the composite properties of AS4, tensile-DIC testing was performed on ten 0-degree and ten 45-degree test coupons, as shown in Figure 23. Each coupon is fabricated specific to dimensional sizes detailed for ASTM D3039 standards (250 x 25 x 2 mm^3). Garolite tabs were fabricated (40 x 25 x 3.175 mm^3) and adhered to the test coupons via structural epoxy; this prevents the vice grips from puncturing the test coupons, causing premature failure through a concentrated stress at the ends of the coupons. Strain is measured using DIC. In order to measure two-dimensional strains, cameras were placed equidistant on either side of the coupon. This camera placement will negate out-of-plane displacement values once collected data from both cameras are averaged.

Figure 23: Tensile test on AS4 carbon fiber test coupon. Speckle pattern is applied to both sides of coupon. DIC cameras are placed on both ends of the coupon to average out through-thickness deflection.

A table of properties is presented in **Appendix B** for tested composites along with manufacturer's specifications for the MFCs**.** MFC properties are

presented with a virtual thermomechanical variable that will be discussed in a later section. Note that the reported average value for out-of-plane shear moduli (G23, G13) from testing are given as a variable range. The assumption is that the behavior of the fiber reinforced prepregs is focally planar. All out-of-plane stresses are then considered negligible. However, smaller values other than the recommended values are ill-advised if the given material is analytically evaluated; smaller out-of-plane modulus may result in potential yielding/buckling through the thickness of the composite, reducing the accuracy of analysis. For textile composites, G13 and G23 can be assumed equivalent to G12. This assumption can be used for unidirectional composites, though in the case of unidirectional composites, the assumption is not necessarily correct.

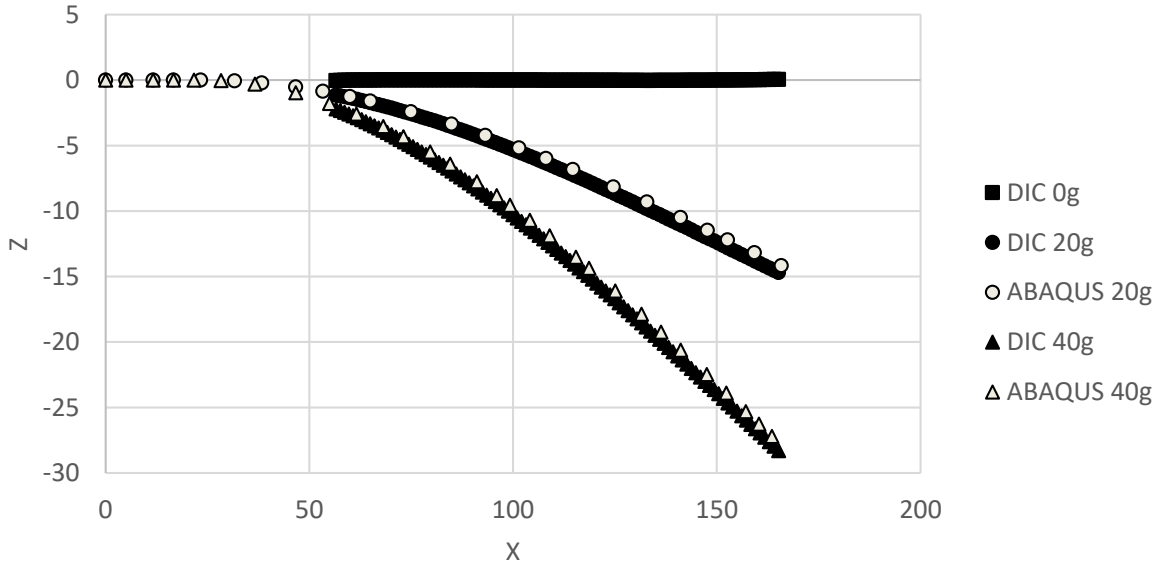

Figure 24: Cantilever beam comparison between experimental digital image correlation results to ABAQUS finite element analysis. Tips were loaded using a 20 gram and 40 gram weight scale at the free end. The fixed end of the laminate was held using a vice.

The material properties were validated by using DIC testing to compare a tip loaded cantilever beam experiment to a finite element method (FEM) using ABAQUS. Figure 24 displays graphical results of both methods. The in-plane shear modulus, G_{12}, is calculated using the following set of equations derived from the constitutive relation for orthotropic materials, assuming plane stress.

$$\tau_{12} = -\sigma_x cos\theta sin\theta$$

$$\gamma_{12} = -2cos\theta sin\theta\varepsilon_x + 2cos\theta sin\theta\varepsilon_y + \gamma_{xy}(cos^2\theta - sin^2\theta)$$

$$G_{12} = {}^{\tau_{12}}/_{\gamma_{12}}$$

where γ_{12} and τ_{12} are the in-plane shear strain and stress, σ_x is the global longitudinal stress, and θ is the fiber direction. ε_x, ε_y, and γ_{xy} are the global longitudinal strain, transverse strain, and in-plane shear strain.

MFC Bimorph Hysteresis Studies

In-lab experimentation and prior literature has determined that MFCs exhibit a phenomenon known as hysteresis. Hysteresis occurs when a material is subject to deformation under load but does not return to its original state when unloaded. Hysteresis complicates the use of MFCs as control surfaces since positional error may lead to unwarranted maneuvering. Though vehicle data rates can contravene this issue, a proper study needs to be considered in-case compensation is required.

Experimental Testing

Appropriate equipment and model setup are necessary in order to capture the hysteresis path history. DIC was used to observe the output displacements and strains. Figure 25 shows the experimental test bed. The MFCs were actuated using a power source that provided 10.5 V of potential with appropriate current. The voltage signals were supplied to the MFC using an AVID LLC™ MFC high-voltage driver. Input was controlled via Digilent™ Analog Discovery 2 waveform generator using analog voltage signals. This device also logged input data using a voltage divider of one 10,000 and ten 1,000,000 ohm resistors; this was necessary since the logger could not read voltages above 10 V. The data logger has a 3 mV resolution. Displacements were recorded using 12-36mm varifocal lens fastened to specific DIC cameras with 300 μm positional resolution. Additional lighting was provided to minimize shutter speed. All modules and data were controlled and stored in an operating system with essential softwares.

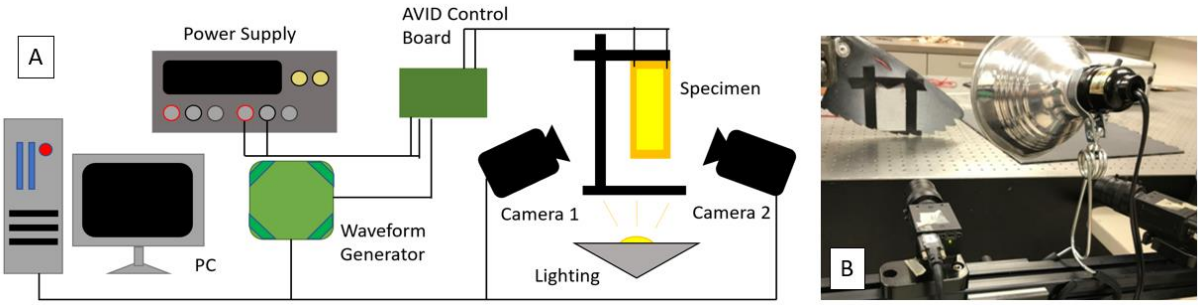

Figure 25: (A) Illustrated schematic of DIC test bed for hysteresis studies. Power is supplied to the AVID board which actuates the MFCs. Signals are inputted into a coupled OS and transferred through the waveform generator onto the MFC specimen. The waveform generator also collects voltage data from the MFC. Dual cameras were used to capture out-of-plane motion, with an additional light source provided to reduce shutter speed and increase frequency. (B) Image of the test bed. Test observes a wing tip specimen deflected to capture hysteresis. Cameras were placed further apart during testing.

Wing Tip Boundary Effects on Hysteresis

Four variations of wingtip specimens were studied to analyze the behavior of hysteresis as a function of the wingtip design (Figure 26). Fiber orientation and geometric contour were used as control variables. Two sets of specimens would be manufactured so that the global fiber orientation was parallel to the polarization direction of the MFC; the other two would have global fibers 45-degrees with respect to the MFCs to reduce boundary stiffness. Additionally, two specimens would have their trailing edge tips scalped/segmented to diminish the multi-curvature about the MFC as well as reduce the hardening-softening effects of the geometry.

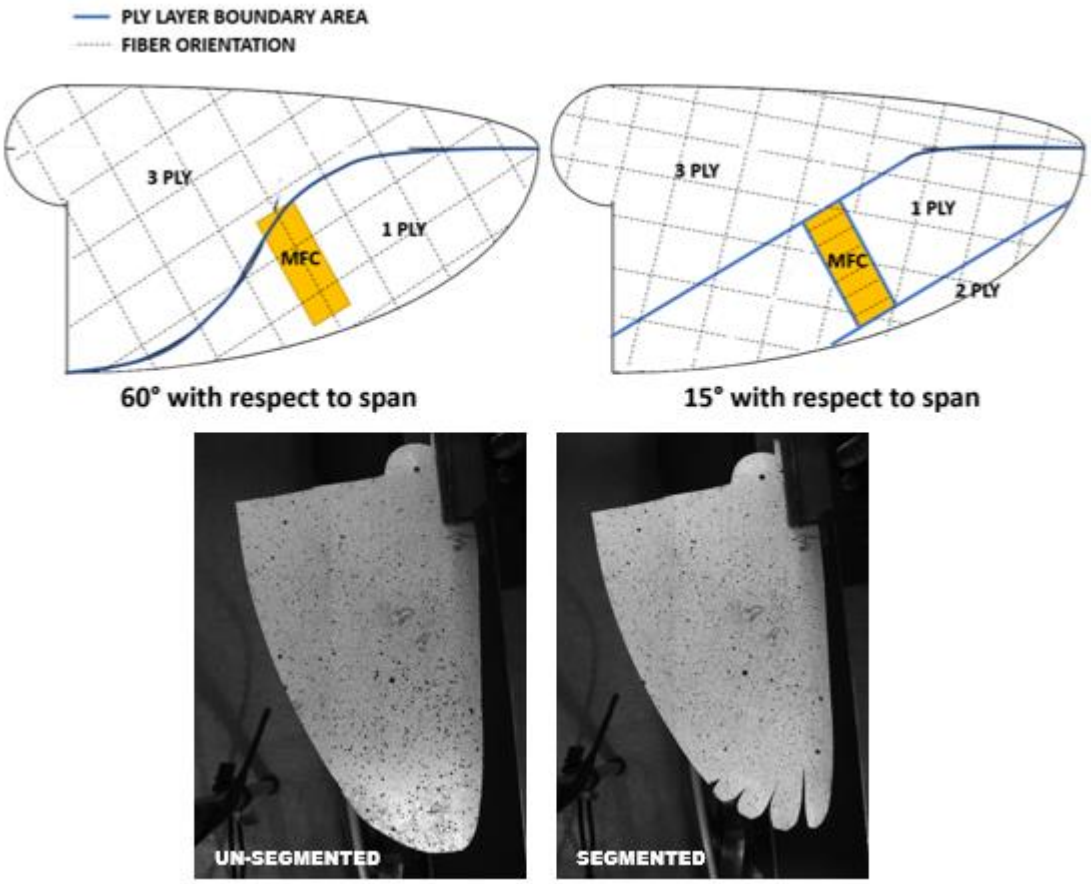

Figure 26: Visual parameter change of each specimen undergoing deformation.

The wingtips were actuated upwards (away from ground) to their maximal position before being relaxed to neutral. The displacements for each specimen along the trailing edge were captured and recorded as shown in Figure 27. Evidence from experimentation provides a counter to hysteresis, at least with respect to the design of a wingtip. An overall reduction in boundary stiffness and curvature promotes hysteresis behavior. Reducing the freedom of elements around an MFC can mitigate positional error; however, full actuation magnitude is compromised, as shown in **Appendix B. Appendix B** also provides hysteresis strain as a function of actuation rate and curvature, to be archived for reference.

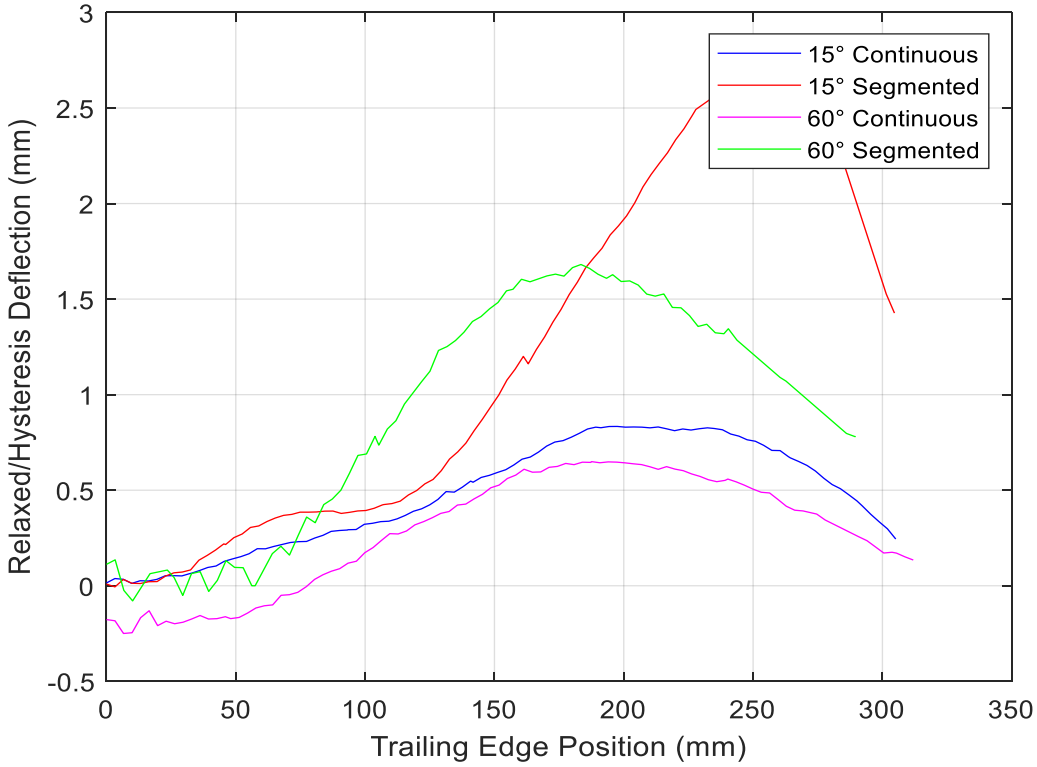

Figure 27: Hysteresis due to relaxed actuation. Fabricated specimens are as follows: (blue) plies 45-degrees to MFC and unsegmented, (red) plies 45-degrees to MFC and segmented, (majenta) plies parallel to MFC and unsegmented, and (green) plies parallel to MFCs and segmented.

Hysteresis Compensation

To counteract the effects of hysteresis using control input, in-case vehicle rates and boundary designs are not apt, a study was performed using an empirical method developed by Chang-Lining. A profile is first acquired without compensation to extract necessary parametric points (Figure 28). These points are then fitted onto a surrogate model, where compensated voltages were outputted to achieve ideal positioning. DIC recorded hand-actuated input commands using recommendations from the compensation model. The result yields higher agreement between the compensated and ideal positioning. For MFCs used as control surfaces, especially in autonomy, this compensation model is valid for improving flight authority.

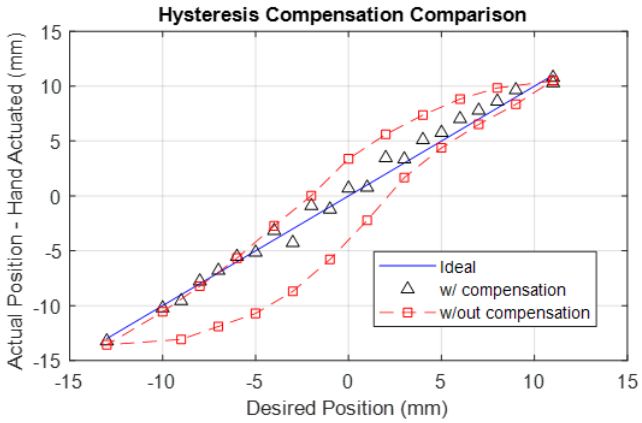

Figure 28: Hysteresis profile on a flat specimen with integrated bimorphs (red). A compensation model was developed using a technique introduced by Chang and Lining (ref. 1). Actuation of the specimen as recommended from the model reduced the overall hysteresis (black) improved agreement with the ideal path (blue).

Considerations For Creep

In addition to hysteresis, the MFCs display a progressive displacement behavior at a held actuation load, similar to creep models. DIC displacement data for a flat specimen with integrated bimorphs is located in **Appendix B**. Unlike real creep models, the progressive displacement observed from the MFCs saturate after a certain period of time. Though the theory on this phenomenon is still under research, the global magnitude it has on vehicle performance is negligible. Creep can be compensated for using a further surrogate model developed by Chang and Lining.

Fluid-Structure Interaction Studies

Analytical and experimental results achieved through static conditions alone is inadequate to visualize the full effect of aerodynamics onto a wing structure, i.e., deflections recorded through ground testing may not reflect those acquired during flight. Fluid-structure interaction (FSI) is a method of applying aerodynamic load onto a physical structure in order to determine a converged, predicted objective. Figure 29 shows a FSI flowchart, where the objective is displacement convergence. The geometry is first modeled into a flow solver and outputs pressure data. The mentioned data is then applied to a physical model of a deflected wing using MFCs. Displacements are recorded and magnitudes are compared against prior iterations to evaluate structural convergence. This method is generally cheaper for design purposes compared to wind tunnel testing. However, validity of the model requires physical evidence to compare against.

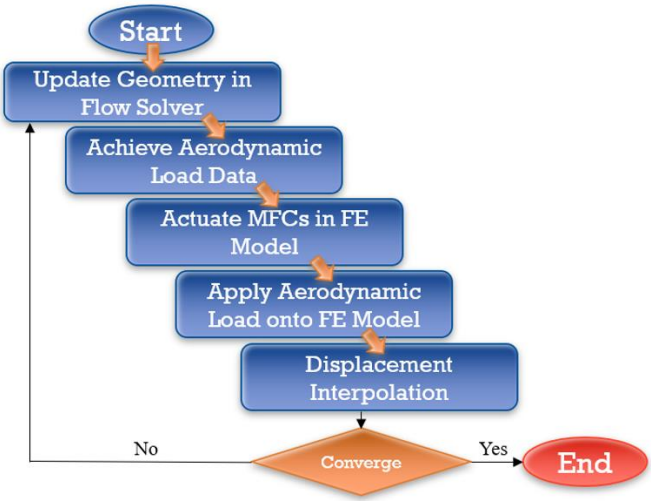

Figure 29: Flowchart of fluid-structure interaction study performed on an MFC integrated specimen. The objective in the chart is displacement, where convergence is achieved if the magnitudes of displacement from the last two iterations are similar. The displacements are added to the geometry in the flow solver if convergence is not achieved, and the next iteration initiates.

FSI Modeling

Before FSI studies, understanding of the intermediate models is necessary. The flow solver will be conducted using Athena Vortex Lattice (AVL), a program that uses Biot-Savart Vortex Panel theory to solve for pressure distribution. The vortex lattice model is adequate for determining the lift distribution along the surface of a wing; however, formulations for drag are dependent on results induced by lift. An empirical model for drag needs to be extracted from aerodynamic data in order to establish a well-defined solver.

For the physical solver, ABAQUS CAE™ finite element program is sufficient. ABAQUS is popular for research and academic studies since its base programming is rooted in finite element theory, which can be adapted to any user defined model. A model of the wingtip with MFCs was paired against its experimental counterpart (Figure 30) and results show good agreement. MFCs were modeled as functions of temperature inputs to mimic piezo mechanical control, as discussed in theory in **Appendix B.**

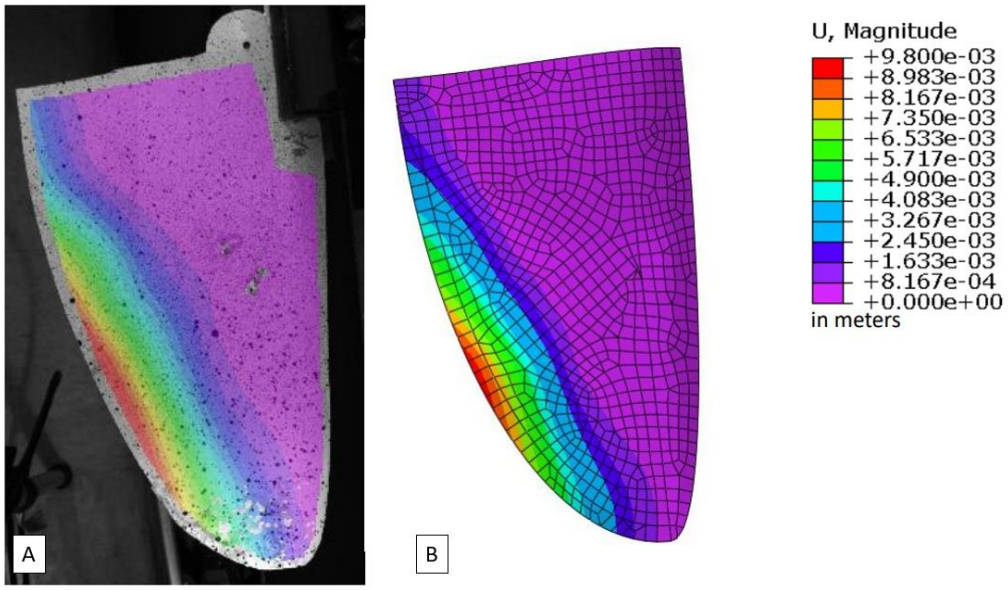

Figure 30: (A) Digital image correlation of out-of-plane displacement of a wingtip specimen versus (B) its finite element model counterpart. Distribution between the two models show apt agreement. Contours are presented in meters for out-of-plane displacement

Tail FSI Study

To quantify the aerodynamic effects onto an MFC displaced structure, a coupled fluid-structure simulation was performed on a simple flat cantilever beam. The orientation of fibers and MFC placement mimicked that of a fabricated tail for the Morphing Wing vehicle. A physical representation of an actuated MFC-host structure was modeled using finite element analysis (FEA) in ABAQUS CAE™. The geometry was imported into AVL to incur pressure loads. Loads were then imported onto the FEA model, shown in Figure 31, to attain a new deflection. The maximum deflection of the tail is in competition with the aerodynamic loads provided by AVL. Iterations between ABAQUS and AVL persisted until the tip displacement converged. Figure 32 depicts the difference in deflection in-between iterations before convergence.

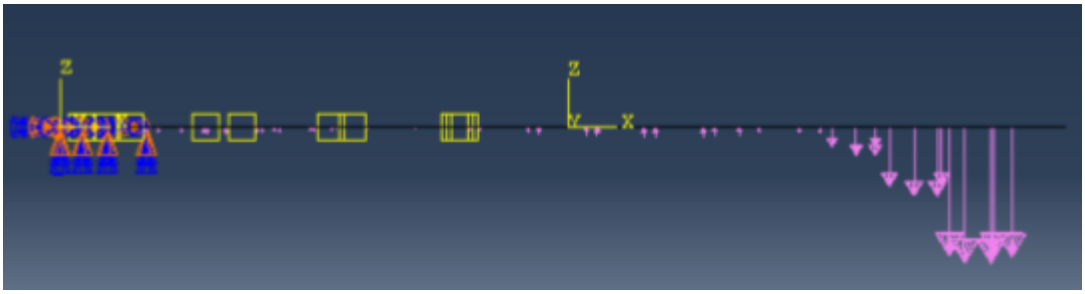

Figure 31: AVL pressure data applied to a FEA model of a laminate cantilever beam in ABAQUS. Yellow indicators reflect the location of the MFC on the beam.

Initial and converged deflections are recorded in Table 2. Pressure data was acquired using 0, 5, 8, 12, 15, and 25 m/s airspeeds. From the data, increased airspeeds impede tip deflection as a result of increased body pressure. However, the data pertains only to the set configuration addressed in this particular simulation. In order to preserve the quantified results onto different configurations, a mapping of pressure as a function of curvature was developed through numerical poly-fitting.

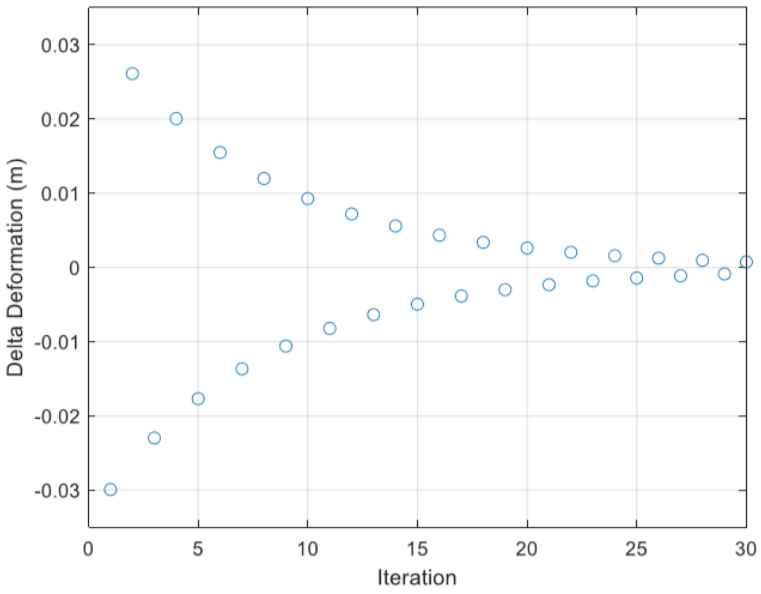

Figure 32: Plot of maximum tail deflection versus iterations using FSI at airspeeds of 25 m/s

Table 2. Final tail deformations for varying airspeeds

Airspeed (m/s)	Initial Deformation (no airflow) (mm)	Final Converged Deformation (mm)	Delta Deformation (mm)
0	43.0	43.0	0.0
5	43.0	40.99	-2.01
8	43.0	39.40	-3.60
12	43.0	36.58	-6.42
15	43.0	34.22	-8.78
25	43.0	27.16	-15.84

$$-712.45\theta^3 + 383.62\theta^2 - 63.86\theta + 3.13 \quad (3)^*$$

$$-679.89\theta^3 + 350.14\theta^2 - 55.28\theta + 2.50 \quad (4)^*$$

$$-765.89\theta^3 + 364.21\theta^2 - 52.82\theta + 2.16 \quad (5)^*$$

$$-882.01\theta^3 + 390.71\theta^2 - 52.63\theta + 1.99 \quad (6)^*$$

$$-1581.2\theta^3 + 531.4\theta^2 - 53.8\theta + 1.5 \quad (7)^*$$

Note: Equations 3-7 refer to the resultant pressure acting upon a singularly curved piezo-actuated surface for airspeeds of 5, 8, 12, 15, and 25 m/s, respectively. Utilizing these equations in tandem with established laminate theories enables full-field investigations on varying configurations of single-curved MFC-host structures.

Control System Studies

The bimorph MAV research drone is a biomimetic fixed-wing vehicle inspired by the peregrine falcon. The MAV, shown in Figure 33, is designed to serve as a reconnaissance drone that uses its avian silhouette to hide in plain sight. To be successful, the MAV must dash from launch to target, yet also loiter for as long as necessary when making observations. These disparate mission requirements lead to competing design choices for the wing shape and size. To optimally accomplish both dash and loiter requirements, the MAV is designed to mimic the peregrine falcons' ability to sweep its wings. To reduce the weight and mechanical complexity of the swept wings macro fiber composites (MFCs) actuate the MAVs three control surfaces. These are located on each outboard wing and the horizontal tail. When excited with high voltage at low current, the MFCs control the carbon fiber skin's bending. The use of independent variable-sweep wings for vehicle morphing and aerodynamic control and MFCs for control surface actuation makes the MAV's control design unique.

Figure 33. Bimorph micro air vehicle (MAV) top view

The MAV has six independent degrees of freedom, labeled in Figure 34. These are right and left flapperons, elevator, left and right-wing sweep angles, and a fixed-pitch variable revolutions per minute (RPM) propeller. Symmetric wing sweep and variations in the propeller RPM provide control of the MAV's lift and drag forces for trimming at different flight conditions. The three control surfaces and two wing morphing degrees of freedom provide five inputs used to control the vehicle's aerodynamic forces and moments. These are used in the innermost vehicle control loop for stabilization. The vehicle is over actuated because there are five control inputs to stabilize three body moments. Flight testing has shown that the vehicle's yaw stiffness is sufficient for directional stability. Direct control of vehicle yaw is not required to maintain trimmed stable flight.

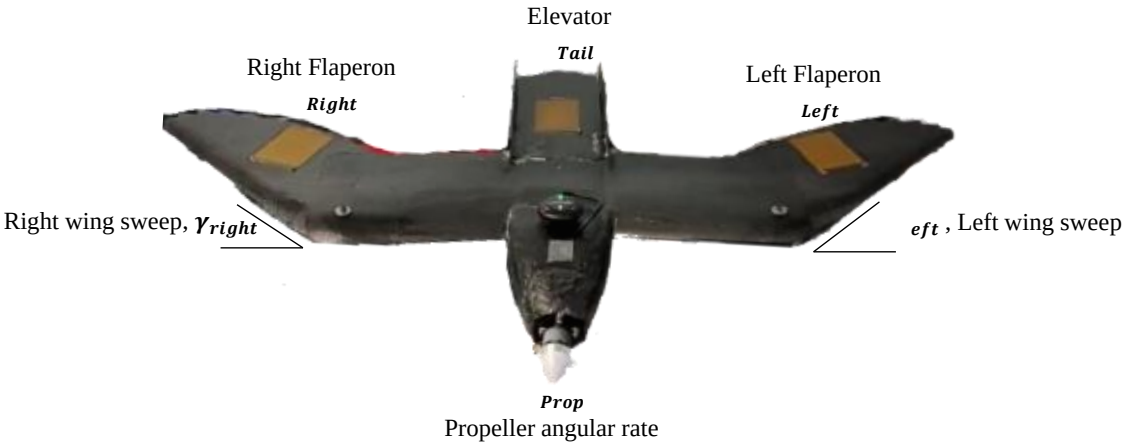

Figure 34. Degrees of freedom on MAV

Table 3 shows the combinations of control deflection inputs to body moment outputs. The choice of a control allocation scheme is not unique. A suitable control allocation scheme must account for the fact that the flapperons' location on the outboard wings couples their effectiveness with wing sweep angle. The authority of the flapperon attenuates as the wing is swept. The control allocation scheme used on the MAV is scheduled based on average wing sweep angle, blending from using the MFC as primary control inputs to using variable-sweep as the primary control input at severe sweep angles. The variable-sweep actuators were chosen to have sufficient bandwidth to perform inner loop control tasks.

Table 3. Control allocation combination table

Moments controlled		
Roll, l	Pitch, m	Yaw, n
$\frac{-}{2}$	$\frac{+}{2}$	$\frac{\gamma \quad -\gamma}{2}$
$\frac{\gamma \quad -\gamma}{2}$	$\frac{\gamma \quad +\gamma}{2}$	

The control of the MFC themselves is a unique problem. The piezoelectric MFC patches exhibit hysteresis and creep on the order of ten percent of full range deflection. In practice, these effects are mitigated by the vehicle attitude controller. The current MAV has no direct observation of MFC deflection. Instead, the control loop is closed directly by the body rotational rate feedback. This strategy has shown adequate tracking of the desired body rotational rates during trimmed flight. Laboratory investigation of using collocated strain gages as strain feedback for closed-loop MFC control is ongoing. The MAV includes an onboard flight computer that provides data logging and a full range of autonomy modes, from manual to automated missions. The hardware used for the flight computer is an off the shelf Pixhawk 4 selected for being inexpensive and open source. A diagram of the avionics in the MAV is shown in Figure 35. Here the flight computer integrates a telemetry radio, flight control radio, and sensor suite with high voltage driver boards that control the MFC and outputs to the motor and variable sweep servos. Onboard sensing includes GPS position, fused vehicle state estimation, air data, control outputs, and mission event logging. The data is logged at a high rate and stored on an onboard SD card eliminating packet loss. A subset of the flight data is sent to a ground station in real-time for gain tuning, vehicle control, mission planning, and vehicle health monitoring.

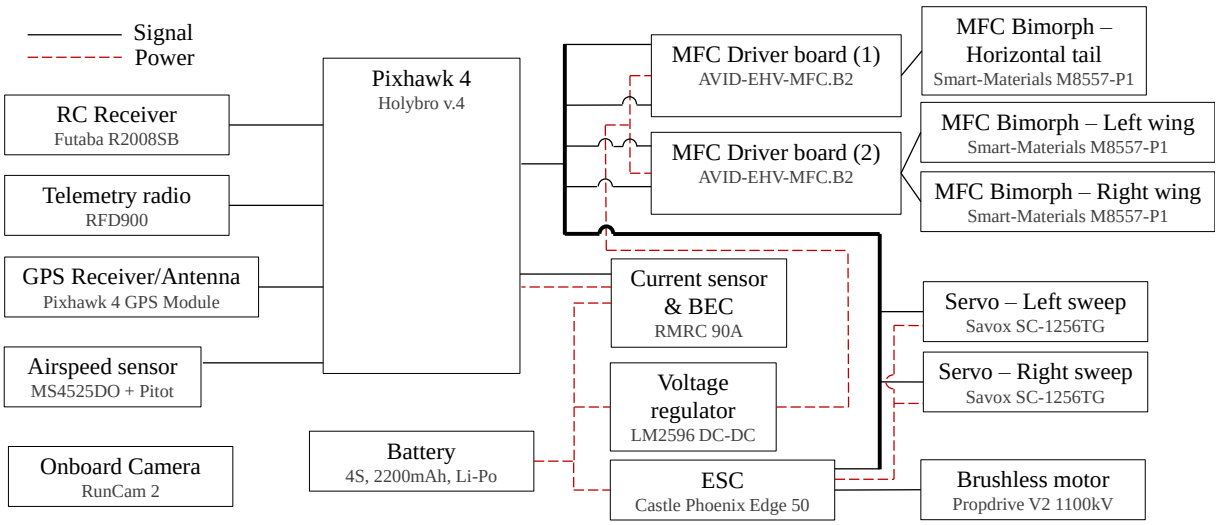

Figure 35. Avionics diagram of MAV

The MAV controller can be considered as two independent loops. An outer guidance and navigation loop, Figure 36, and an inner attitude control loop, Figure 37.

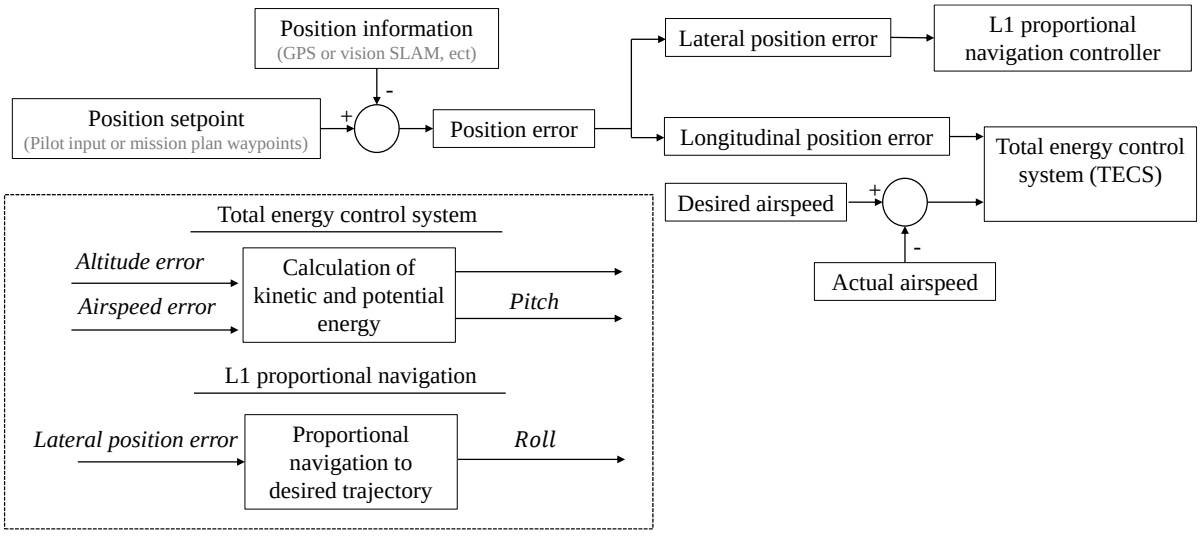

Figure 36: Guidance control diagram

The outer loop is responsible for the navigation and guidance to locate the vehicle in space. The loop takes GPS or vision-based earth frame location data as an input and compares this with the desired set of positions such as waypoints or loiter circles in a mission plan. The error is computed and guidance is generated based on an L1 proportional controller to track flight paths and a total energy control system (TECS) for longitudinal control. The desired trajectory is followed by prescribing a desired vehicle attitude state. These controllers have limits to provide realistic guidance trajectories for the vehicle to follow. The inner loop controller stabilizes the vehicle and tracks vehicle attitude set-points. A proportional-integral controller for each rotational axis takes an estimated vehicle attitude as an input and provides a corrective attitude command output. These attitude commands are translated into control outputs based on a control allocation algorithm. Three successively more complicated control allocation schemes have been designed for the MAV. As shown in Figure 37 these are labeled fixed sweep, symmetric sweep, and symmetric and asymmetric sweep. The fixed sweep allocation is the only unique control allocation with flapperons used for roll control and elevator used for pitch control. Successful manual and autonomous control has been tested with this allocation scheme. The second allocation

scheme adds symmetric variable sweep control to the first, all MFC, allocation scheme. Manual flight testing of this allocation scheme highlights the inability of the MAV to trim in level flight with significant wing sweep. Large symmetric sweep angles were used to produce a stable dive maneuver after which the wings were unswept, and the vehicle recovered stable level flight.

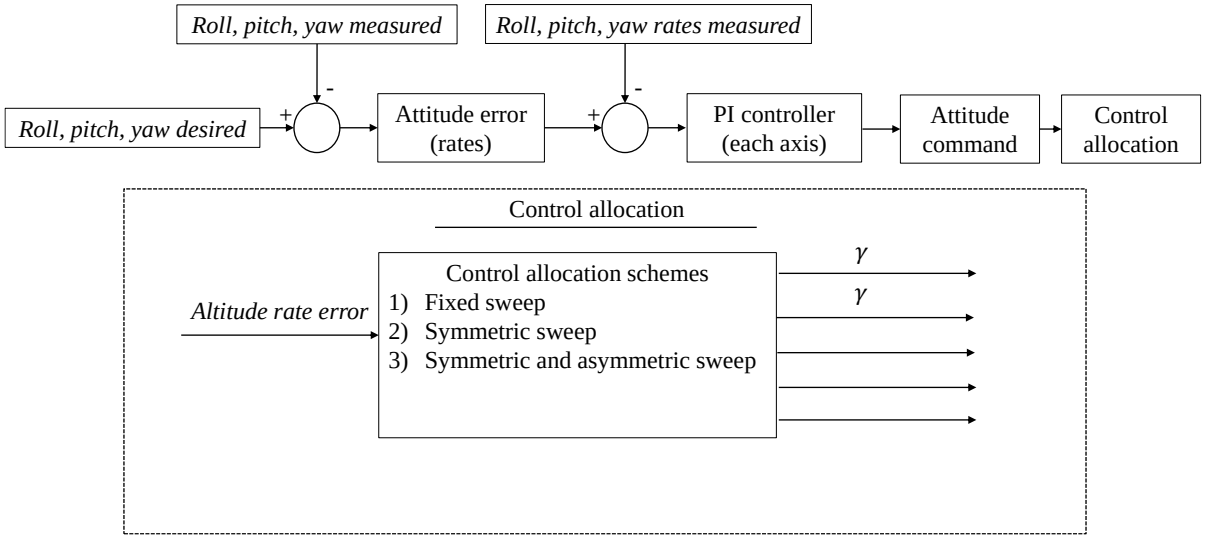

Figure 37: Attitude control diagram

The MAV is designed to mimic a peregrine falcon both in morphology and aerodynamically. When the wings are swept back symmetrically, the center of pressure on the MAV shifts aft. This shift increases pitch stiffness on the MAV and provides enhanced stability during high-speed stoop (dive) maneuvers. The large backward change in the center of pressure also makes trimming vehicle in level flight impossible. The result is that specific subsets of control allocation outputs lead to an untrimmable state. The standard way of handling this is to limit the output space to only sets of outputs that may trim the vehicle. The original reconnaissance mission requirements dictate that the MAV must fly trim and level and dive at high speeds. On the MAV this leads to two different trim states, one pitch level and one pitch down. The outer navigation loop handles when to change the pitch trim condition. The navigator loop determines if there is a large desired change in altitude, if so, the desired pitch and airspeed trim values are overridden from the TECS controller and set to align with the gravity vector and a maximum dive velocity. The control allocation then interprets this extremum as a fully swept maneuver and uses small elevator deflections to trim downwards. During the dive, the altitude error decreases until it is below a threshold value. After the error drops under 10 meters, the navigator loop commands a level desired pitch. The transitions in the vehicle state are violent and quick by design. This behavior mimics the flight of a peregrine falcon in a stoop.

The MAV leverages its morphing wings and bimorph actuators to mimic a falcon's flight across the mission profile. Given an arbitrary mission profile the navigation controller outlined in this section simply trims the vehicle accordingly. The result is an avian like flight with automatic variable sweep control. The goal of the controller design is to be simple and integrated, generating autonomous responses to navigation commands and avoiding ad hoc automated maneuvers.

RESULTS

During the period of performance for the Biomimetic Design of Morphing Micro Air Vehicles Program, many different iterations of the morphing micro air vehicle have been flown and evaluated. First flight models were non-morphing fixed wing aircraft; each individual model had a wing configuration that emulated one of the four different flight configurations for which the morphing MAV was being designed. These flight configurations included take-off/landing, loiter, aggressive maneuver, and dash

(stoop), as shown in Figure 38. The next flight models were morphing capable, but the morphing was accomplished using manual adjustments, or, eventually, servo motors and linkage rods external to the fuselage. The vehicles in Figure 38 show the servo motors and linkages that modified the ailerons and elevator. The final flight model uses micro fiber composite piezoelectric actuators to control the ailerons and elevator and servo motors to sweep the outboard wing. A version of each of these configurations has flown. There have been test flights that included the wings being swept back and then being brought back to their original configuration.

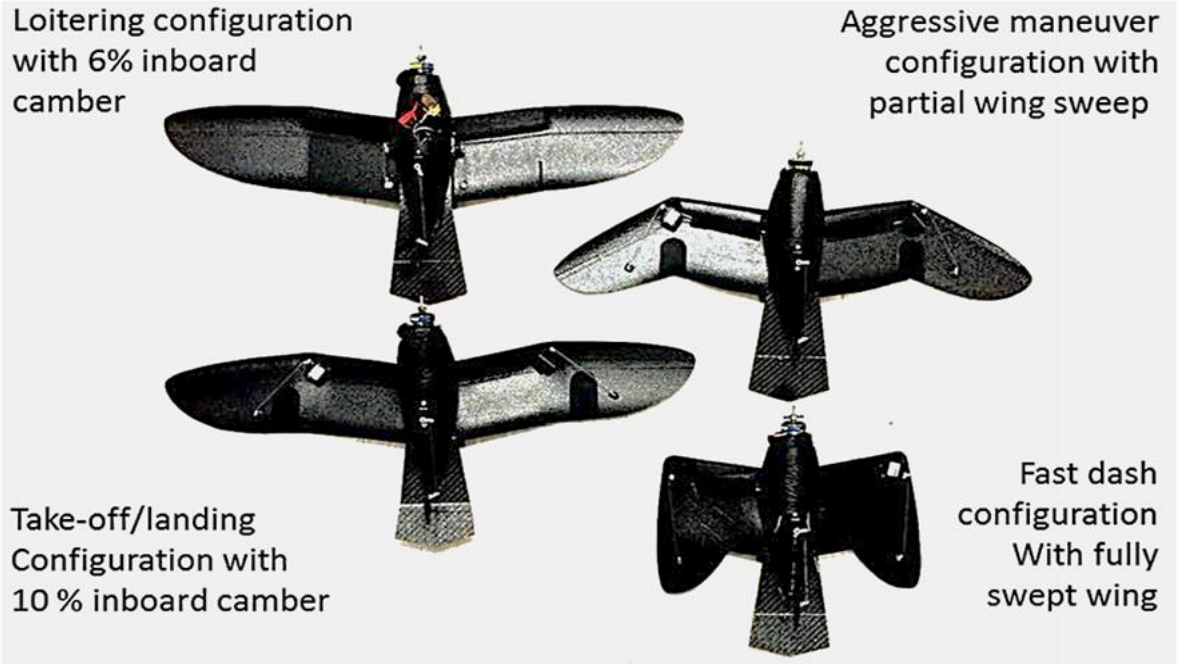

Figure 38. Four morphed configurations; initially flown in fixed position, then with servo motor actuation, then finally with MFC bimorph actuation and servo wing sweep

Full autonomous control of the MFC bimorph actuated MAV has not yet been demonstrated. In the last attempts to fly the vehicle, during final check out, the piezoelectric MFC bimorphs shorted out, rendering them incapable of providing control inputs during flight. The problem has been traced to a bad batch of MFC actuators; the company supplying the MFCs has committed to providing replacements. Another problem that was discovered was a faulty circuit design in the driver MFC driver boards; the repair to the faulty circuit design is a change in the control algorithm software.

The Micro Air Vehicle Laboratory at the University of Florida, with Air Force Office of Scientific Research permission, intends to continue working on the flight vehicle; replacing the faulty piezoelectric actuators, test flying the vehicle to determine the flight limits, and then flying the vehicle under autopilot control. During the autopilot control flight testing, the vehicle will be programmed to gain altitude, morph into a stoop (sweep the outboard wings back), dive to a programmed altitude, then flare out of the stoop into an aggressive maneuver configuration, and then pull up and gain altitude. The craft will be programmed to proceed through a series of way points while under autopilot control. The results of this flight test will be informally reported to Texas Research Institute Austin; TRI Austin will forward the results to the AFOSR technical point of contact.

Two graduate students are using the work in the Biomimetic Design of Morphing Micro Air Vehicles Program to generate the research in support of their doctoral theses. One of the students is focused on the physics of the flight vehicle, and the other student is focused on the control system.

CONCLUSIONS

Through the course of the Phase II effort, Texas Research Institute Austin and the University of Florida have investigated and demonstrated the capability of macro fiber composite piezoelectric actuators to provide control authority to an airborne micro air vehicle, allowing the vehicle to significantly change flight control surfaces and wing span in response to flight conditions and mission requirements. Initial indications are that macro fiber composite piezoelectric actuators, when tied to an autopilot control system, have the capability of controlling the aircraft in such a manner that the aircraft can be launched, assume autonomous flight, complete the assigned mission, and return for full recovery.

Highly morphing aircraft have the capability of responding to changing flight conditions, be programmed to meet waypoint check-in requirements, and to meet the schedule requirements by morphing. Highly morphing aircraft will have the ability to fly in a wider range of flight conditions because the aircraft will be able to adjust control surfaces in response to non-uniform flight conditions. These highly morphing aircraft will be able to fly to the limit of their radio control, switch to a programmed flight plan, and fly under autopilot control significantly beyond radio control range to the preprogrammed destination, then return to be within range of radio controlled flight and returned to the selected recovery point.

Highly morphing aircraft have a role to play in future Department of Defense and commercial markets.

RECOMMENDATIONS

Texas Research Institute Austin, Inc. makes the following recommendations for the further development of biomimetic design based micro air vehicles:

a) The University of Florida should be granted permission for a no-cost extension of the period of performance in order to allow the faulty MFC piezoelectric actuators to be replaced and the final flight testing program completed. This extension of the period of performance and permission to use the flight vehicle will result in completion of the flight test program and demonstration of a piezoelectric actuator controlled flight vehicle morphing to a meet a programmed flight plan.

b) The flight vehicle that is tested in the final flight test program of the Biomimetic Design of Morphing Micro Air Vehicles Program should be considered as an intermediary flight test vehicle for the Neuromophic Networks for Multifunctional Intelligence Systems Program (AFOSR MURI 2019). The control system in the current vehicle should be converted to the neuromorphic networks being developed.

c) Further funding should be considered to expand the capabilities of the final flight test vehicle in the Biomimetic Design of Morphing Micro Air Vehicles Program to include autonomous change in wing camber, tail rotation and flare, and adding controlled ‘feathers’ to the outboard wing tips. These expanded capabilities will support the AFOSR MURI 2019 objectives.

d) The Air Force should consider exploring the operational capabilities of the morphing MAV developed in the Biomimetic Design of Morphing Micro Air Vehicles Program. The vehicle is suited to carry and deploy sensors that will improve situational awareness for Warfighters in combat environments. Of special interest is the ability of the craft to fly a programmed route outside of radio contact.

Appendix A: Key Terms

AFOSR	Air Force Office Scientific Research
AVL	Athena Vortex Lattice
Bimorph	Macro Fiber Composites (MFC) aligned back to back with substrate between
CFD	Computational Fluid Dynamics
DIC	Digital Image Correlation
FEA	Finite Element Analysis
FSI	Fluid Structure Interaction
MAV	Micro Air Vehicle
MFC	Macro Fiber Composite (piezoelectric)
RPM	Revolutions Per Minute
TECS	Total Energy Control System
TRI Austin	Texas Research Institute Austin

Appendix B: Supplemental Information

OUTBOARD WING DESIGN

Modeling and Evaluation of winglets with feather emargination

Motivation

The use of non-planar wings (winglets) has been shown to be effective in increasing the efficiency (span) of an aircraft in-flight. This has both been shown both through theory and through experiment. The purpose of this initial study is to examine the role of static aero-elasticity in creating a suitable multi-element non-planar wing geometry to enhance the efficiency of the aircraft, while maintaining a span constraint.

The concept of utilizing non-planar geometry to mitigate the penalty of a shortened wingspan can be observed in nature:

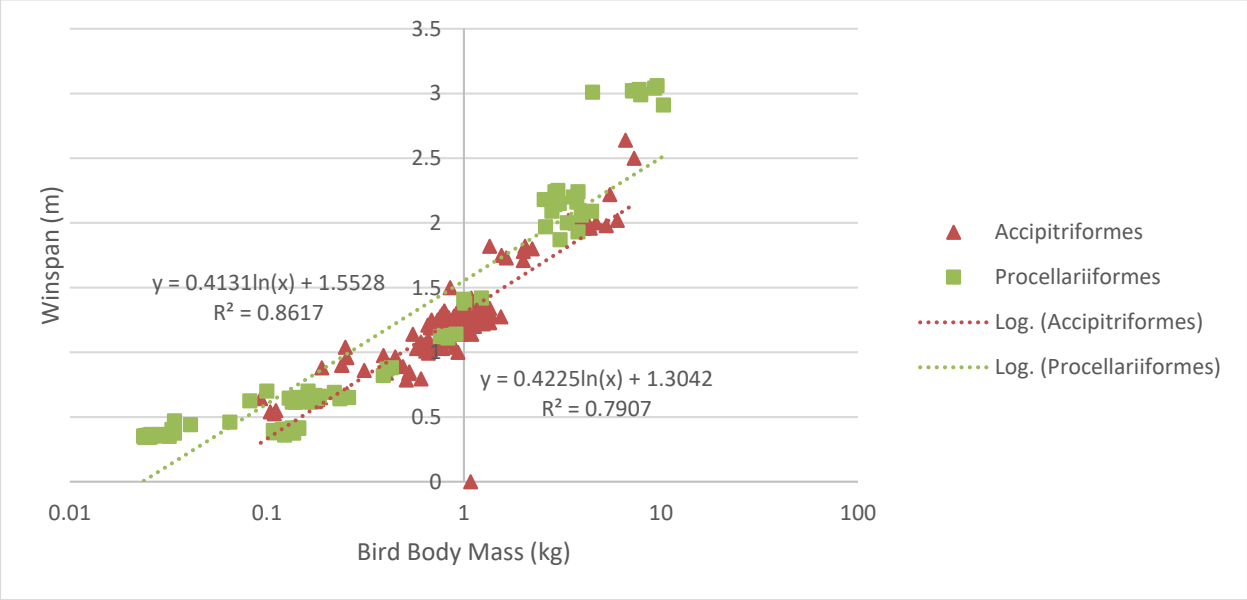

Figure 1: Allometric Relationship between Mass and Wingspan of Pelagic (Procellariiformes) and Terrestrial (Accipitriformes) birds

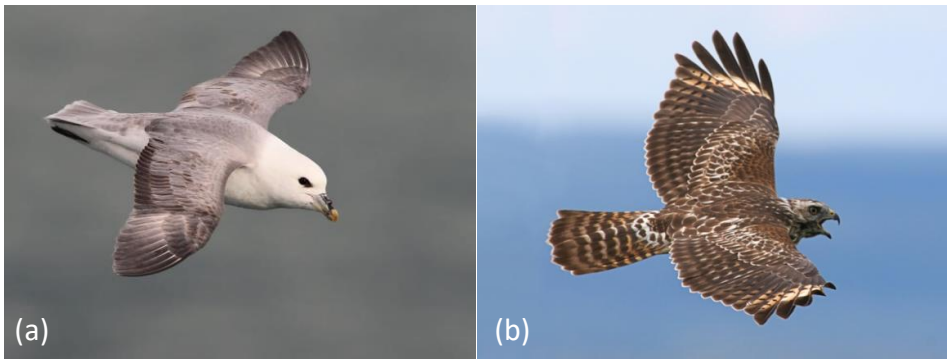

Figure 2: (a) Northern Fulmar (Procellariiform) (b) Red Tailed Hawk (Accipitriform). Both of these birds are similar in weight, but the Northern Fulmar, on average, has a longer wingspan than the Red Tailed Hawk. However, the Red Tailed Hawk has emarginated primary feathers (non-planar multi-element wingtips) while the Northern Fulmar does not.

From Figure 1 and Figure 2, we can see that terrestrial birds have about a 33% shorter wingspan compared to pelagic birds given the same weight. Basic aerodynamic theory posits that this shorter wingspan would yield decreases in efficiency. However, these terrestrial birds have been observed to have emarginated primary feathers (multi-element winglets) compared to their pelagic counterparts. Thus, it can be hypothesized that these terrestrial birds make up for their shortened span, with winglets.

Since it is desired that the aircraft being built for the Phase II will be able to switch between high speed, low speed loiter and highly maneuverable flight, there are likely to be significant trade-offs for when designing an optimal wing geometry. As such, it is desired to develop an aircraft with multi-element wing tips that make-up for any losses in efficiency that will result from any design trade-offs.

Overview
The path forward to building and flying an aircraft with multi-element feathers would be through the use of both theoretical optimization & flight testing. The current stage in the development of this design is in the theoretical stage. Our theoretical effort is based on two fronts: an aero-elastic parameter sweep for individual feather design and an aerodynamic optimization for wingtip shape. Using these results, the proper outboard wing geometry would be designed for the Phase II aircraft.

Aero-Elastic Parameter Sweep
The current generation of performance enhancing wingtip devices are rigid and heavy. While these devices are known to enhance performance, they can also be cumbersome and impose an additional bending moment penalty on the wing. The goal of our effort would be to design a wingtip device that is able to enhance performance by *aero-elastically* deforming to the appropriate aerodynamic shape required. This should allow for the corresponding device to be lightweight and flexible. This not only reduces or eliminates a bending moment penalty, but it also allows the wingtip device to be adaptable to different flight conditions. This outboard wingtip device, acts similar to the outer primary feathers of a bird – flexible, adaptable and yet rigid enough to yield performance enhancements.

The plan to achieve this lightweight, aero-elastically deformable wingtip device will be done through the use of carbon-fiber composite layers. An attractive property of composite materials it their ability to have a *bend-twist coupling* when subject to an external load. We plan on investigating this bend-twist coupling in our initial parameter sweep to identify the shapes that are possible through the use of composite materials.

This initial study will be done through the coupled use of numerical lifting line theory (*MachUp)* and a standard finite element analysis code (*Calculix.)* Both these software packages are free and open source, and have been validated. The aerodynamic results from the lifting line code will be fed into the finite element analysis code and the process would repeat (iterate) until a final solution / shape is converged. From there, the bending and twisting of the material will be noted. For the parameter sweep, the following parameters will be studied:

Independent Variables
Due to the complexity of the problem, the following independent variables will be varied. The geometry will be assumed to be a fixed rectangular planform for the sake of simplicity.

- Device Aspect Ratio (AR)
  - $AR = b^2 / S$
- Fiber Direction
  - 1 layer/direction for single ply composite, 2 layers/directions for triple ply composite
- Specified Lifting Condition (C_L)
  - Defined as a specific operating C_L for operation, which defines the load distribution
- Specified Sideslip (β)
  - This influences the load distribution across the wing
  - Can be used to study the behavior of aero-elastic bend twist coupling for swept wingtips

Dependent Variables
Based on these independent variables, the following dependent variables will be examined

- Wingtip Bending at Tip (δ)
  - This will be compared to the baseline, un-bent wing to calculate the amount of dihedral produced by the wingtip
- Wingtip Twist at Tip (τ)
  - This will be again compared to the baseline, to see the wingtip twist at the tip
  - The twist distribution will also be collected

In summary, we are seeking the following information

f(Aerodynamic Conditions, Composite Layup) = Wingtip Geometry

This information for wingtip geometry will then be used for design purposes.

Preliminary Results
The following are preliminary results from MachUp / Calculix. Given the following lift distribution:

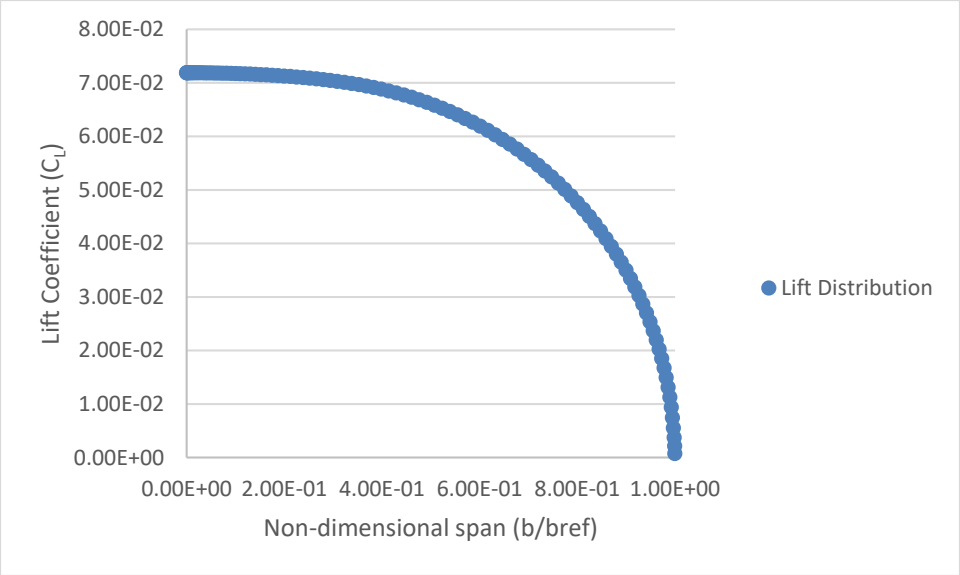

Figure 3: Lift Distribution, for Zimmerman profile

This initial lift distribution yielded the following displacements:

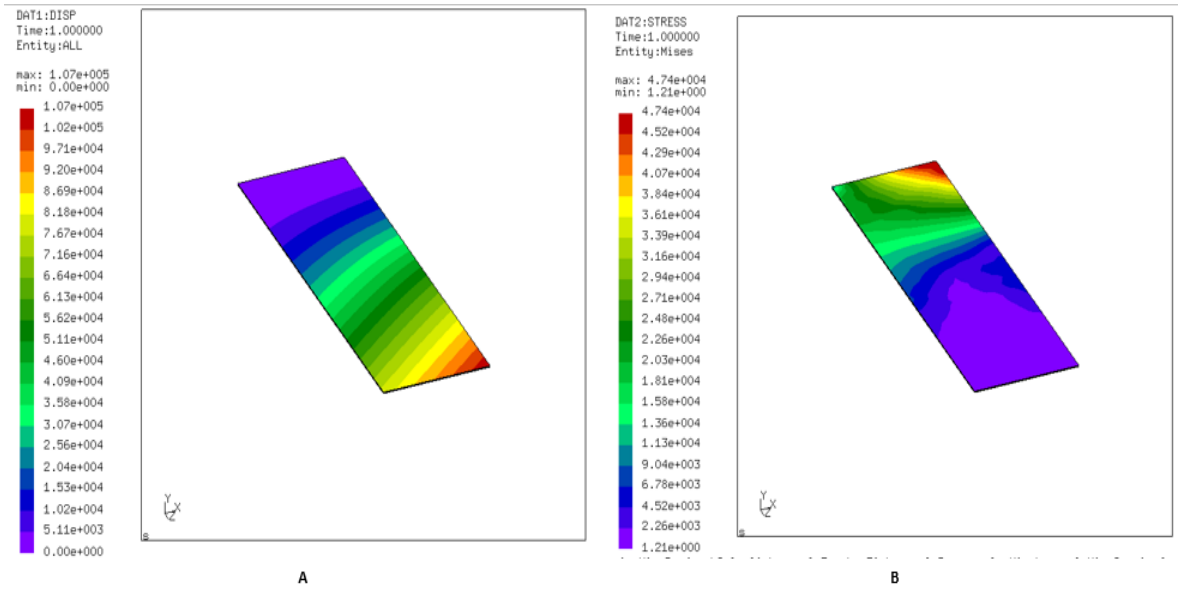

Figure 4: Calculix results for (a) tip displacements (b) tip stress distributions

The above results are not converged, and represent an initial case. The remaining step in this process is to develop and automated process to yield the accurate shape.

Aerodynamic Shape Optimization

In parallel, the effort to obtain an optimal aerodynamic wingtip geometry arrangement will be sought. As an initial case, the geometry will be based on literature. This allows for easy benchmarking, and also yields insight into the problem which could be applied to the current Phase II effort and other cases. The

geometry will be based on Fluck and Crawford (2014) and the feather arrangements will be optimized for different flight conditions. Again, the variables are as follows:

Independent Variables

- Number of wingtip feathers
- Feather dihedral distribution
- Feather twist distribution
- Feather sweep distribution
- Main wing twist
- Specified loading condition

Dependent Variables

- Induced drag

A sample result is shown from the Athena Vortex Lattice (AVL) software for a Fluck & Crawford type geometry showing an optimal feather arrangement / twist distribution for a wing to minimize induced drag:

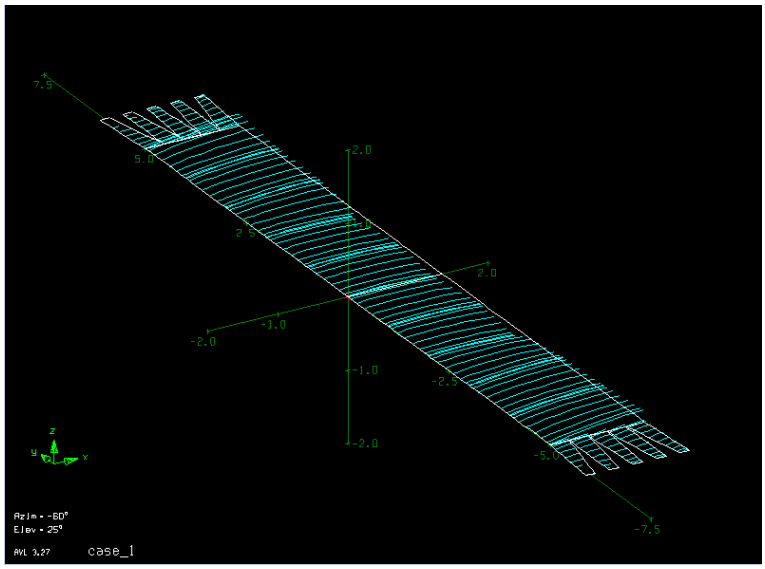

Figure 5: Wing with outboard primary feathers showing an optimal wingtip geometry arrangement

It should be noted that the results in Figure 5 represent an initial case and need to be properly verified. In addition, the calculations are now to be performed in MachUp (Lifting Line) instead of the vortex lattice (AVL) due to the use of different computer systems that the code is running on.

Modelling of piezoelectric actuator samples in Abaqus

The first step was to create a model in Abaqus that matches the experimental results obtained through DIC. Several options was considered in the creating a part module. The two best options for modelling the Macro-fiber actuators (MFCs) was either a shell planar or solid extrusion. The first design that will be explored is the shell planar.

A shell planar part was created. The rectangle was modelled and dimensions were obtained from the DIC file. The dimensions observed from the DIC seem to be a bit larger than the actual size. These

should be verified with actual measurement of the physical sample. The next step is followed by creating a partition for the MFC to be placed on top of the substrate.

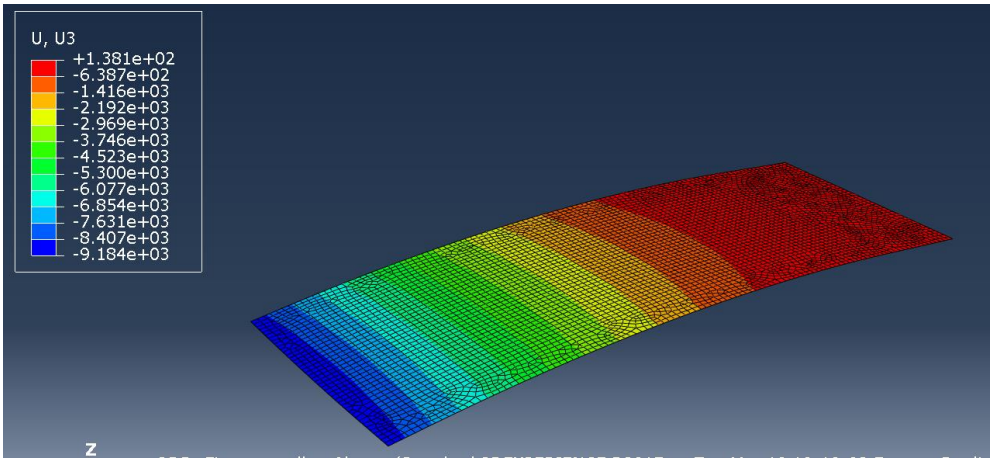

Figure 6: Modelling of an MFC actuator on a carbon fiber plate

The preliminary results look promising. The deformation values seem to be off. The next steps include checking the units of the measurement values to ensure there is consistency and make sure there are no magnitude errors. Once all the values are checked, the results from Abaqus can be compared with that of the DIC. The number of layers and unidirectional carbon fiber properties should also be checked. Three layers were used for the experimental setup, but only one layer was used for FEA. In addition, a unimorph configuration was used instead of a bimorph configuration. These changes need to be made to ensure results are comparable.

FEA model accuracy check

While looking at the FEA model, it was necessary to check the material properties that were obtained from previous work. It was identified that there was a mismatch from the general trend of piezoelectric properties at 1500V for MFC-1. Excel was used to plot and identify the source of this error. It is also important to note that the poisson's ratio for the piezoelectric actuator was not a uniform value.

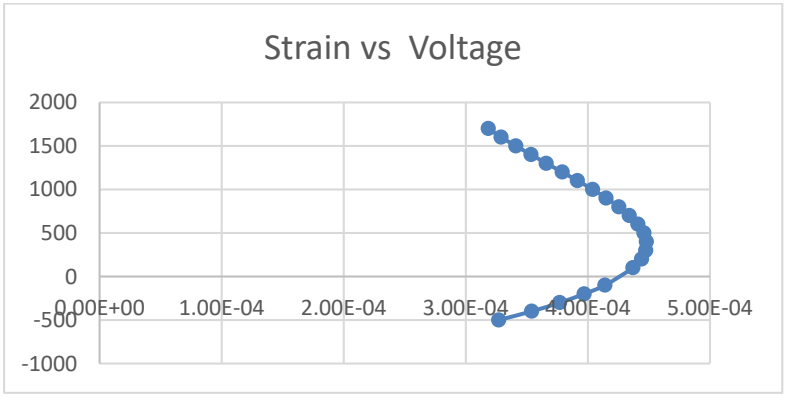

Figure 7: Strain in the y-direction for MFC

The strain values used in the Abaqus model was much different than the strain values that were in Brad LaCroix thesis. The strain values had a linear relationship in the thesis. [Fig 5-3 Transverse strain] The correct values needs to be identified to move forward with the analysis.

The unidirectional thickness was changed. The dimensions were adjusted to keep everything consistent. The material properties were fixed from previous run. The results shows 12.46 mm deflection in the z-direction.

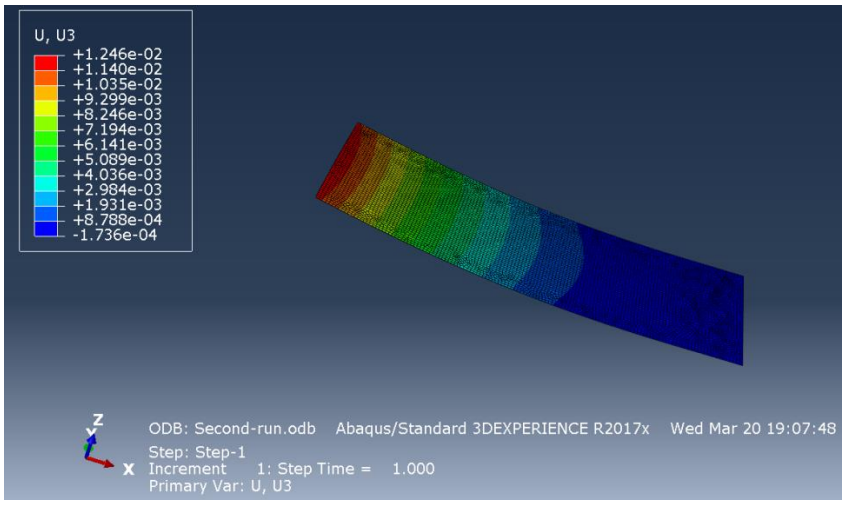

Figure 8: Deflection results for updated FEA model

The next steps involve validation this data with experimental data from DIC module observed from M8528 P1 co-cured sample.

FEA and DIC comparison

The dimensions of the model were adjusted based on sample 2 from Set 1(M8528 co-cured). Multiple time steps were created for different voltage increment in Abaqus. Displacement was recorded in U3 (z-direction). These data was then plotted against DIC values.

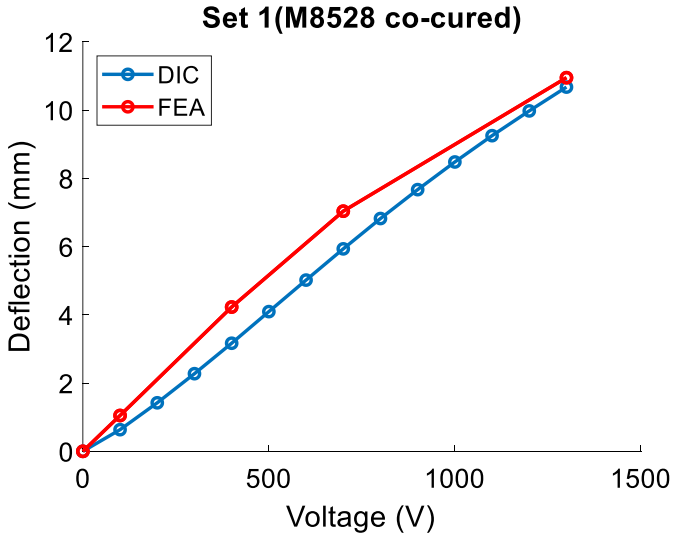

There are multiple things that need to be considered. A convergence analysis should be done for the finite element model to ensure accuracy of obtained results. All the co-cured samples were measured and plotted for the first cycle. It is important to note that this model only accounts for the first pass from 0-1400 V. When there are multiple cycles involved, hysteresis takes effect and the deflection values do not match with the deflection values obtained from FEA. Another reason for the mismatch could be due to the node that was selected for probing. The DIC measured values were close to the edge of the active region of the MFC.

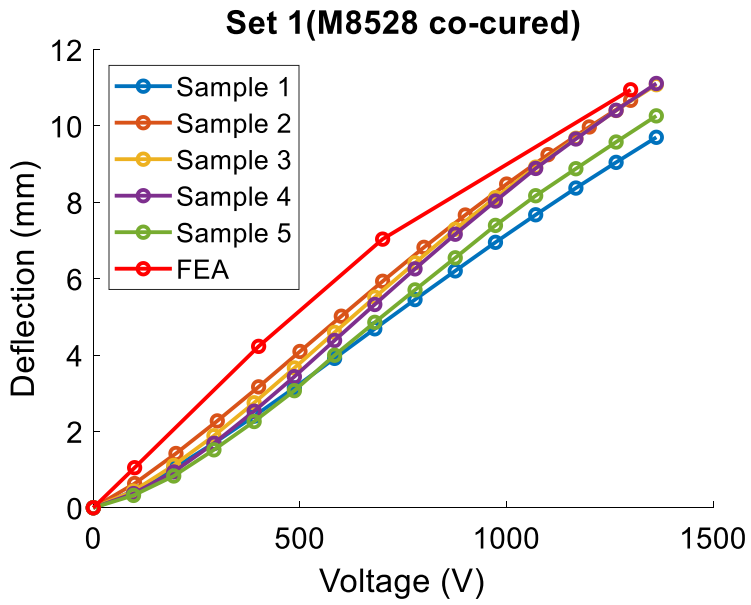

Optimization of the piezoelectric placement for the multi-curved surface in Abaqus

A simple sweep by changing the angle of the MFCs in relation to the wing is presented below. The optimum value seems to occur at about 34 degrees. It is important to note that these values were magnitudes obtained from Abaqus. Some of the results had deflection in opposite directions along the z-axis. This was done before accurately placing the MFC angles.

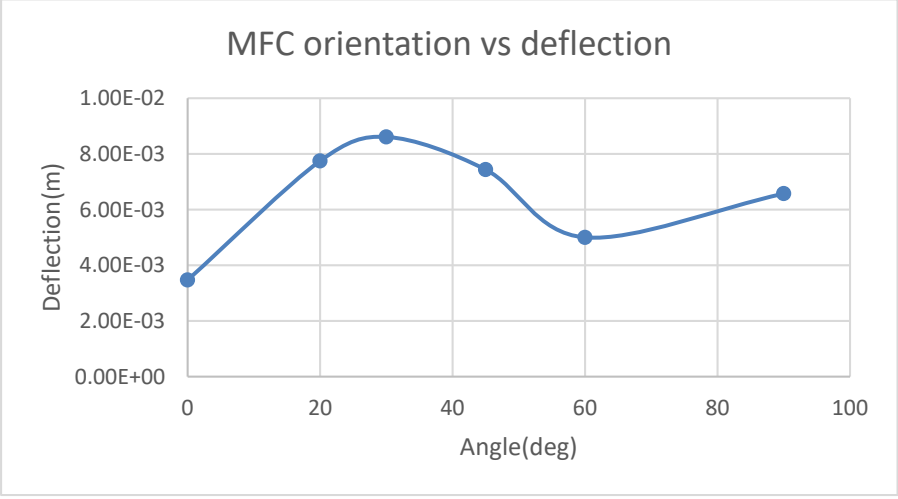

After comparing some preliminary analysis on the multi-curved wing imported from Solidworks, it was important to understand the orientation of the MFC in relation to the composite layup underneath. The following shows a good match with the behavior of MFCs when placed at different orientations.

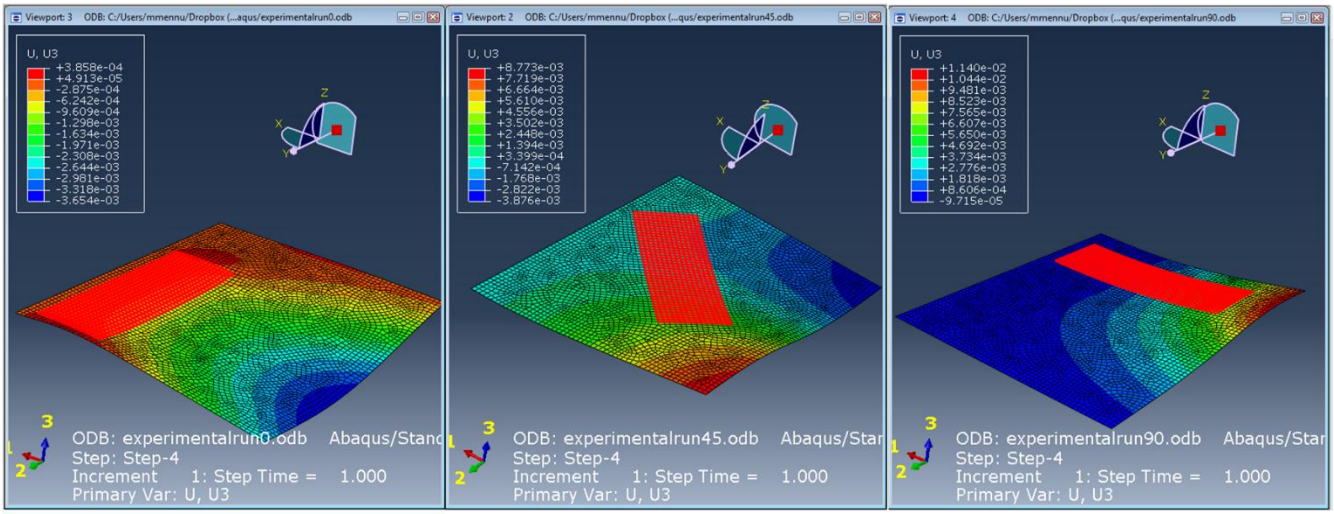

Figure: Comparing MFC orientation in a square plate

Based on the above understanding, a parameter sweep on the orientation of the MFC on the multi-curved wing will be studied.

A separate material coordinate system was used for the MFC to simplify steps in the iteration process. The orientation of the unidirectional carbon fiber was aligned to the MFC placement in the wing section. This was done by changing the angle in the section properties in the Abaqus menu. Once this step was established, various angles of the MFC was tested. Some examples are shown below.

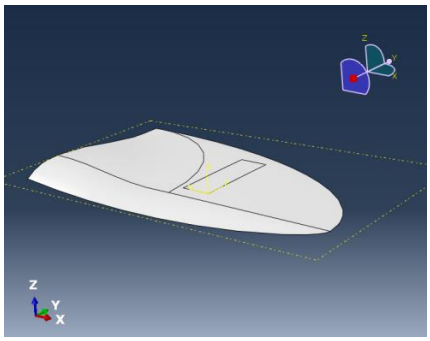

Figure: Separate Coordinate system used for MFC section in FEA model

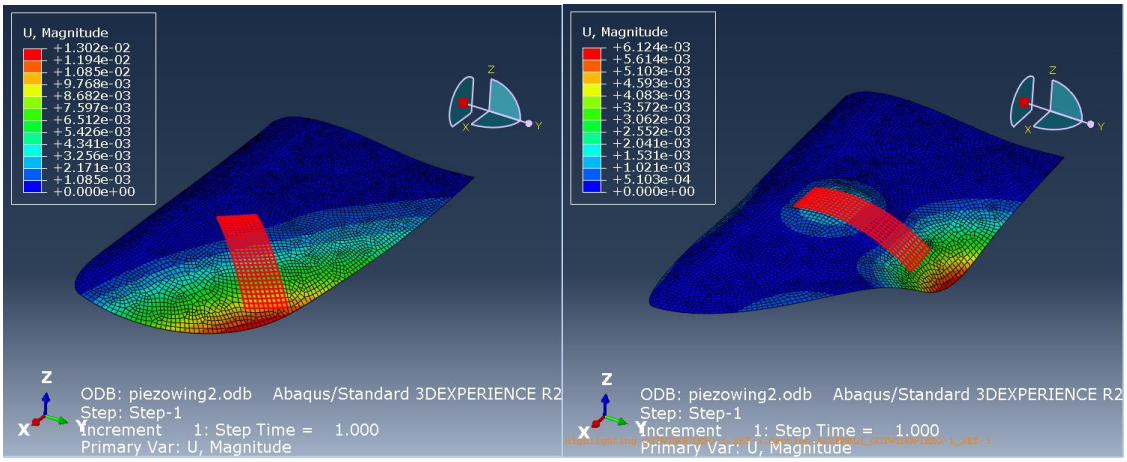

Figure: Deflection results for two different orientation of the MFC actuator

The new parameter sweep can be seen in the following curve. The analysis was done for orientation from 0 to 90° MFC orientation with 15 degree increments. The optimum placement based on this curve is at about 61°.

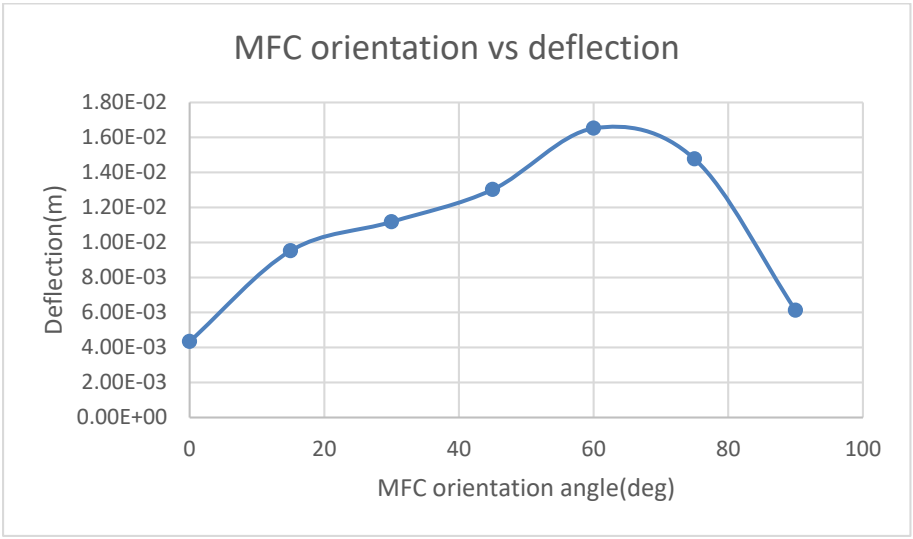

The above results were using a unidirectional laminate. For the following study, a bidirectional laminate is used by duplicating E_1 to E_2. The results are presented below. A new model has to be created to determine the optimal design for the outboard wing with bidirectional carbon-fiber and a larger MFC.

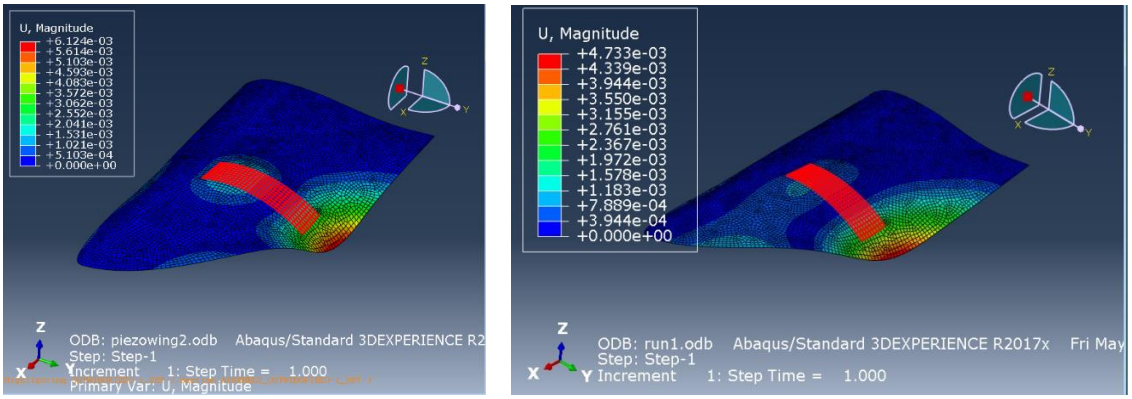

Figure: Deflection results using a unidirectional laminate (left) compared to bidirectional laminate (right)

A new model with the large MFC has been created. The section that will be assigned the MFC has also been partitioned in such a way that it can be changed to determine the best piezoelectric placement. A bimorph configuration has been assigned. In addition, the leading edge of the wing has been fully constrained, i.e. the encastre option was used. The piezoelectric strain field was applied to the model.

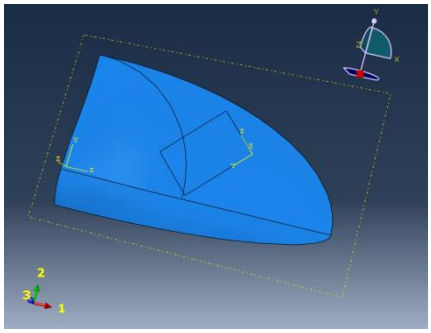

Figure: New model with larger MFC (85 mm x 57 mm)

The first simulation for the larger sized MFC was conducted with a unidirectional laminate. The results are displayed in the following figures. The first result has unidirectional fiber direction along the leading edge. This result was compared to a fiber orientation perpendicular to the leading edge. The deflection in the first is greater than the one on the right which is to be expected.

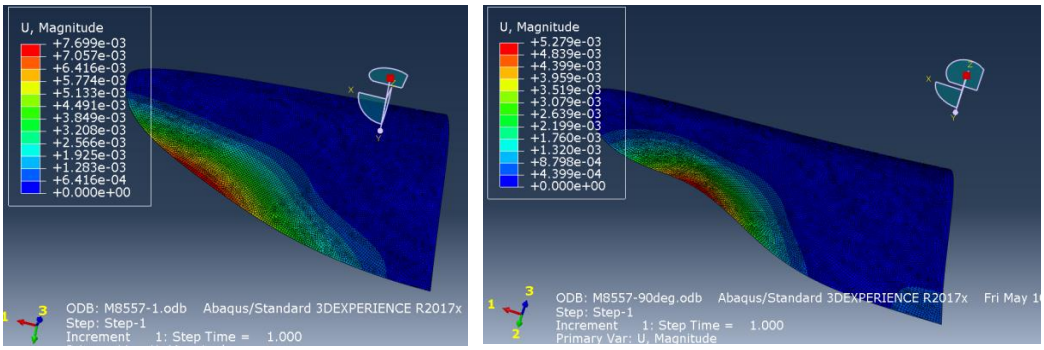

Figure: Deflection results for large MFC with fiber aligned parallel to leading edge(left) and perpendicular to the leading edge(right)

Once the unidirectional model was obtained and validated, the next step is to use a bi-directional fiber because that will be used in the actual layup process. The unidirectional material properties was changed as discussed in the beginning. The results obtained from a 0/90 bidirectional laminate is given in the figure below. It is observed that there is slightly lower magnitude of deflection compared to the unidirectional results since the stiffness in both the 1 and 2 directions are the same.

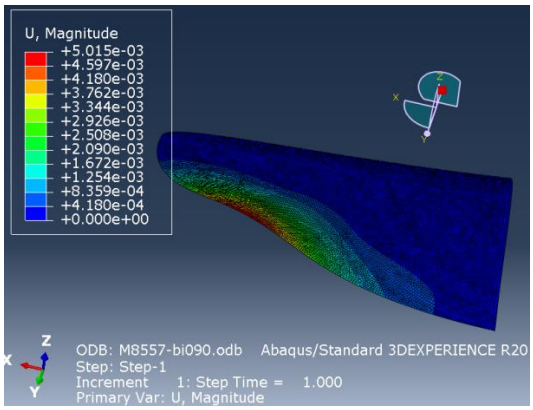

Figure: Deflection result for bidirectional laminate wing with the large MFC

The next step is to change the orientation of the bidirectional carbon fiber to match that of the MFC. This will help understanding the relationship between fiber directions with MFC actuation. The results are displayed below. There was half a millimeter increase in deflection when the fiber direction was aligned with the MFC. When attempting to optimize the MFC placement for this outboard wing, the MFC alignment and the bidirectional orientation will be matched going forward.

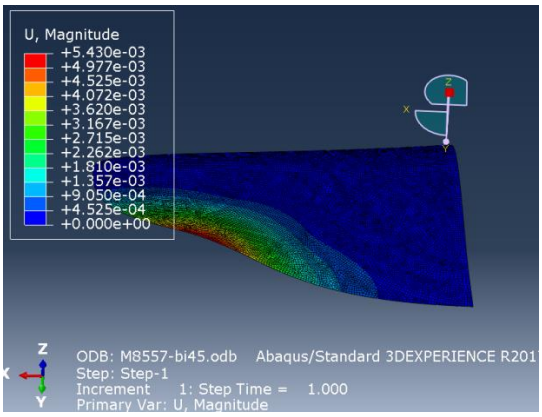

Figure: Deflection result for bidirectional laminated aligned with the MFC placement angle

The next step is to check several different orientation of the MFC and bidirectional laminate simultaneously to do a rough parameter sweep. This will help determine the MFC placement for making a prototype laminate. The boundary condition for this study was changed to the root of the leading edge to observe any deflection in the tip from a 0^o orientation MFC.

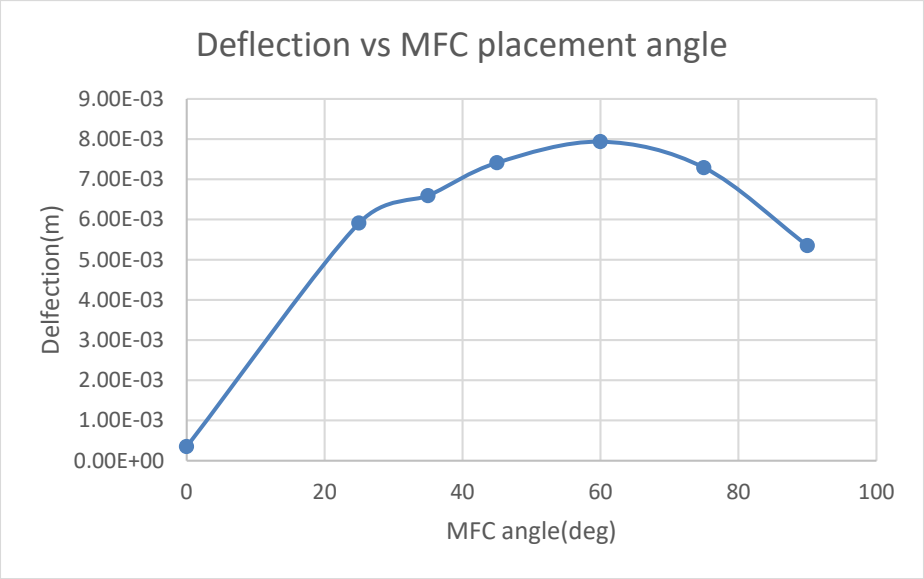

Overlapped plates experiment

Before implementing overlapping sections on the outboard portion of the wing, it was necessary to study the contact interaction between a single layered bi-directional carbon fiber plates and bi-directional carbon fiber plates with MFC attached. The schematic produced below shows the experimental setup. There were three plates that was used. The plate with the MFC layer was placed in the middle while the other two plates were placed on opposite sides. The plate on the right was placed on top of the middle layer while the plate to the right was placed underneath the middle layer. The plates shown in the figure below are clamped on the edge resembling a cantilever setup.

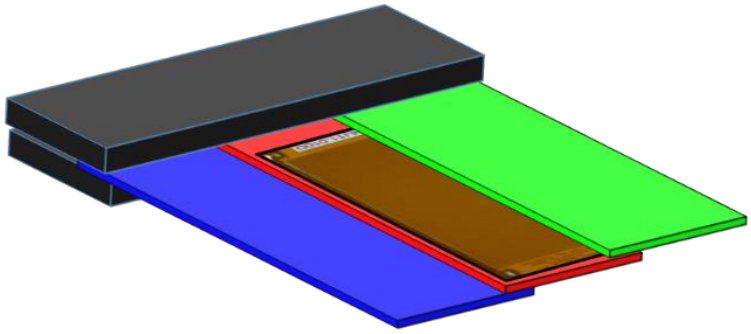

Figure. Cantilever setup for overlapped plate results

Digital image correlation was used as a non-contact measurement technique for collecting deflection data from the cantilever setup. 3D VIC software was used with two cameras mounted on a tripod facing the top of the plate. The MFC was then actuated and the deflection results were recorded. The following figure shows the plate deflection results when the MFC is actuated upwards. Deflection results for the center line of each plate was compared. The initial assumption was that the MFC plate deflection and curvature would be mimicked by the overlapped plate in the direction of the actuation. However, it was observed that the contact between the MFC plate and the overlapped plate only happened at the tip.

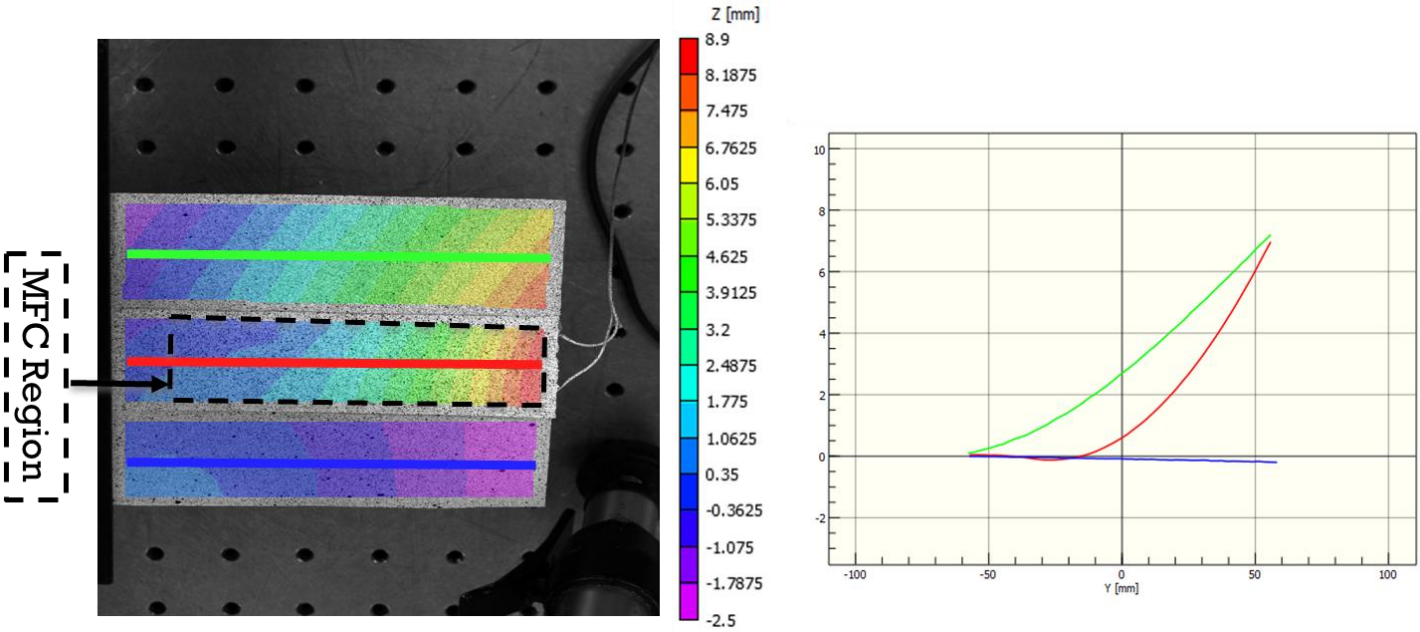

Figure. Results from the deflection study of overlapped plates

A full scale version of an outboard wing was built with the MFC angles placed based on the initial optimization scheme. The initial configuration was an unslit wing. Due to the convenience of showing the MFC placement of the wing, the camera setup of a slitted wing is shown in the following figure. The wing was clamped at the root of the leading edge which would be the location for connecting with the inboard portion of the wing.

TAIL DESIGN

Change to Vertical Stabilizer

A further change in the approach to the design concept is to change the vertical stabilizer to a V-shaped tail as shown in Figure 7.

V-Tails are designed to act as a simultaneous horizontal and vertical stabilizer; thus, the additional of a V-Tail to the morphing wing prototype will allow for longitudinal stability in concert with yaw/roll maintenance. The current material schematics for the V-Tail is shown in Fig. 8A. Silicon rubber was used to fill the center of the tail in order to increase tail deflection actuated by a pair of MFC bimorphs stationed at the slanted surfaces [Fig. 8B]. A unidirectional carbon fiber strip reinforces the silicon rubber to mitigate flight flutter. To reduce the stiffness of the two-ply substrate between the bimorphs, these plies must be oriented ±45° with respect to the MFC.

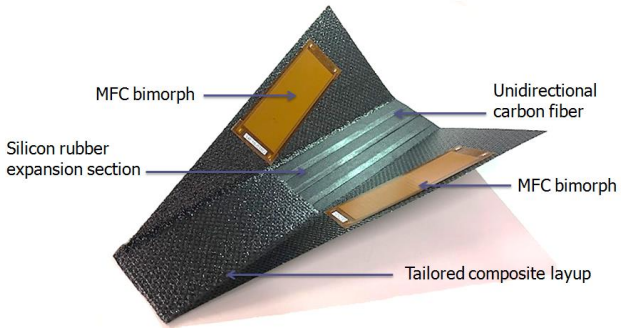

Figure 7. Changing the vertical stabilizer will make the flight vehicle more bird like in appearance, thus able to be less notice during operational deployment.

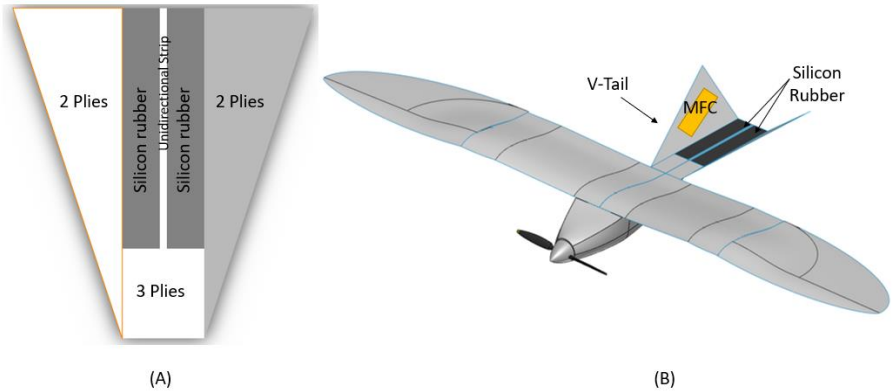

Figure 8. A) V-Tail material composition and B) an isometric view of the morphing wing V-Tail with MFC actuators

The current integration plan for the morphing wing prototype is shown in Fig. 9. In contrast prior iterations, this configuration houses two additional motors for the sweep mechanism and tendon (inboard flap) actuator. The macro fiber composite (MFC) actuator previously stationed at the inboard was substituted for a tendon actuator in order to increase trailing edge deflection. In addition, the horizontal and rudder tails were replaced with a V-tail to retain the vehicle's "bird-like" imagery; this would also prevent any damage done to the vertical stabilizer during landing.

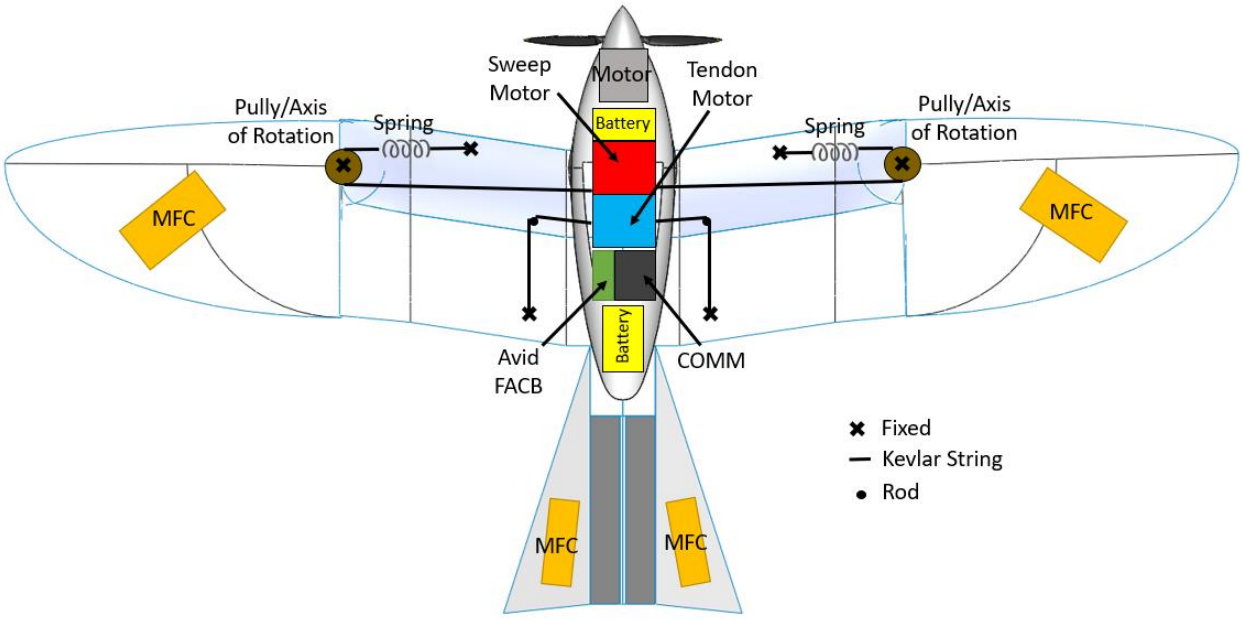

Figure 9. Current integration diagram for morphing wing

WING SWEEP MECHANISM

Tooling to Accommodate Wing Sweep

The sweep profile, a contoured surface that revolves a portion of the airfoil about the axis of rotation, was developed and imbedded onto the outer section of the morphing wing for a near perfect meshed surface sweep. The profile and wing models were created using Solidworks (CAD), and an integrated CAM app generates g-codes used to manufacture the tooling molds, shown in Figure 1. The tooling molds were manufactured via CNC using Renboard, a high-density foam material. Prepreg, plain weave carbon fiber is laid onto the molds and vacuum bagged at near 30 inHg then oven cured to produce the wings in Figure 8. Additional layers of carbon fiber were placed at the leading edges to stiffen the wing.

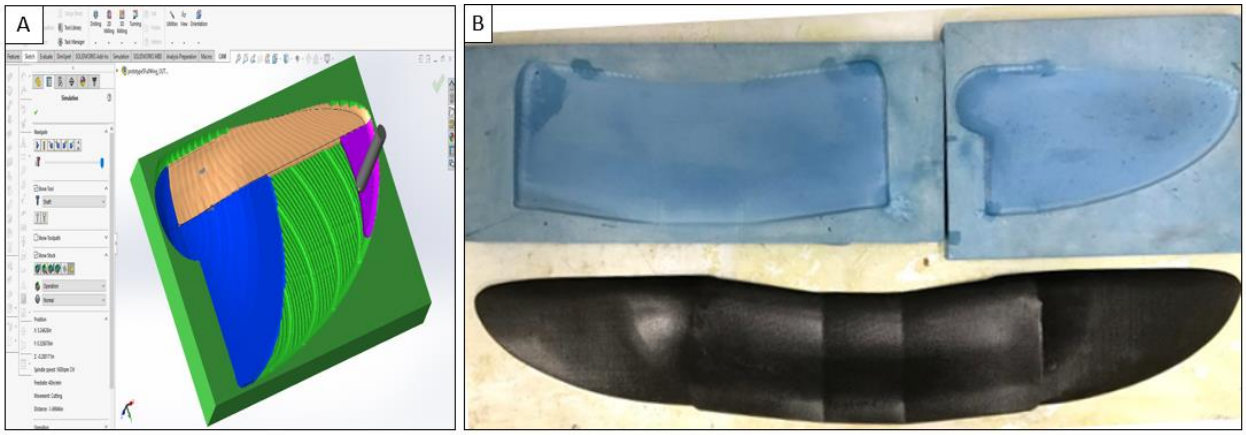

Fig. 8. (A) Generated CAD/CAM model of the tooling molds used to make (B) the Renboard molds necessary to produce the carbon fiber wings.

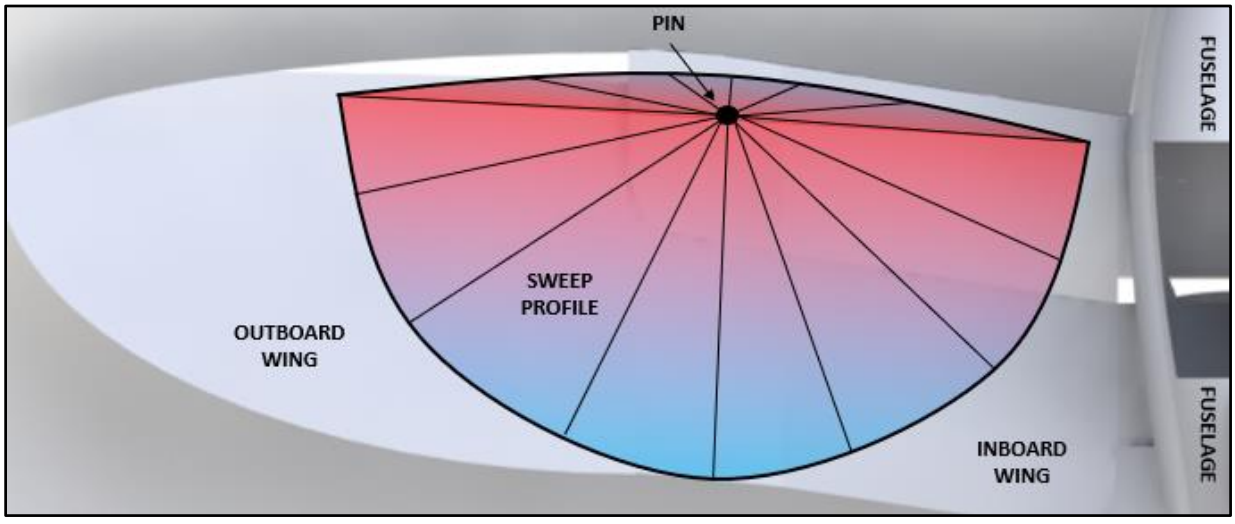

Figure 9. Illustration of a sweep profile on a morphing wing where the pin acts as the point of rotation.

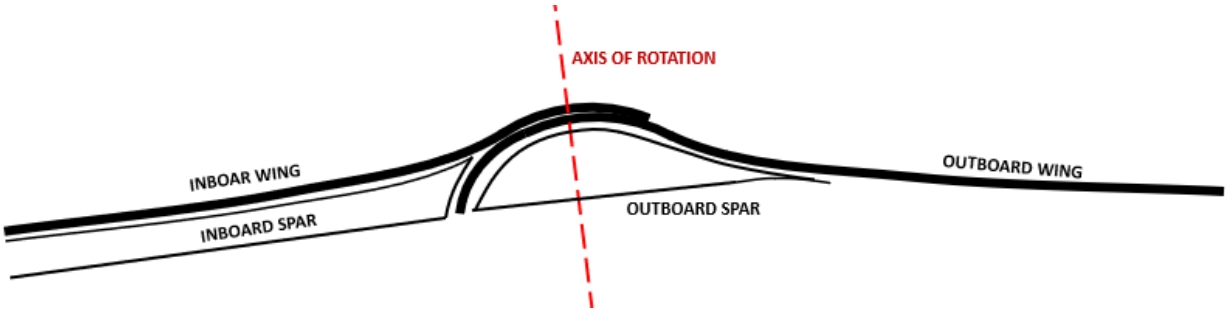

Figure 10. Front view of the wing showing the modular spar design.

A fundamental change in the direction of the wing tip sweep process is being evaluated. The basis of this change of approach is to make the inboard wing a double skinned structure, as shown in Figure 11. The leading edge of the wing top skin and the wing bottom skin are joined. The trailing edges of the wing skins, top and bottom are not joined. The change from a single skin wing to a double skin wing is being evaluated in order to accomplish the following: a) the wing tip can be swept back into the space between the wing top and bottom skins; b) a servo based approach to changing the wing camber will allow a greater degree of camber change than a piezoelectric based system; c) the necessary spar structure, internal to the inboard wing, does not have to be oval in shape; d) a flap structure can be internalized between the wing skins and deployed for take-offs and landings; and e) the mechanisms to activate the wingtips, flaps, and camber change can be internal to the inboard wing volume. Work has been initiated to develop the mechanism to actualize the wing tip sweep process.

Inboard Flap and Bottom Surface

Silicon rubber was initially positioned at the slits of the flaps to retain streamline aerodynamics; however, they also hinder the amount of tip deflection. Therefore, a solution is to replace the silicone rubber [Fig. 3A] with an overlap of carbon fiber [Fig. 3B], permitting further freedom in tip deflection while surfaces are kept streamline.

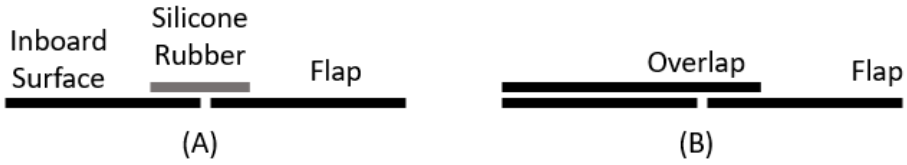

Figure 3

It may be prudent to mention how the bottom surface of the inboard will be kept streamline as it transitions toward the outboard. A current solution has yet to be found as difficulty arises during the outboard wing's sweep motion. However, there is potential in implementing another sweep profile surface at the end of the bottom surface to mesh with the outboard wing, shown in Fig. 4.

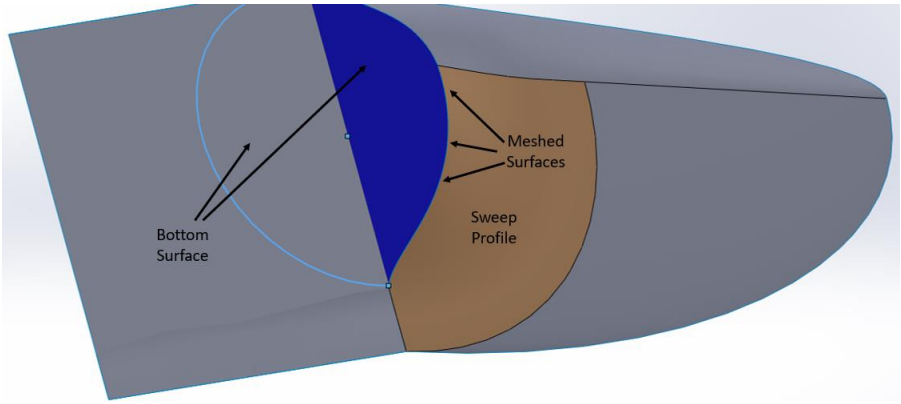

Figure 4. Bottom inboard surface meshed with outboard

1. Sweep Mechanism and Tendon Actuator

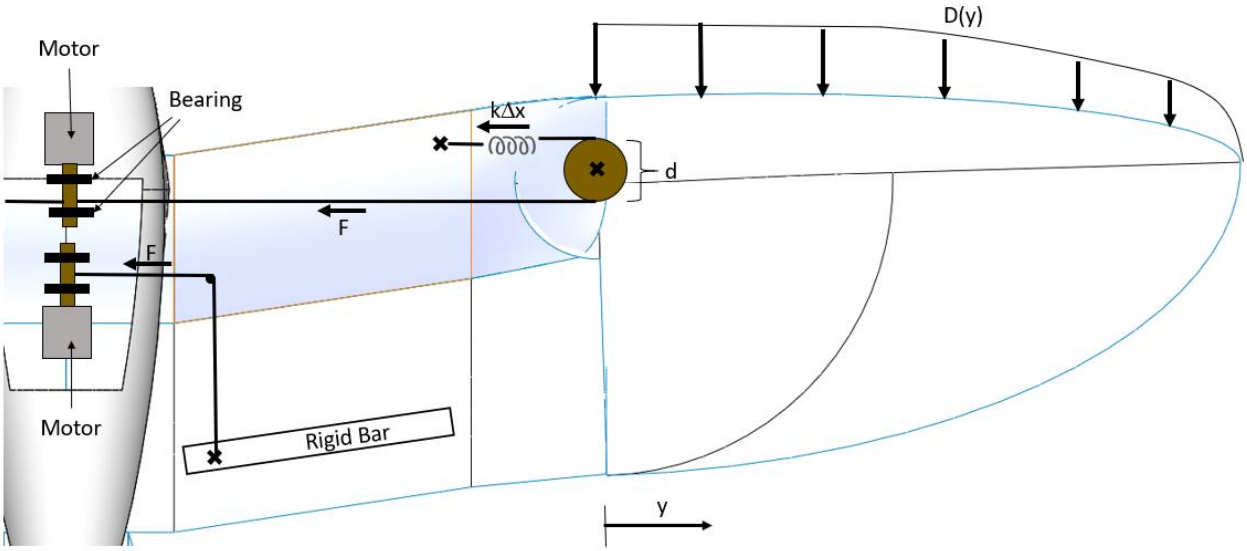

Figure 5. Sweep mechanism and tendon actuator diagram

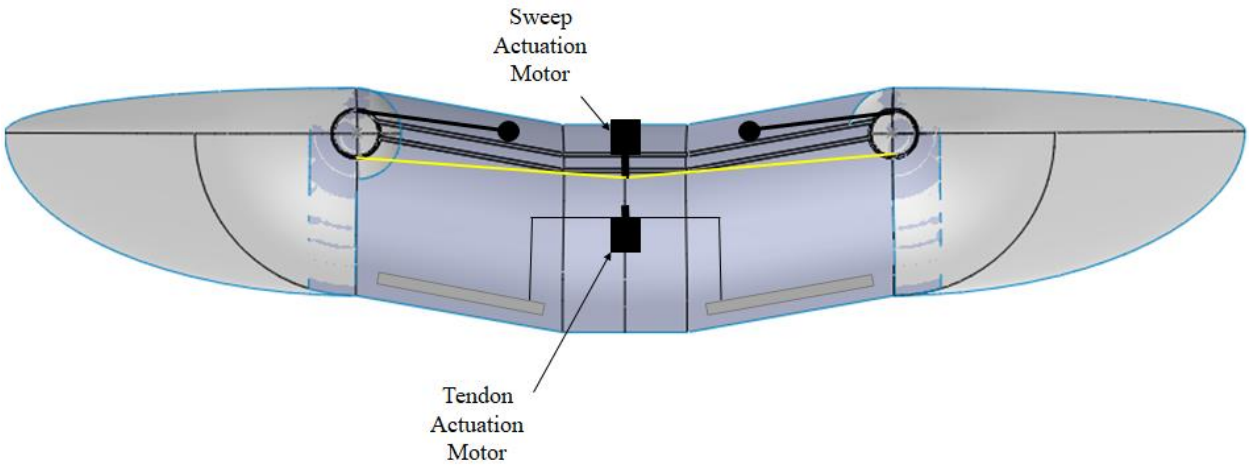

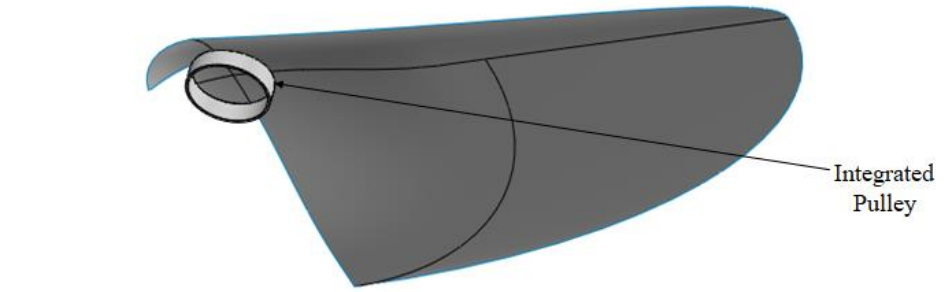

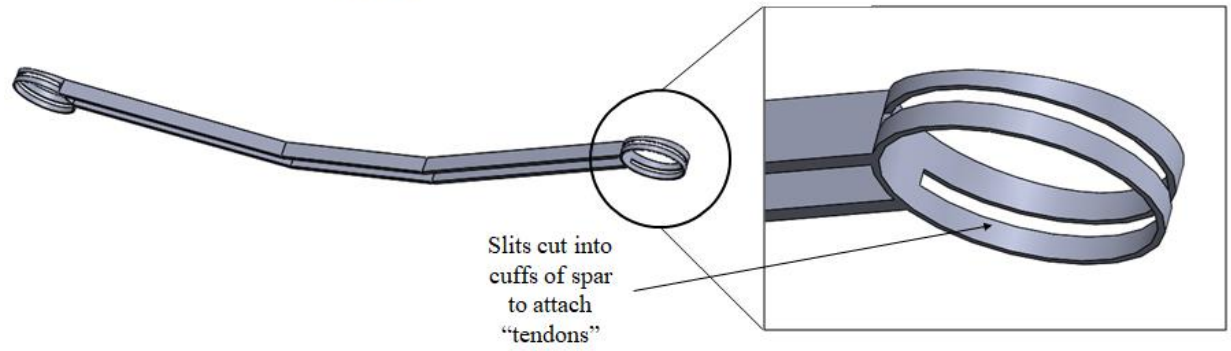

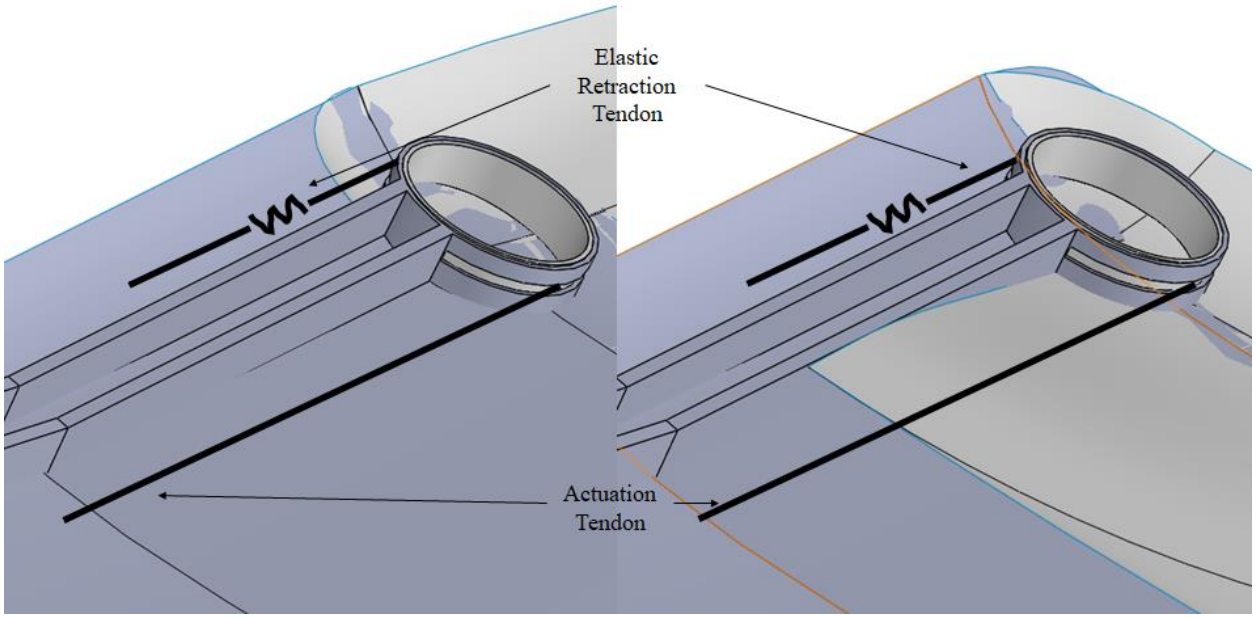

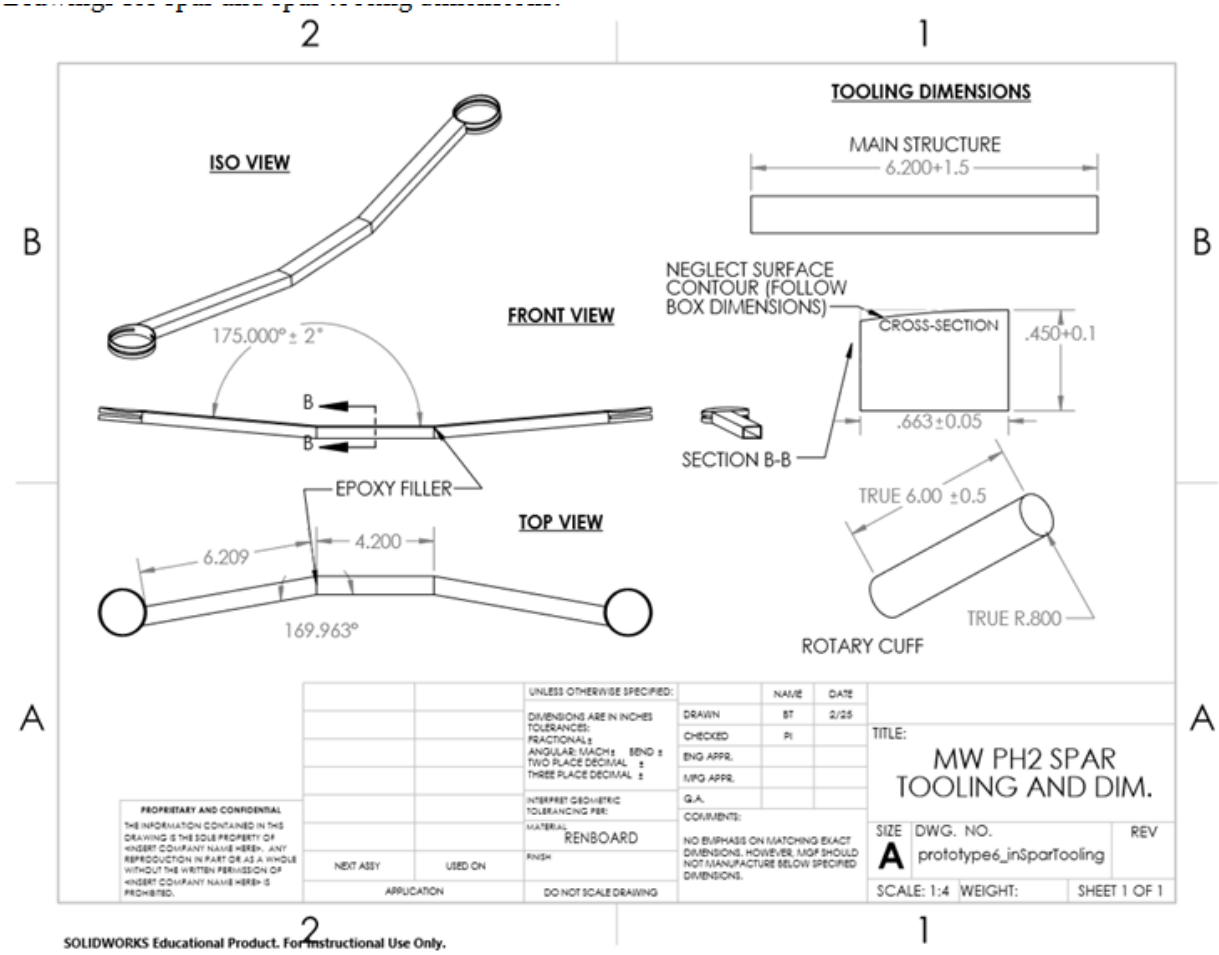
TOOLING DIMENSIONS
ISO VIEW
MAIN STRUCTURE
6.200+1.5
NEGLECT SURFACE CONTOUR (FOLLOW BOX DIMENSIONS)
FRONT VIEW
175.000° ± 2°
CROSS-SECTION
.450+0.1
.663±0.05
SECTION B-B
EPOXY FILLER
TOP VIEW
6.209
4.200
169.963°
TRUE 6.00 ±0.5
TRUE R.800
ROTARY CUFF
TITLE:
MW PH2 SPAR TOOLING AND DIM.
SIZE A
DWG. NO. prototype6_inSparTooling
REV
SCALE: 1:4
WEIGHT:
SHEET 1 OF 1
RENBOARD
SOLIDWORKS Educational Product. For Instructional Use Only.

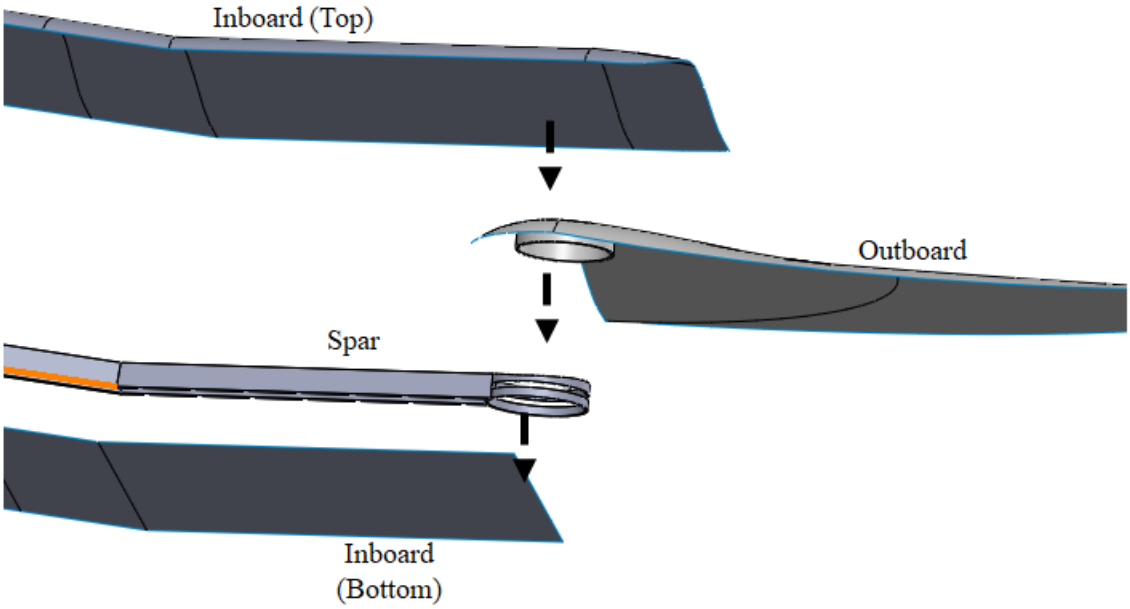
Inboard (Top)
Outboard
Spar
Inboard
(Bottom)

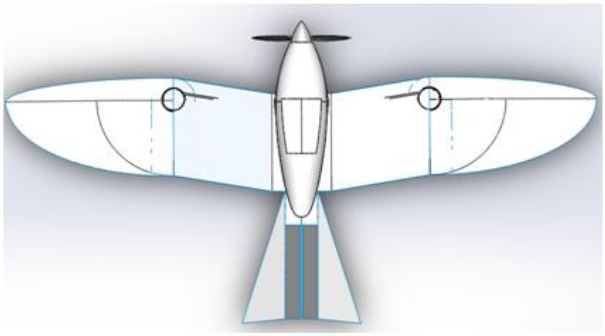

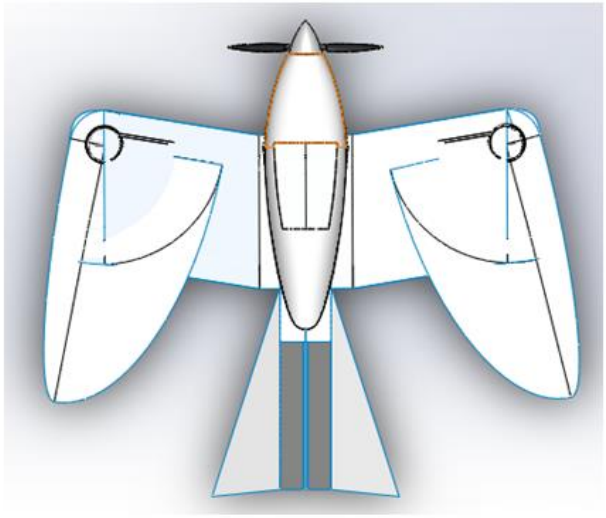

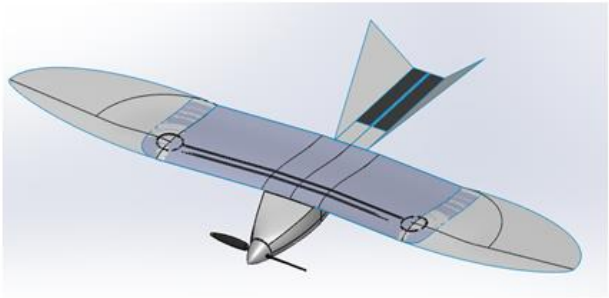

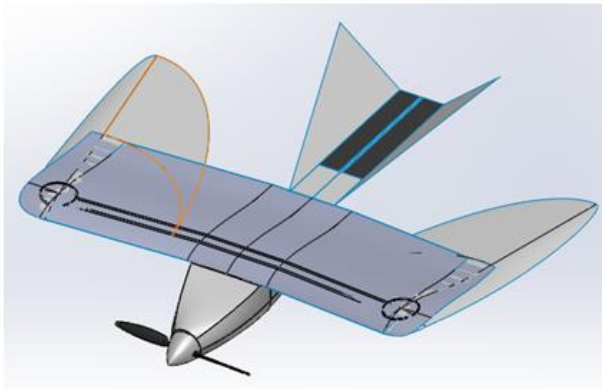

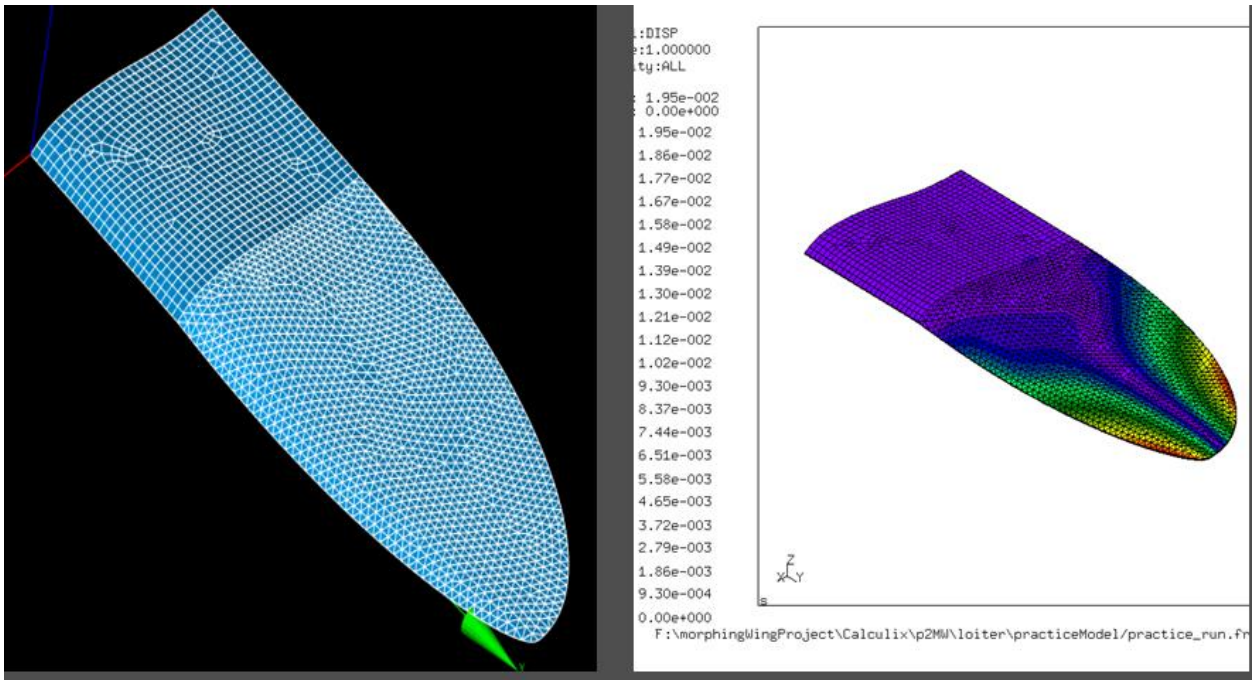

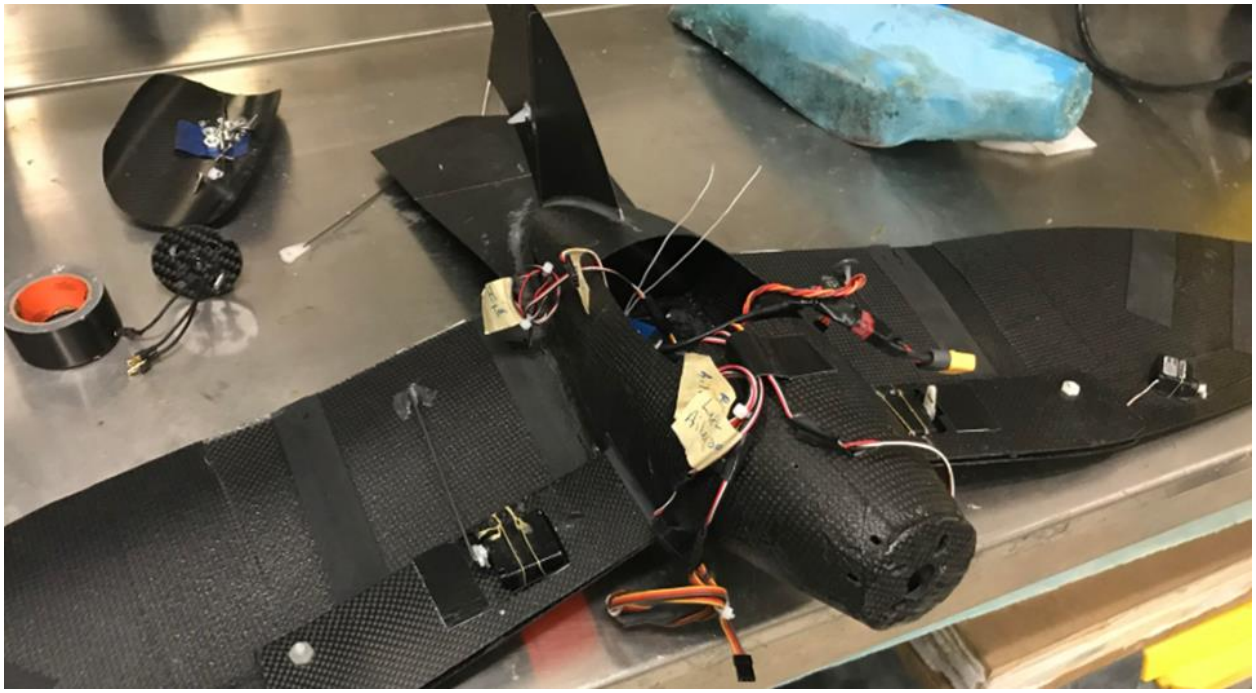

The sweep mechanism and tendon actuator mechanisms are illustrated in Fig. 5. Both mechanisms are to be actuated by servos positioned in the fuselage and attached via Kevlar strings. The strings will be wined around a nylon rod attached to the motors and supported by fixed bearings.

Sweep Actuation

The sweep mechanism in Fig. 5 is actuated by a single motor that simultaneously pulls both sides of the wing. A pully system is integrated into the sweep mechanism where one end is fixed to a spring; a spring was necessary in order to have the wing recoil back into loiter position. The parameters of the spring and motor must be designed in concert with respect to the rest of the system. The spring constant can be quantified using Eq. 1.

$$k\Delta x \cdot \frac{d}{2} = k\frac{\pi d}{4} \cdot \frac{d}{2} = T_{friction} + \sum D(y) \cdot y \qquad \text{Eq. 1}$$

Eq. 1 quantifies the restoring force of the spring acting as a moment about the axis or rotation; the moment arm can be set as the radius of the pully. The maximum spring constant required was assumed to be the restoring moment needed to restore the wing to loiter mode from a 90° sweep. The spring is assumed to extend a quarter of the circumference of the pulley for a 90° sweep. Counteracting moments considered include both the friction created between the inboard and outboard wings and the aerodynamic drag as a function of wing span. After designing the spring constant, servo parameters can be designated. It's worth noting that the time to perform a full sweep motion should be limited. Thus, servos must have RPM speeds in tandem with the required torque to meet this time limit.

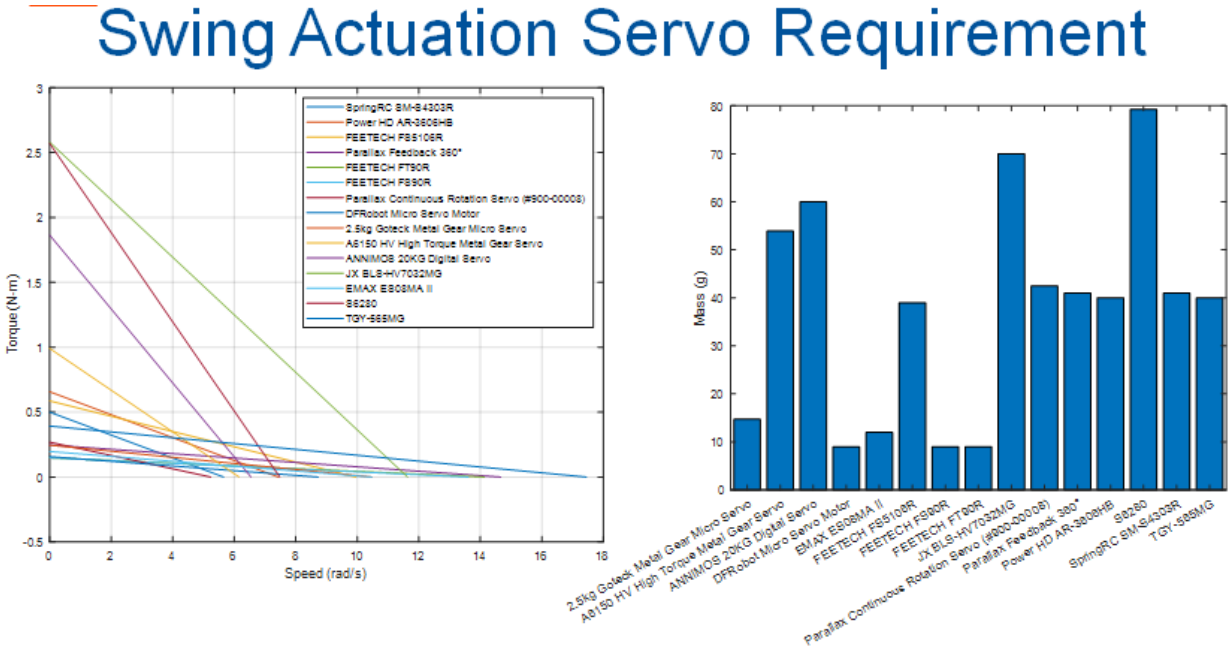

Swing Actuation Servo Requirement

Assuming 20 cm servo rod diameter

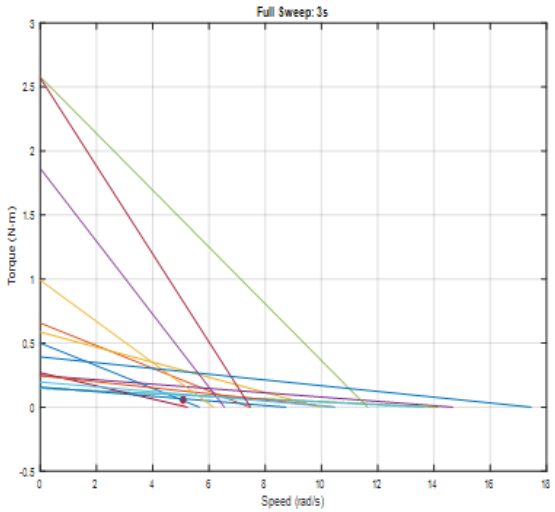

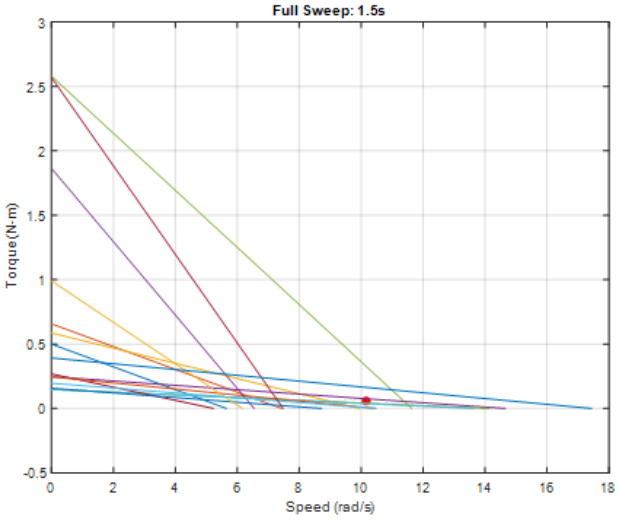

MATERIAL STUDIES and CHARACTERIZATION

Experimental Setup for Characterizing the Material Properties of Carbon Fiber Prepreg
The carbon fiber used in this project is prepreg. This is a carbon fiber system that has already been pre-impregnated with epoxy material. The curing process is done in the lab after laying up the prepreg in the desired geometry. It is important to determine the material properties of the carbon fiber to accurately model the wings as well as other aspects of the vehicle. Tensile and shear test specimens were made from the carbon-fiber prepreg. 10 layers of prepreg was used to make a 16-inch square plate of bidirectional carbon-fiber. Once the plate was made, the tensile test pieces and shear pieces were cut out with waterjet to the required ASTM standards. In addition, tabs were attached to the tensile test specimens.

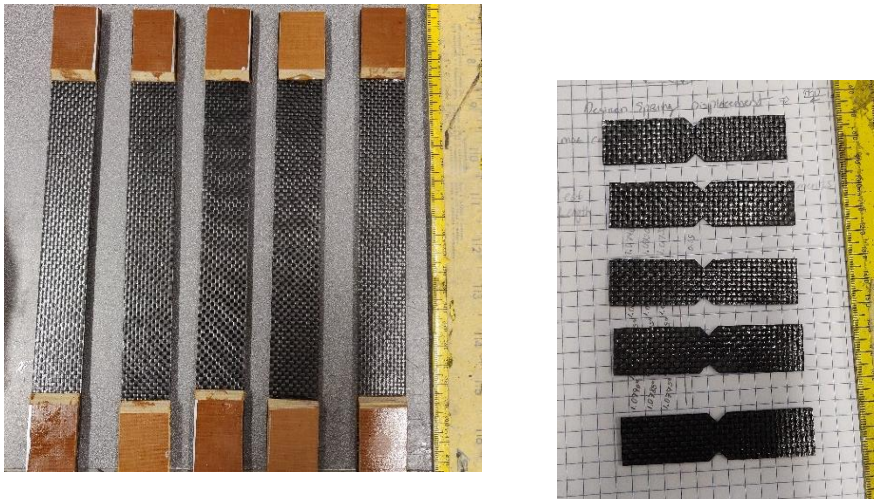

Figure 14. Tensile test specimens and shear specimens of bidirectional carbon-fiber

Test Resource Universal Testing Machine (UTM) was used for loading the specimens. Digital Image Correlation is a full-field measurement technique using stereo cameras to capture deformation and strain data accurately. It requires the use of stereo cameras and it is simple to setup. The specimen preparation requires speckle patterning to allow for uniquely characterizing sections of the specimen. This is achieved in the lab by using spray paint. First, a layer of white spray paint is used. Then, the black spray paint is sprayed at an optimal distance to get the required distribution and size of the speckle patterns. For this measurements, two cameras on the front and back side of the specimen are mounted. This allows for getting an average strain of the specimen. Light sources are also mounted on both sides in order to get even lighting across the specimen.

a)  **b)**

Figure 15. a) DIC camera setup with light sources b) speckle pattern

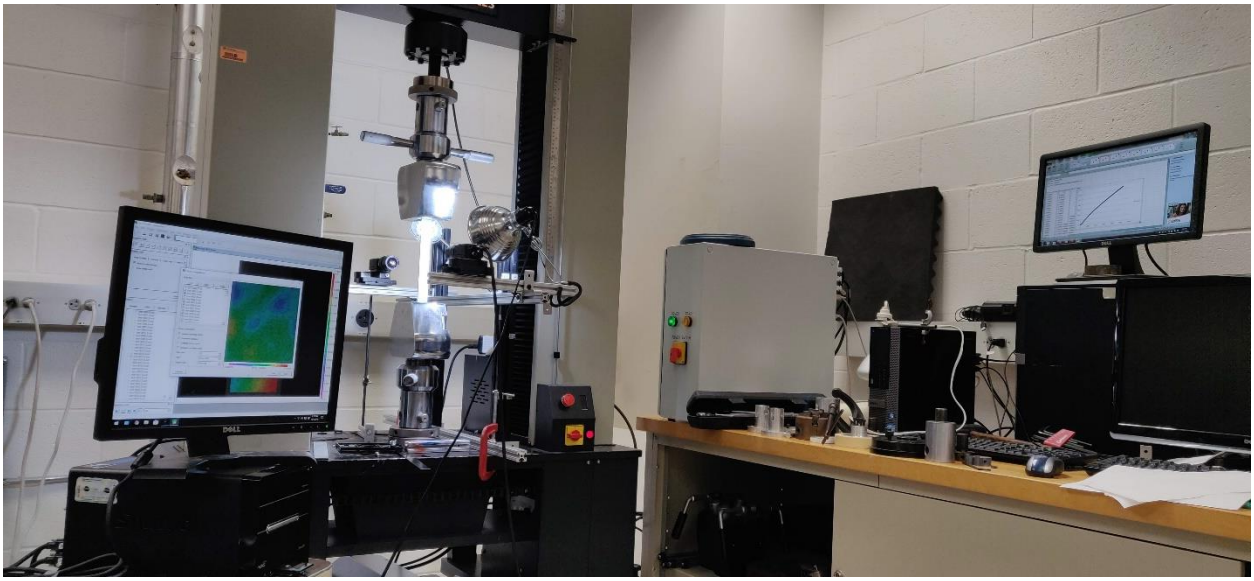

Figure 16. Full setup with Universal Test Machine and Digital Image Correlation with two cameras

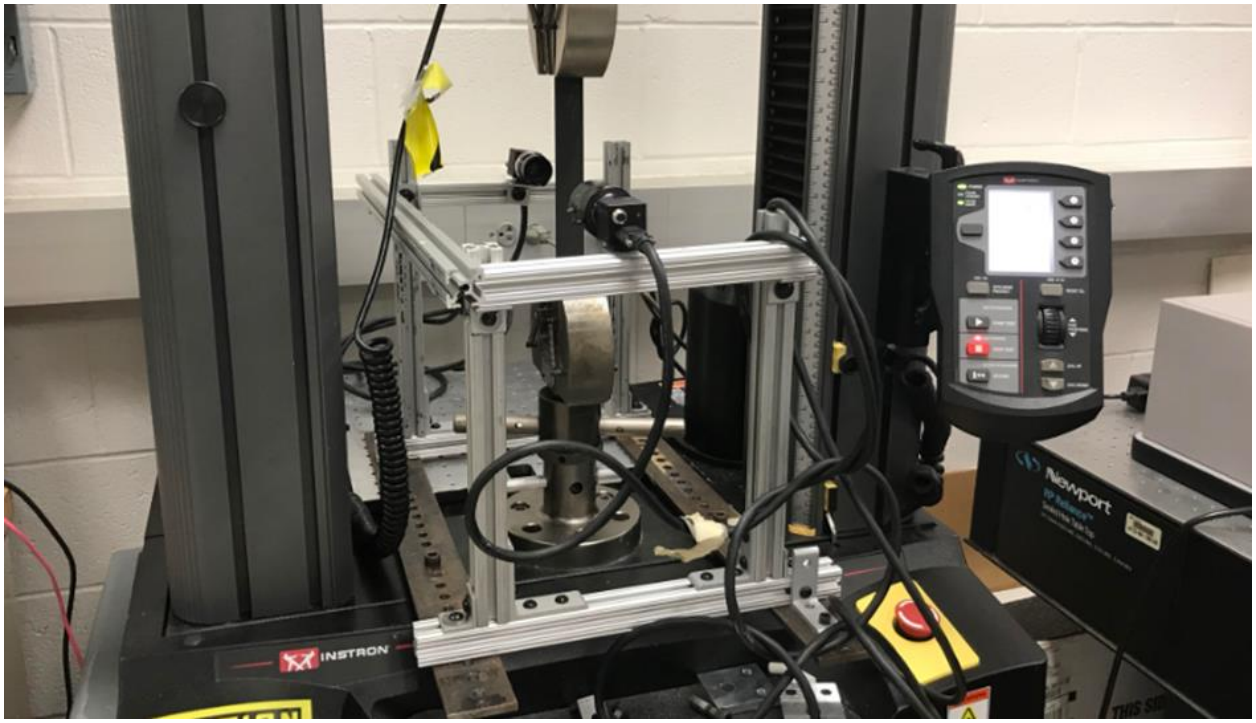

Tensile Test (AS4 Plain Weave Carbon Fiber Prepreg)

In order to obtain material properties for structural models later, uniaxial tensile tests were performed on HexTow AS4 plain weave carbon fiber prepregs specimens. AS4 was originally selected as the primary material for the morphing wing due to its marketed high longitudinal modulus and small thickness, which are ideal combinations to maximize piezoelectric bimorph deflection [2]. Test coupons were produced specific to guidelines set by ASTM D3039 [3]. Coupons each consisted of 10 ply layers. Garolite (G10/FR4) tabs were used to mount the test coupons to the grips of the universal tensile testing machine (UTM) without wearing the specimen. Araladite brand structural epoxy was used to fix the tabs onto the coupons via clamping for approximately five hours.

Figure 4 shows the test setup. Two sets of 10 specimens were produced at 0° and 45° fiber orientation. Fiber orientations were chosen to measure longitudinal, transversal, and in-plane shear modulus effectively. Two high-resolution cameras are positioned on either side of the test coupon on the UTM for analytical digital image correlation (DIC) post-process analysis. Note that two-dimensional DIC requires that both cameras are level with ground and are directly normal from the other. Use of two-dimensional DIC with two cameras allow for out-of-plane displacements to average to approximately zero. However, tester should be wary of too much out-of-plane deflection, which will skew results.

Figure 4. Digital image correlation and uniaxial tension test performed on AS4 carbon fiber specimen.

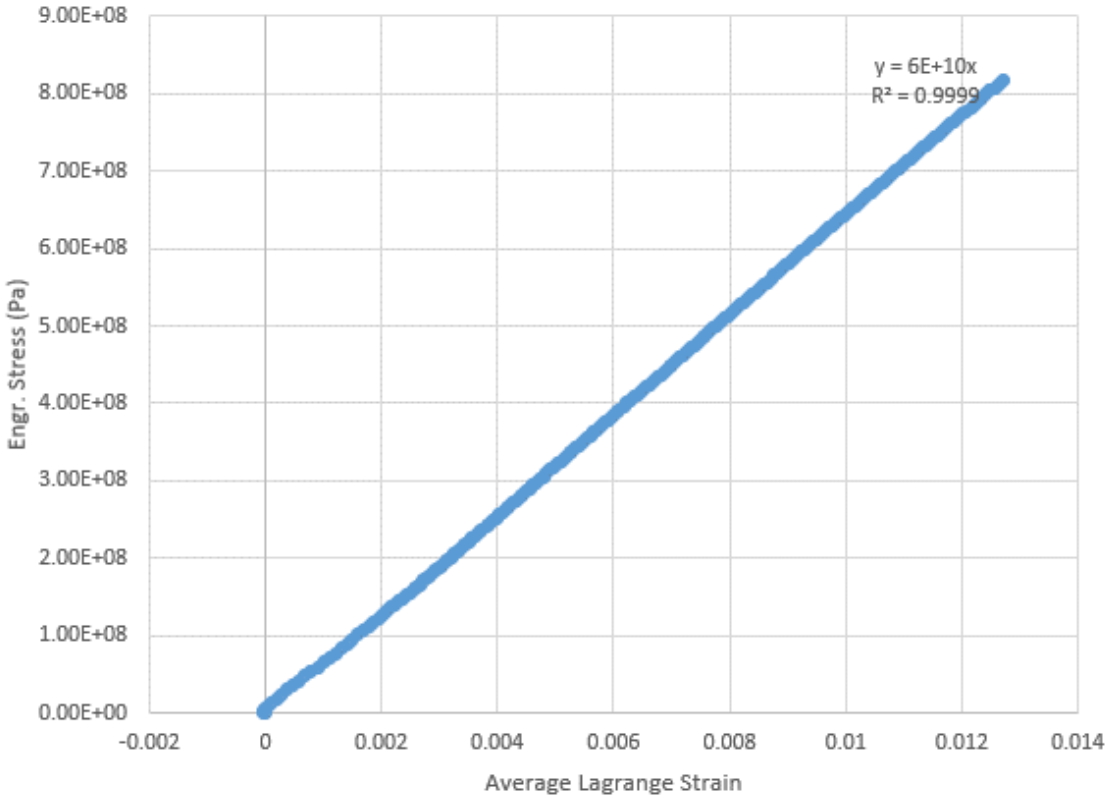

Figure 5. Experimented stress strain curve for AS4 0° specimen. Engineering stresses obtained by averaging resultant loads with specimen cross-sectional area. Strain was measured via digital image correlation and reported in Lagrange coordinates.

Sample test results for a 0° AS4 specimen is shown in Figure 5. Five specimens from each fiber orientation set has been tested and material properties have been recorded. The approximate material properties for the current tested specimens are given in Table II. Note that experimental case studies for

out-of-plane properties are to be ignored since they will have negligible effects on material behavior through application.

TABLE II
Experimented Material Properties for AS4 Carbon Fiber Prepreg

Longitudinal Modulus, E_1	64.3 GPa
Transverse Modulus, E_2	64.3 GPa
In-plane Poisson Ratio, ν_{12}	0.00363
In-plane Shear Modulus, G_{12}	390.0 MPa
Tensile Strength, S_T^+	816.1 MPa

Finalized Tensile Test (AS4 Plain Weave Carbon Fiber Prepreg)
The biomimetic morphing wing prototypes are primarily made with AS4 plain weave carbon fiber-epoxy composite prepregs. This material was implemented based on its marketed high longitudinal modulus and minimal ply thickness, ideal as a substrate for increased macro fiber composite actuation curvature for control surfaces (see *Investigating potential substrates to maximize out-of-plane deflection of piezoelectric macro-fiber composite actuators*, LaCroix et al.).

In order to characterize the composite properties of AS4, tensile-digital image correlation (DIC) testing was performed on ten 0° and ten 45° test coupons, as shown in Figure 5. Each coupon is fabricated specific to dimensional sizes detailed for ASTM D3039 standards (250 x 25 x 2 mm^3). Garolite tabs were fabricated (40 x 25 x 3.175 mm^3) and adhered to the test coupons via structural epoxy; this prevents the vice grips from puncturing the test coupons, causing premature failure through a concentrated stress at the ends of the coupons.

Strain is measured using DIC. In order to measure two-dimensional strains, cameras were placed equidistant on either side of the coupon. This will negate out-of-plane displacement values once collected data from both cameras are averaged. The resultant material properties for AS4 prepreg is displayed in Table III.

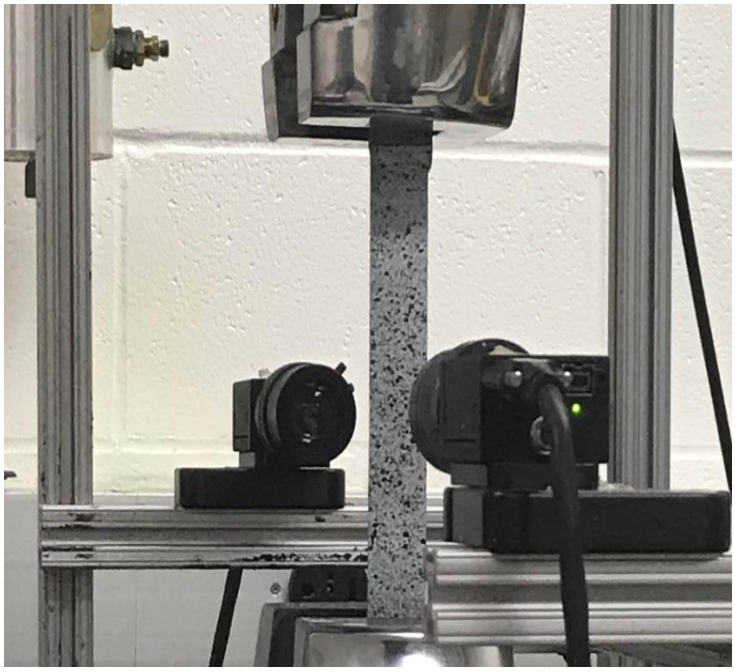

Fig 5. Tensile test on AS4 carbon fiber test coupon. Speckle pattern is applied to both sides of coupon. DIC cameras are placed on both ends of the coupon.

TABLE III
Experimented Material Properties for AS4 Carbon Fiber Prepreg

	Average	Standard Deviation
Longitudinal Modulus	65.90 GPa	2.21 GPa
Transverse Modulus	65.90 GPa	2.21 GPa
Major Poisson Ratio	0.0500	0.0235
Long. Shear Modulus	1.68 GPa	0.587 GPa
Out-of-Plane Shear Modulus	600-800 MPa	-
Tensile Strength	841.99 MPa	41.37 MPa

Note that the denoted average value for out-of-plane shear modulus (G23, G13) are given at a variable range. It is assumed that the behavior of the fiber reinforced prepregs is focally planar. All out-of-plane stresses are then considered negligible. However, smaller values other than the recommended quantities are ill advised if the given material is analytically evaluated; smaller out-of-plane modulus may result in potential yielding/buckling through the thickness of the composite, reducing the accuracy of analysis.

The material properties were validated by using DIC testing to compare a tip loaded cantilever beam experiment to a finite element method (FEM) using ABAQUS. Figure 6 displays graphical results of both methods.

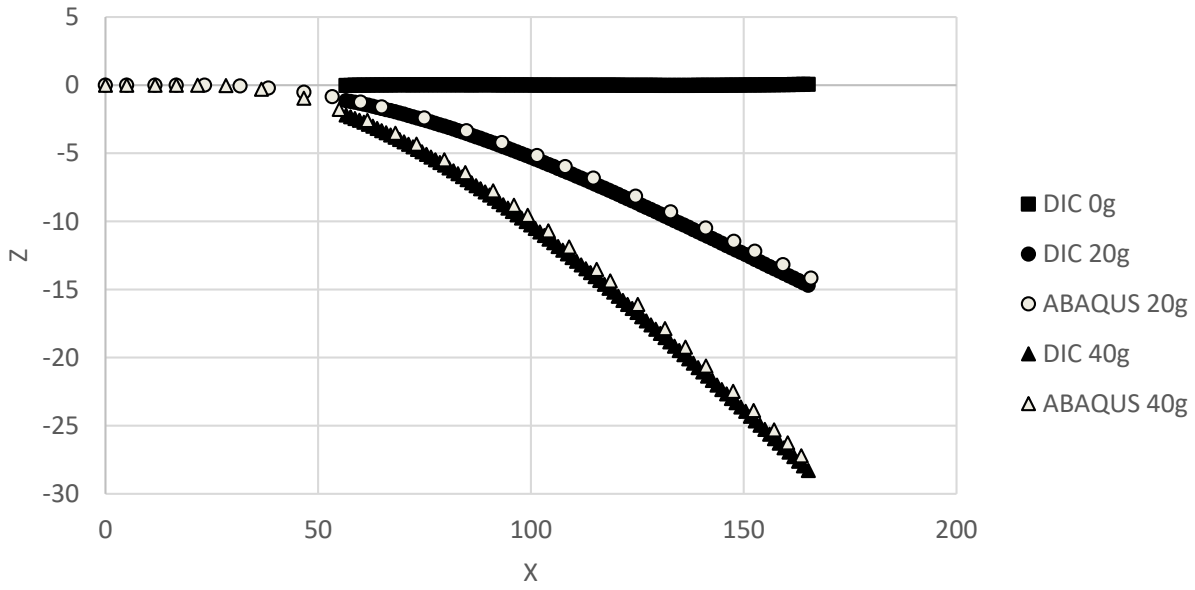

Fig 6. Cantilever beam comparison between experimental digital image correlation results to ABAQUS finite element analysis.

The in-plane shear modulus, G_{12}, is calculated using the following set of equations derived from the constitutive relation for orthotropic materials, assuming plane stress.

$$\tau_{12} = -\sigma_x cos\theta sin\theta$$

$$\gamma_{12} = -2cos\theta sin\theta\varepsilon_x + 2cos\theta sin\theta\varepsilon_y + \gamma_{xy}(cos^2\theta - sin^2\theta)$$

$$G_{12} = {}^{\tau_{12}}/_{\gamma_{12}}$$

where γ_{12} and τ_{12} are the in-plane shear strain and stress, σ_x is the global longitudinal stress, and θ is the fiber direction. ε_x, ε_y, and γ_{xy} are the global longitudinal strain, transverse strain, and in-plane shear strain.

MFC BIMORPH HYSTERESIS STUDIES

Hysteresis Compensation Program Error

The mathematical errors of the hysteresis tracking program consequently caused incorrect positioning of tip displacement. Fortunately, this problem can be dealt with by interpolating ascending curves in order to map the tracking position to the ideal path (i.e. choose the curve that includes the starting position of the next actuation step).

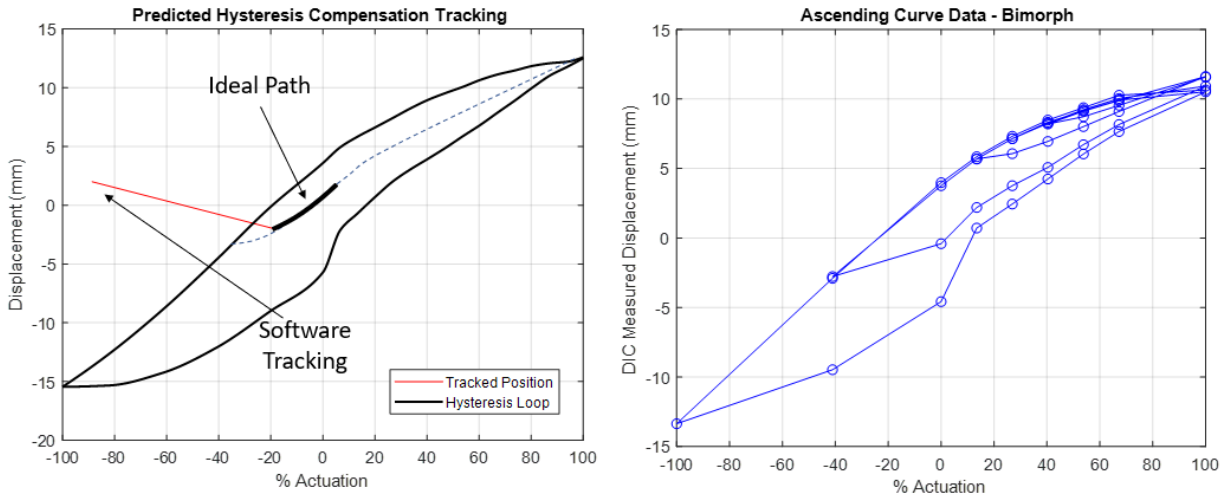

Figure 8